==================== **PHYSICS** ====================

Cherenkov Relativistic Generators
Based on Symmetric *E*-Waves of a Corrugated Waveguide

V. F. Kravchenko[a], A. A. Kuraev[b],
Corresponding Member of the RAS V. I. Pustovoĭt[c], and A. K. Sinitsyn[b]

INTRODUCTION

Electrodynamic systems of modern power and super-power microwave electronic devices [gyrotrons, relativistic running-wave lamps (RWLs), and relativistic inverse-wave lamps (IWLs)], including energy inputs/outputs, represent segments of irregular waveguides. The operating conditions for these waveguides are preferably multiwave. The improvement of physical characteristics of superpower microwave devices is associated with the optimization of the profile of their electrodynamic systems. This requires the development of a novel theory and methods for calculating arbitrarily irregular waveguides. However, there exists a method that would appear to be the most efficient for both the calculation of irregular waveguides and the physical interpretation of phenomena occurring in them. This method is based on the mapping of an arbitrarily irregular inner waveguide surface onto a regular cylinder, a coaxial structure, etc., with a circular or rectangular cross section [1–5]. In the transformed (oblique) system of coordinates, the solution represented in the form of connected normal waves is based on using the projection procedure. In this case, the amplitudes of the connected waves are described by a set of ordinary differential equations with variable coefficients, their form being determined by the irregular-waveguide profile. The boundary conditions to this set correspond to the initial and final cross section of the irregular-waveguide segment (two-point problem).

Solving this problem by conventional methods meets with no difficulties provided that only propagating waves are considered. As is shown below, for the exact calculation of the waveguide, supercritical waves that substantially change the physical characteristics of the waveguide should be taken into account along with the propagating waves. However, for supercritical waves, an exact solution to the boundary value (two-point) problem, which is based on the use of traditional methods (stepwise methods of the Runge–Kutta type or the Hemming method), is impossible by virtue of their rapid divergence. (We imply that abruptly increasing solutions appear due to small errors.)

To solve this problem, we used in this study the stable method of the block matrix sweep [6, 7]. We compare the results obtained on the basis of the newly developed method with those for the calculation of the same waveguide irregularities by the finite-element method. We give attention to the absence of the second-rank periodicity condition (Floquet condition) in matched segments of periodic irregular waveguides. This shows the inaccuracy of a number of studies in the field of the RWL and IWL theory [11–14], which are based on the indicated condition and on the conception of field spatial harmonics.

SELF-CONSISTENT EQUATIONS OF THE NONLINEAR MODEL FOR RELATIVISTIC IWLS AND RWLS SUPPLIED WITH A RETARDING SYSTEM IN THE FORM OF A CORRUGATED WAVEGUIDE

A theory of relativistic RWLs and IWLs supplied with the electrodynamic system in the form of an irregular corrugated waveguide was developed in [1–3, 7, 15] on the basis of the method of coordinate transformations. For RWLs and IWLs operating with the E_{0m} wave of the irregular waveguide, this theory, in the two-dimensional approximation, leads to the following set of self-consistent nonlinear equations:

$$\frac{d\dot{A}_m}{dz} = (sW\dot{V}_{sm} + \nu_{0m}\dot{C}_{sm}),$$

[a] *Institute of Radio Engineering and Electronics,*
Russian Academy of Sciences,
Mokhovaya ul. 11, Moscow, 125009 Russia
e-mail: kvf@pochta.ru

[b] *Research and Technology Center of Unique*
Instrumentation, Russian Academy of Sciences,
ul. Butlerova 15, Moscow, 117342 Russia
e-mail: kurayev@gw.bsuir.unibel.by;
sinitsyn@bsuir.unibel.by

[c] *Belarussian State University of Information Science*
and Radio Engineering, ul. Brovki 17,
Minsk, 220072 Belarus

$$\dot{C}_{sm} = -\frac{\nu_{0m}\dot{V}_{sm}}{sW\,b^2} + \frac{\partial b}{b\partial z}\left(-\frac{\dot{A}_{sm}}{\nu_{0m}} + \sum_{k\neq m}\frac{2\nu_{0m}}{\nu_{0k}^2 - \nu_{0m}^2}\right.$$

$$\left.\times\frac{J_1(\nu_{0k})}{J_1(\nu_{0m})}\dot{A}_{sk}\right) - \frac{jG_0}{sW e_{0m}b^2}\frac{1}{N}\sum_{i=1}^{N}J_0\left(\nu_{0m}\frac{r_i}{b}\right)e^{-jsW\theta_i},$$

(1)

$$\frac{d\dot{V}_{sm}}{dz} = -sW\left\{\dot{A}_{sm} + \left(\frac{\partial b}{\partial z}\right)^2\left[\dot{A}_{sm}\cdot\frac{1}{3}\left(1 + \frac{4}{\nu_{0m}^2}\right)\right.\right.$$

$$\left.+\sum_{k\neq m}\frac{4(\nu_{0m}^2 + \nu_{0k}^2)}{(\nu_{0m}^2 - \nu_{0k}^2)}\frac{J_1(\nu_{0k})}{J_1(\nu_{0m})}\dot{A}_{sk}\right]$$

$$\left.-b\frac{\partial b}{\partial z}\left(-\frac{\dot{C}_{sm}}{\nu_{0m}} + \sum_{k\neq m}\frac{2\nu_{0k}}{\nu_{0m}^2 - \nu_{0k}^2}\frac{J_1(\nu_{0k})}{J_1(\nu_{0m})}\dot{C}_{sk}\right)\right\}$$

$$+\frac{G_0}{e_{0m}b}\left(\frac{1}{N}\sum_{i=1}^{N}J_1\left(\nu_{0m}\frac{r_i}{b}\right)\left(\frac{\beta_{ri}}{\beta_{zi}} - \frac{r_i}{b}\frac{\partial b}{\partial z}\right)\right)je^{-jW\theta_i}.$$

The equations of motion of large particles are

$$\frac{dP_{ri}}{dz} = \frac{1}{\beta_{zi}}\left(\frac{\gamma_i\beta_{\varphi i}^2}{r_i} - E_r - \beta_{\varphi i}F_z + \beta_{zi}B_\varphi\right),$$

$$\frac{dP_{zi}}{dz} = \frac{1}{\beta_{zi}}(-E_z - \beta_{ri}B_\varphi + \beta_{\varphi i}F_r),$$

$$\frac{dr_i}{dz} = \frac{\beta_{ri}}{\beta_{zi}}, \quad \frac{d\theta_i}{dz} = \frac{1}{\beta_{zi}},$$

(2)

$$\mathbf{P}_i = \gamma_i\boldsymbol{\beta}_i, \quad \beta_{\varphi i} = \frac{F_0(z)[r_i^2 - r_i^2(0)]}{\gamma_i r_i},$$

$$\gamma_i = \frac{1}{\sqrt{1 - \boldsymbol{\beta}_i^2}} = \sqrt{1 - P_{ri}^2 - P_{\varphi i}^2 - P_{zi}^2}.$$

Then, we express the physical high-frequency fields in terms of the calculated amplitudes with allowance for space-charge fields:

$$E_r = -\frac{1}{b}\sum_{s=1}^{S}\sum_{m=1}^{M}J_1\left(\nu_{0m}\frac{r_i}{b}\right)\mathrm{Re}(\dot{A}_{sm}e^{jsW\theta_i})$$

$$-\frac{G_0}{2r_i}\left(\frac{1}{\beta_0} - \beta_{z0}\right),$$

$$E_z = \mathrm{Re}\left[\sum_{s=1}^{S}\sum_{m=1}^{M}J_0\left(\nu_{0m}\frac{r_i}{b}\right)\dot{C}_{sm}e^{jsW\theta_i}\right.$$

(3)

$$\left.+\frac{r_i}{b^2}\frac{\partial b}{\partial z}\sum_{s=1}^{S}\sum_{m=1}^{M}J_1\left(\nu_{0m}\frac{r_i}{b}\right)\dot{A}_{sm}e^{jsW\theta_i}\right],$$

$$B_\varphi = \frac{1}{b}\sum_{s=1}^{S}\sum_{m=1}^{M}J_1\left(\nu_{0m}\frac{r_i}{b}\right)\mathrm{Re}(-j\dot{V}_{sm}e^{jsW\theta_i}).$$

The magnetostatic focusing field is

$$F_r = -\frac{1}{2}r_i\frac{\partial F_0(z)}{\partial z} + \frac{1}{16}r_i^3\frac{\partial^3 F_0(z)}{\partial z^3},$$

$$F_z = F_0(z) - \frac{1}{4}r_i^2\frac{\partial^2 F_0(z)}{\partial z^2},$$

$$F_0 = \frac{B_0(z)e}{m_0\omega_0}.$$

Here, $B_0(z)$ is the field along the axis; $W = \dfrac{\omega}{\omega_0}$; ω and ω_0 are the operating and reference frequencies, respectively; s is the number of an operating-frequency harmonic; m is the radial index of the E_{0m} wave; ν_{0m} is the mth root of the function $J_0(x)$; $e_{0m} = 0.5J_1^2(\nu_{0m})$; $k_0 = \dfrac{\omega_0}{c}$; $r = k_0r'$; $z = k_0z'$ (primes stand for dimensional quantities having denotations that are identical to the dimensionless ones); $b(z) = k_0b'(z)$; $b'(z)$ is the inner waveguide radius (waveguide profile); $\dot{A}_{sm} = \dfrac{b'\dot{E}_{rsm}e}{m_0c^2}$; $\dot{C}_{sm} = \dfrac{\dot{E}_{zsm}e}{\omega_0 m_0c}$; $\dot{V}_{sm} = \dfrac{b'\dot{B}_{\varphi ms}e}{m_0c}$; $\dot{E}_{rsm}$, $\dot{E}_{zsm}$, and $\dot{B}_{\varphi sm}$ are the amplitudes for the partial-wave components; e and m_0 are the electron charge and rest mass; c is the speed of light; $G_0 = \dfrac{eI_0}{\pi\varepsilon_0 m_0c^3}$, I_0 is the beam current in amperes; $r_0 = k_0r_0'$; r_0' is the mean radius of the tubular electron flux at the input of the interaction region; $\theta_i = \omega_0t_i$; t_i is the time of flight for the ith large particle through the cross-section z; $\beta_i = \dfrac{\upsilon_i}{c}$; and υ_i is the velocity of the ith particle.

Excitation equations (1) involve both the vortex and the potential (the space-charge field) components of the total field at the frequency $s\omega_0W$. The boundary conditions related to the sets of Eqs. (1), (2) can be formulated in the following manner. At the boundaries of the

conjugation of the irregular region of the interaction with the regular waveguide, the condition

$$\frac{db(0)}{dz} = \frac{db(L)}{dz} = 0$$

is fulfilled, and the following relationships occur:

(i) for propagating E_{0m} waves:

$$W\dot{A}_{sm}(0) + jk^e_{sm}\dot{V}_{sm}(0) = jk^e_{sm}W \cdot 2b(0)\dot{e}^+_{sm},$$
$$-W\dot{A}_{sm}(L) + jk^e_{sm}\dot{V}_{sm}(L) = jk^e_{sm}W \cdot 2b(L)\dot{e}^-_{sm}; \quad (4)$$

(ii) for supercritical E_{0m} waves:

$$W\dot{A}_{sm}(0) + k^e_{sm}\dot{V}_{sm}(0) = k^e_{sm}W \cdot 2b(0)\dot{e}^+_{sm},$$
$$-W\dot{A}_{sm}(L) + k^e_{sm}\dot{V}_{sm}(L) = k^e_{sm}W \cdot 2b(L)\dot{e}^-_{sm}. \quad (5)$$

Here, $k^e_{sm} = \sqrt{\left|(sW)^2 - \left(\frac{v_{0m}}{b}\right)^2\right|}$, $\dot{e}^+_{sm}$, $\dot{e}^-_{sm}$ are the relative amplitudes of the direct and opposite propagating waves and supercritical waves at the regular segments conjugated with the interaction region. For the unmodulated electron beam, we have at the input of the interaction region

$$W\theta_i(0) = \frac{2\pi}{N}(i - 0.5), \quad i = 1, 2, \ldots, N,$$
$$\beta_i(0) = \beta_0, \quad r_i(0) = r_{0i}. \quad (6)$$

Thus, for the set of Eqs. (1) with respect to the amplitudes, the boundary value problem is posed, and for the equations of state (2) for large particles, the Cauchy problem is formulated. The combined solving is performed as a result of the iteration procedure. The interaction efficiency is determined by the following relations:

(i) in terms of the power of excited wave fluxes (the so-called wave efficiency):

$$\eta^v_{sm}(z) = e_{0m}\frac{\text{Im}[\dot{A}_{sm}(z)\dot{V}^*_{sm}(z) - \dot{A}_{sm}(0)\dot{V}^*_{sm}(0)]}{(\gamma_0 - 1)G_0},$$
$$\eta^v = \sum_s\sum_m\eta^v_{sm}, \quad (7)$$

(ii) in terms of the kinetic-energy loss by the electron beam (the so-called electronic efficiency):

$$\eta^e(z) = \frac{1}{N}\sum_{i=1}^N\frac{\gamma_0 - \gamma(z)}{\gamma_0 - 1}. \quad (8)$$

The phase grouping of electrons is determined by the grouping function

$$G_{rs}(z) = \frac{1}{N}\left[\left(\sum_{i=1}^N\cos sW\theta_i\right)^2 + \left(\sum_{i=1}^N\sin sW\theta_i\right)^2\right]^{1/2}. \quad (9)$$

In the case of a small energy exchange, the quantity G_{rs} is close to the relative *s*th harmonic of the beam current.

APPROXIMATION OF THE CONTROL

Problem (1)–(6) with the indicated goal function $\max F_e[\mathbf{g}(z)]$ (usually $F_e = \eta^e$) belongs to the problems of optimal control. In this problem, the normalized waveguide profile $b(z)$ of the waveguide or the profile $F(z)$ of the focusing magnetic field is the object of the desired control $\mathbf{g}(z)$. In the approximation of the controls, we used splines of the third and fifth orders. The profile of the irregular corrugated-waveguide segment was set in the form

$$b(T) = b_0 + h_v(T)\sin^2[n_v\pi(T + D_v(T))], \quad (10)$$

where $T = \dfrac{z - z_0}{L_v}$; z_0 and L_v are the beginning coordinate and the length of the corrugated waveguide segment, respectively; n_v is the number of periods; $h_v(T)$ is the corrugation depth; $D_v(T)$ is the function determining the period variation; e.g., $D_v(0) = 0$, $D_v(1) = 0$; for $D_v(T) = 0$, the period is constant and is equal (in the accepted units) to $d_v = \dfrac{L_v}{n_v}$. The functions $h_v(T)$ and $D_v(T)$ were set in the form of an expansion in shifts of the standard finite function $\varphi_3(x)$ that corresponded to B-splines of the third order [8]:

$$h_v(T) = \sum_{k=1}^K h^v_k\varphi_3[T(K - 3) - k + 2],$$
$$D_v(T) = \sum_{k=1}^K d^v_k\varphi_3[T(K + 3) - k - 1], \quad (11)$$

$$\varphi_3(x) = \begin{cases} 0, \quad |x| \geq 2, \quad \dfrac{(2 - x)^3}{6}, \quad 1 \leq x \leq 2; \\ \dfrac{1}{6}[1 + 3(1 - x) + 3(1 - x)^2 - 3(1 - x)^3], \\ 0 \leq x \leq 1; \\ \varphi_3(-x), \quad x \leq 0. \end{cases}$$

For this approximation, the values of the coefficients h^v_k and d^v_k correspond to those of the functions

$h_\nu\left(\dfrac{k-2}{K-3}\right)$ and $D_\nu\left(\dfrac{k+1}{K+3}\right)$, respectively. The conjugation of the regular waveguide segments of different radii b_1, b_2 were set in the form $b = b_1 + (b_2 - b_1)P_5(T)$, $T = \dfrac{z - z_0}{L_c}$; z_0 and L_c are the onset coordinate and the length of the conjugation segment. The fifth-order polynomial

$$P_5(T) = T^3(10 - 15T + 6T^2), \quad \frac{\partial P_5}{\partial T} = 30T^2(1 - T)^2,$$

$$\frac{\partial^2 P_5}{\partial T^2} = 60T(1 - 3T + 2T^2)$$

ensures the continuity of the first and second derivatives at the conjugation points. Using these conjugations on the waveguide profile, we simulated resonance grooves and asperities of a certain configuration. In this case, the configuration is determined by the physical parameters $h_k = |b_2 - b_1|$, $\Delta_p = \dfrac{L_k - 2L_c}{L_k}$. Here, L_k is the groove width, h_k is the groove height, and Δ_p is the parameter featuring the steepness of groove walls. Using these conjugations of grooves, as well as splines of the form $D_\nu(T)$, $h_\nu(T)$ (11), we simulated retarding quasi-periodic meander structures, mode transformers, and horn-shaped outputs.

SETTING THE PROBLEM
FOR GRID CALCULATIONS

In the accepted notation, the dimensionless components E_r, E_z, B_φ of the symmetric E-wave fields of a cylindrical longitudinally irregular waveguide (at the fundamental frequency $s = 1$) are found by solving the following boundary value problem:

$$\dot{B}_\varphi = \frac{u(r, z)}{r}, \quad \dot{E}_r = \frac{j}{W}\frac{1}{r}\frac{\partial u}{\partial z}, \quad \dot{E}_z = -\frac{j}{W}\frac{1}{r}\frac{\partial u}{\partial r},$$

$$u(z, r) = u_{re} + ju_{im}.$$

In the region $0 \le r \le b(z)$, $0 \le z \le L$, we have

$$\frac{\partial}{\partial z}\left(\frac{1}{r}\frac{\partial u}{\partial z}\right) + \frac{\partial}{\partial r}\left(\frac{1}{r}\frac{\partial u}{\partial r}\right) + \frac{W^2}{r}u = 0. \quad (12)$$

The boundary conditions are the following. For $r = 0$, $u = 0$, at the conducting boundary, $r = b(z)$, $\dfrac{\partial u}{\partial \mathbf{n}} = 0$ ($\mathbf{n}$ is the vector of the normal to the surface). For $z = 0$ and in the case of the incident E wave, $-\dfrac{\partial u}{\partial z} + jk_m^e u =$

$e^+ rJ_1(\nu_{0m}r)$. For $z = L$, $\dfrac{\partial u}{\partial z} + jk_m^e u = 0$ (the condition of complete matching for the E_{0m} wave). The power transferred through the waveguide cross section is

$$P = \text{real} \int_0^{b(z)} E_r B_\varphi^* r dr$$

$$= \frac{1}{W} \int_0^{b(z)} \left(u_{im}\frac{\partial u_{re}}{\partial z} - u_{re}\frac{\partial u_{im}}{\partial z}\right)\frac{\partial r}{r}. \quad (13)$$

NUMERICAL EXPERIMENT

To verify the adequacy of set (1), we solved the problem of the reflection of the E_{01} wave of a regular cylindrical waveguide of radius b_0 from an inhomogeneity of k sinusoidal-shape grooves of depth h and width d:

$$b(z) = \begin{cases} b_0, & z < z_1, \\ b_0 + h\sin^2\dfrac{\pi(z - L_1)}{d}, & z_1 \le z \le z_1 + kd, \\ b_0, & z_1 + kd < z < L. \end{cases} \quad (14)$$

The values of z_1 and L were chosen based on the condition of the attenuation of supercritical waves excited on the inhomogeneities, so that only E_{01} waves of the regular waveguide could be observed in the cross sections with the coordinates $z = 0$, $z = L$. Figure 1 presents the curves for the power transferred (13) normalized to that of the regular waveguide as a function of the groove height h. Curves *1* are calculated with allowance for 8 basis functions. The second curve is obtained from the solution of the boundary value problem by the method of finite triangular elements with the use of the MATHLAB program package. The values $z_1 = 1.5b_0$ and $L = 2z_1 + kd$ were chosen. The number of partition elements in this region equaled 2750. When the number of partition elements reached 4000, all curves in Fig. 1 coincided with each other; i.e., the results obtained by the finite-element method converge to those found from Eqs. (1).

NONFULFILLMENT
OF THE SECOND-KIND PERIODICITY
CONDITION IN MATCHED SEGMENTS
OF PERIODIC WAVEGUIDES

It was indicated previously, in [7, 15], that the second-kind periodicity condition is fulfilled neither in the general case (EH_{nm} and HE_{nm} waves [15]), nor in the case of E_{0m} waves [6]. To confirm these statements, we now present the data of calculations for matched seg-
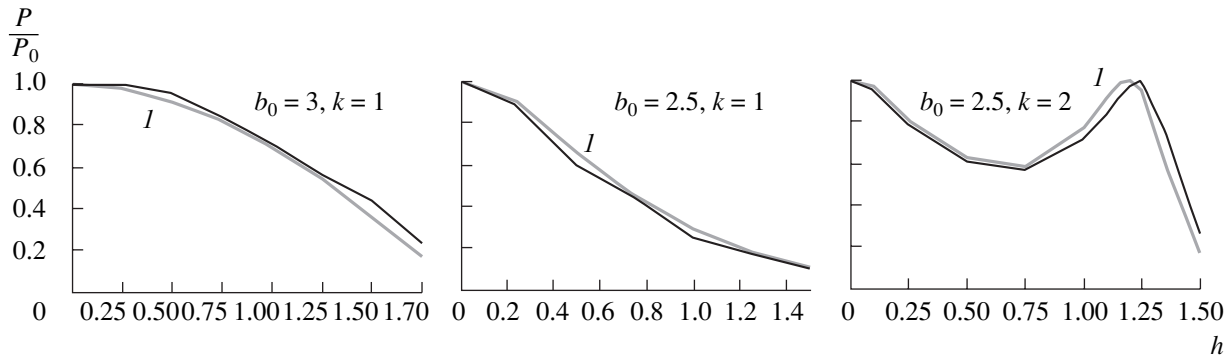
Fig. 1. Beam power transferred through the waveguide cross section as a function of the groove depth for $d = 2$.
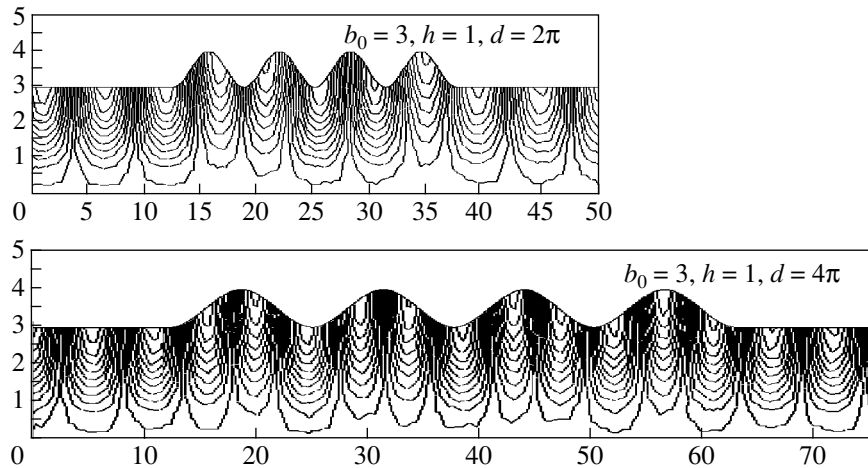

Fig. 2. Level lines real$[u(r, z)]$ obtained by the grid method.

ments of periodic corrugated waveguides operating in the E_{0m} mode. The calculations were performed by solving problem (12) on the basis of both the grid method and the Galerkin method. In Fig. 2, the structure of level lines for the function real$[r\dot{B}_\varphi(r, z)]$ is shown. The structure was obtained by calculations according to the grid method for two waveguide configurations (these lines are close to the **E**-field lines). Figure 3 illustrates the variation of the modulus $|\dot{E}_z(r_0, z)|$ of the longitudinal-component along the corrugated-waveguide segment (calculations by the Galerkin method). It is worth noting that calculations of this waveguide with high accuracy by the grid method turn out to be rather complicated, which is associated with limitations in the capacities of modern computers. As follows from Figs. 2, 3, the periodicity of the distributions over $r\dot{B}_\varphi$ and $\dot{E}_z$ for these two cases is absent in the corrugated section. As was noted previously, in [5, 6, 15], this conclusion is important for the formulation of an adequate self-consistent theory of RWLs and IWLs. In this connection, the theoretical results of [12–14] based on the concept of synchronous spatial field harmonics

in the retarding system of IWLs or RWLs are erroneous.

CALCULATION AND OPTIMIZATION OF RELATIVISTIC GENERATORS BASED ON RWLS AND IWLS WITH CORRUGATED WAVEGUIDES

Using the self-consistent set of Eqs. (1)–(3) and the attached boundary conditions (4)–(6), and on the basis of the block matrix sweep, the following generator variant is proposed. The operating frequency is $f = 37.96$ GHz, and the chosen reference frequency ω_0 corresponds to the wavelength $\lambda_0 = 7.99$ mm. The beam-accelerating voltage is 212 kV, the beam current is $I_0 = 600$ A, and the induction of the focusing magnetic field is $B_0 = 5$ T. The regular corrugated segment has $n_v = 12$ periods, $d_v = 2.756$, $h_v = 1.18$, and $b_0 = 2.3615$ (3.5, 1.5, 3 mm). The radius of the waveguide at its end is $b_L = 2.952$ (3.75 mm). The width, the height of the modulating groove, and its distance from the comb onset are $L_1 = 4.72$, $h_1 = 1.46$, $L_{1v} = 5.51$ (6, 1.86, 7 mm), and $\Delta_p = 0.8$. The beam radius is $r_0 = 2.06$ (2.62 mm). The
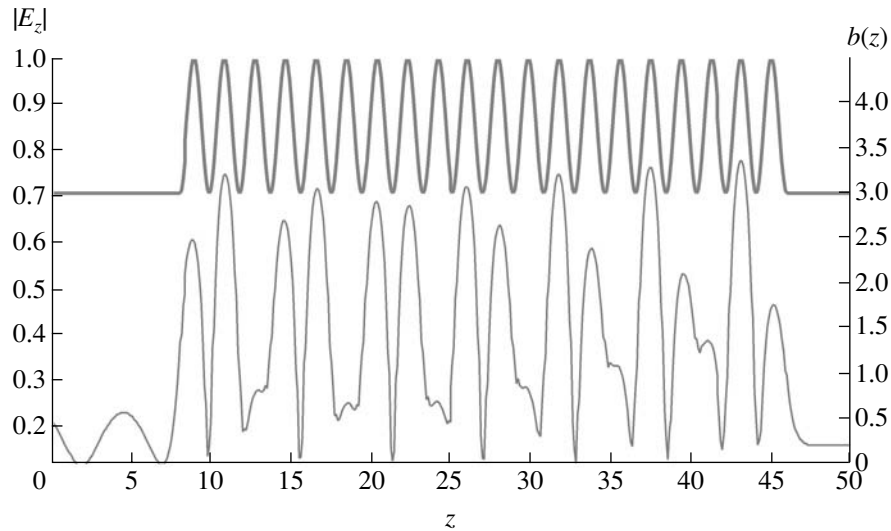
Fig. 3. Variations of the modulus of the E_z-wave field component along the corrugated-waveguide segment ($b_0 = 3$, $d = 1.9$) at the level $r_0 = 2.5$.
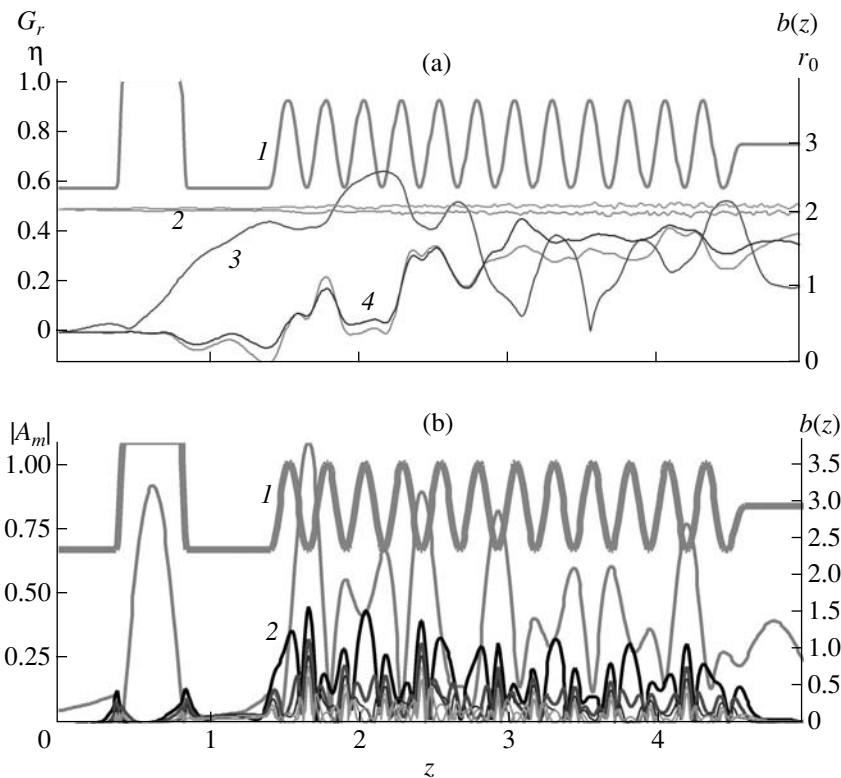
Fig. 4. Characteristics of the variant of the 8-mm wave generator. (a): (*1*) $b(z)$; (*2*) r_{max}, r_{min}; (*3*) G_{r1}; (*4*) η^e, η^v; (b): (*1*) $b(z)$; (*2*) A_m.

efficiency attained is 36%. As our analysis shows, the synchronism is realized at the first harmonic far from the boundary of the transparency band. At the inner radius $b_0 = 2.36$ mm, the waveguide is supercritical. Therefore, to extract the microwave power, the waveguide radius is increased immediately beyond the corrugated segment. The features of this variant are exhibited in Fig. 4. The results obtained for this variant were verified by calculations of the PIC and KARAT

cones based on the finite-element method. In both cases, a complete agreement was observed (the efficiency attains 36%).

CONCLUSIONS

Thus, in this paper, the stability is shown and the convergence rate is determined for projection methods in problems of the theory and optimization of relativis-

tic devices of the "O" types, which are based on irregular (both periodic and aperiodic) waveguides. An important advantage of this method as compared to grid methods should be noted here. It consists not only in the fact that the three-dimensional problem is reduced to a one-dimensional (two-point) problem, although this represents a significant argument in favor of improving the calculation procedure. The other property is more important. In multiwave regimes, boundary conditions of the type of the radiation conditions at the end of the irregular-waveguide segment are not determined *a priori*. In addition, they differ at different points of the cross section, which impedes the employment of the grid methods. In the projection methods, in which waves are separated, this problem does not exist at all. Given the latter, it is rather difficult to solve the problem of waveguide excitation on the basis of the self-consistent RWL theory and grid methods.

REFERENCES

1. A. A. Kuraev, Izv. Akad. Nauk BSSR, Ser. Fiz.-Tekh. Nauk, No. 1, 121 (1979).
2. A. A. Kuraev, *Theory and Optimization of Microwave Electronic Devices* (Nauka i Tekhnika, Minsk, 1979) [in Russian].
3. A. A. Kuraev, *High-power Microwave Devices. Methods of Analysis and Parameter Optimization* (Radio i Svyaz', Moscow, 1986) [in Russian].
4. A. A. Kuraev, Vestsi NAN Belarusi, Ser. Fiz.-Tekh. Navuk, No. 4, 60 (1999).
5. A. A. Kuraev and A. K. Sinitsyn, Élektromagn. Volny i Élektron. Sistemy **7** (3), 12 (2002).
6. M. P. Batura, A. A. Kuraev, and A. K. Sinitsyn, in *Proceedings of 14th International Conference on Microwave and Telecommunication Technologies, Sevastopol, Ukraine, 2004* (Sevastopol, 2004), p. 175.
7. M. P. Batura, A. A. Kuraev, I. V. Lushchitskaya, *et al.*, Dokl. BGUIR, No. 4, 26 (2004).
8. G. I. Marchuk and V. I. Agoshkov, *Introduction to Projection-Grid Methods* (Nauka, Moscow, 1981) [in Russian].
9. A. S. Il'inskiĭ and G. Ya. Slepyan, *Oscillations and Waves in Electrodynamic Systems with Energy Loss* (Mosk. Gos. Univ., Moscow, 1983) [in Russian].
10. S. P. Bugaev, V. I. Kanavets, A. N. Klimov, *et al.*, in *Relativistic High Frequency Electronics* (Gorky, 1988), p. 78 [in Russian].
11. R. A. Silin and V. P. Sazonov, *Retarding Systems* (Sovetskoe Radio, Moscow, 1966) [in Russian].
12. V. A. Solntsev, N. L. Romashin, and N. P. Kravchenko, *Lectures on Microwave Electronics and Radio Physics* (Saratovskiĭ Gos. Univ., Saratov, 1983) [in Russian].
13. L. A. Vaĭnshteĭn and V. A. Solntsev, *Lectures on Microwave Electronics* (Sovetskoe Radio, Moscow, 1973) [in Russian].
14. V. A. Solntsev, Radiotekh. Elektron. (Moscow) **43**, 1285 (1998).
15. S. V. Kolosov and A. A. Kuraev, Élektromagn. Volny i Élektron. Sistemy **4** (3), 44 (1999).

Translated by G. Merzon

================= **PHYSICS** =================

Stabilization of Turbulent Dynamics in Excitable Media by an External Point Action

A. Yu. Loskutov, R. V. Cheremin, and S. A. Vysotskiǐ

Presented by Academician A.R. Khokhlov May 13, 2005

Received May 16, 2005

In this paper, the behavior of an excitable medium in the state of developed spatio-temporal chaos is analyzed. We show that a weak point action on the medium results in the suppression of all spiral waves and stabilization of the system dynamics. The analysis performed is based on the identification of the number of spiral waves in the medium.

The stabilization of the turbulent dynamics of active media, which is based on a weak periodic point action, is a rather important direction of research, finding its application in cardiology. At present, in the theory of excitable systems, a hypothesis dominates according to which the appearance of a fatal cardiac arrhythmias is associated with the generation in the heart tissue of a great number of autowave sources, namely, spiral waves and vortex structures (i.e., spatio-temporal chaos) (see, e.g., [1, 2] and references therein).

Modern methods for the stabilization of such regimes based on single electric pulses (including those based on implanted defibrillators) are rather arduous and not always successful. However, recent studies open novel potentialities in this field of medical science. There is no necessity in high-amplitude pulsed action, and, in many cases, the action can be weakened [3]. Moreover, in a number of excitable media, the turbulent regime can be stabilized by a rather weak periodic parametric action [4, 5] or by a force action applied at a certain domain of a medium [6–8].

In this study, we exploit the simple theoretical model of the FitzHugh–Nagumo type [9, 10] for an excitable medium. We show that the spatio-temporal chaos arising as a result of the decay of spiral waves can be suppressed by means of a point action having a rather low amplitude. In addition, the problem of seeking frequencies that provide for the efficient suppression of all spiral waves is solved. Upon this stabilization, the medium remains in the spatially homogeneous state.

The FitzHugh–Nagumo model describes a two-component system of the activator–inhibitor type:

$$\frac{\partial U}{\partial t} = \Delta U - U(U-\alpha)(U-1) - V,$$
$$\frac{\partial V}{\partial t} = \beta U - \gamma V. \tag{1}$$

As applied to the heart-muscle dynamics, variable U corresponds to the action potential for muscular cells.

Although this model well describes (at the qualitative level) the excitation propagation in the muscular tissue and demonstrates basic types of structures arising in excitable media of the activator–inhibitor type, it is unsuitable for quantitative description. This is associated with the fact that this model does not allow for certain important properties of the heart tissue, such as the dependence of the refractoriness period on both the amplitude and duration of the excitation phase.

In order to obtain a more adequate description, the set of Eqs. (1) is usually represented in the form

$$\frac{\partial U}{\partial t} = \Delta U - f(U) - V,$$
$$\frac{\partial V}{\partial t} = g(U, V)(kU - V).$$

In this case, the form of the functions f and g is chosen with a goal to providing for the consistency of the action-potential profiles to be obtained with experimental data.

Recently, the model developed in [11] has been widely employed, it having been proposed there that

_____

Moscow State University,
Vorob'evy gory, Moscow, 119992 Russia
e-mail: loskutov@moldyn.phys.msu.ru
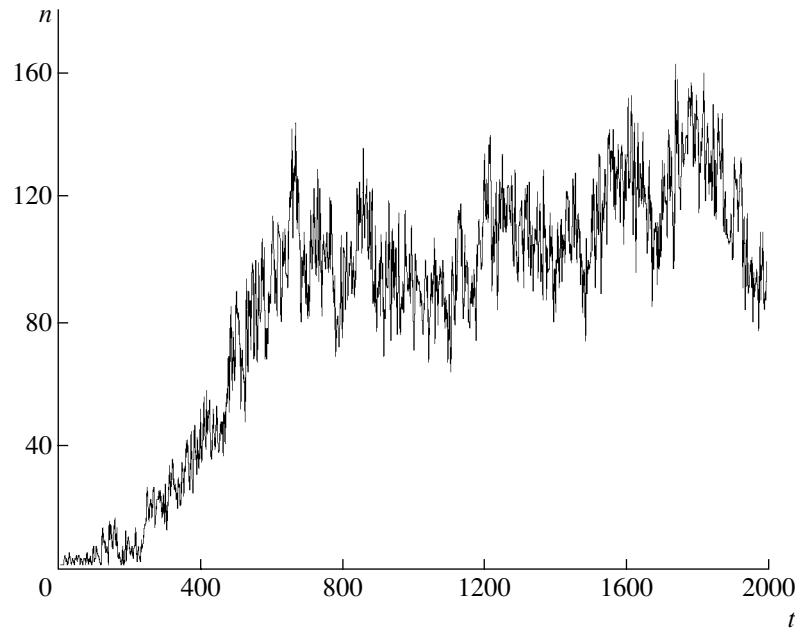
Fig. 1. Number of spiral-wave cores as a function of time in the case of the decay of a single spiral wave and generation of chaos ($G_1 = 1/50$, $G_3 = 0.3$).

the following piece-wise linear functions be used for the functions f and g:

$$f(U) = \begin{cases} C_1 U, & U < U_1, \\ -C_2 U + a, & U \in (U_1 U_2), \\ C_3(U-1), & U > U_2, \end{cases}$$

$$g(U,V) = \begin{cases} G_1, & U < U_1, \\ G_2, & U_1 > U_2, \\ G_3, & U < U_1, V < V_1. \end{cases} \tag{2}$$

One of the advantages of this description is the presence of two independent relaxation parameters. One of them (G_3) determines the relaxation period for small values of U and V. The other parameter (G_1) determines the absolute value of the relaxation parameter for large values of V and intermediate values of U, which corresponds to the leading and trailing wave fronts.

To ensure a correspondence with actual media (e.g., heart tissue), the following values of the parameters related to the set of Eqs. (2) are usually chosen: $C_1 = 20$, $C_2 = 3$, $C_3 = 15$, $U_1 = 0.0026$, $U_2 = 0.837$, $V_1 = 1.8$, $a = 0.06$, and $k = 3$. In this case, G_1 ranges from $\frac{1}{75}$ to $\frac{1}{33}$, $G_2 = 1$, and $0.1 \leq G_3 \leq 2$.

We have analyzed the dynamics of this system in a rectangular plane domain of the size of 350×350 nodes. In order to exclude edge effects at the boundaries, we set the periodic conditions; i.e., the domain under study had the torus topology.

In the chosen range of parameter values, the auto-wave solutions of the spiral-wave type are unstable. As time elapses, they decay into smaller waves and, as a result, the regime of spatio-temporal chaos is developed in the system. The spiral waves are the basic types of the autowave solutions in the given system. This opens the possibility of using their number as a criterion of the complexity of the regime existing in the system [12–15]. The calculation algorithm is based on the fact that the core of a spiral wave (as an arbitrary singularity point of the wave-front) is a singularity for the phase field:

$$\varphi(x, y, t) = \arctan 2 \left(U(x, y, t) - U^*, V(x, y, t) - V^* \right).$$

In this case, the quantity $n = \frac{1}{2\pi} \oint \nabla \varphi \, dl$, called the topological charge, differs from zero only when the integration contour envelopes the singularity. This is the case when n is an integer, and its sign determines the chirality of the spiral wave. The time dependence for the calculated number of spiral-wave cores is plotted in Fig. 1. The plot corresponds to the appearance of the chaotic regime arising from a decaying single spiral wave.

This chaotic regime is further used as the initial state in the analysis of a system with a point periodic action of the rectilinear-step shape:

$$I_{\mp}(t) = A(2\theta(t - T\tau) - 1).$$

Source of excitation
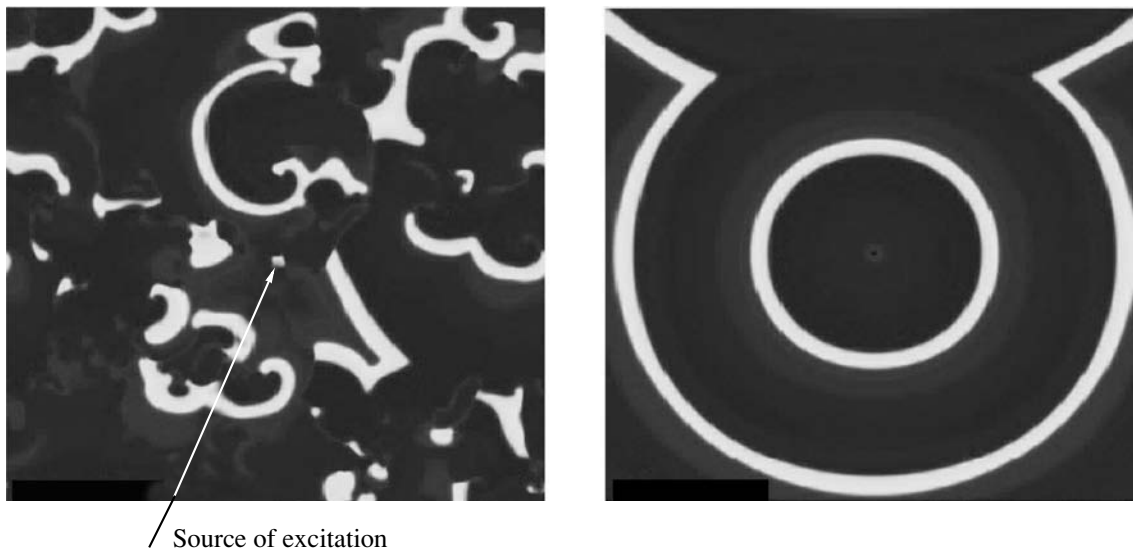
Fig. 2. Results of the action on a system with developed spatio-temporal chaos ($G_1 = 1/50$, $G_3 = 0.3$, $A = 6$).

Here, $A = 6$ is the amplitude, θ is the Heaviside step function, and τ varies within the range from 0.1 to 0.9. The action was applied to the domain enveloping 2×2 nodes. As applied to the heart tissue, this action is weaker than in the case of an implanted defibrillator by a factor of 1000.

Insofar as arbitrarily (in the dark) seeking suppression frequencies is extremely inefficient, we employed a method that made it possible to preliminarily localize the range of frequencies providing the suppression. The concept of this method is based on a well-known property of excitable media: in the case of competing wave sources, only the source with the highest frequency of the generated waves survives. Thus, the most favorable frequencies of the external action (from the standpoint of suppressing spiral waves) are those for which the frequency of excited circular waves in the medium is close to the maximum possible frequency for the given parameters of the medium.

In order to determine these frequencies, we generated circular waves in a small volume of the medium and found the dependence of the frequency ν of the waves being obtained on the frequency ω of the point source. The frequency intervals in the vicinity of the maxima of this dependence served as candidates for a more detailed study. It is worth noting that the simulation in a small volume of the medium over the course of several tens of periods is sufficient for constructing the function $\nu(\omega)$. However, to verify the presence or absence of the suppression effect at the given frequency, it is necessary to consider large volumes of the medium over the course of several thousands of periods, since otherwise the turbulent regime is not developed.

The set of Eqs. (2) was investigated for values of the parameters $G_1 = \{1/75, 1/50, 1.33\}$ and $G_3 = \{0.1, 0.3,$

0.5, 1.0, 1.5, 2.0}, i.e., on the calculation mesh with 18 nodes. For all of them, the effect of suppression of the spatio-temporal chaos was observed (Fig. 2) at frequencies in the vicinity of the maximum for the function $\nu(\omega)$ (Fig. 3). The number of cores for spiral waves as a function of time in the system with a point action is shown in Fig. 4.

The numerical analysis performed has demonstrated that the stabilization of the dynamics is also possible if two or more excitation sources are introduced into the medium. However, in this case, the suppression efficiency noticeably depends on the distance between the sources. When they are spaced for a sufficient distance, the effective action turns out to be stronger than in the
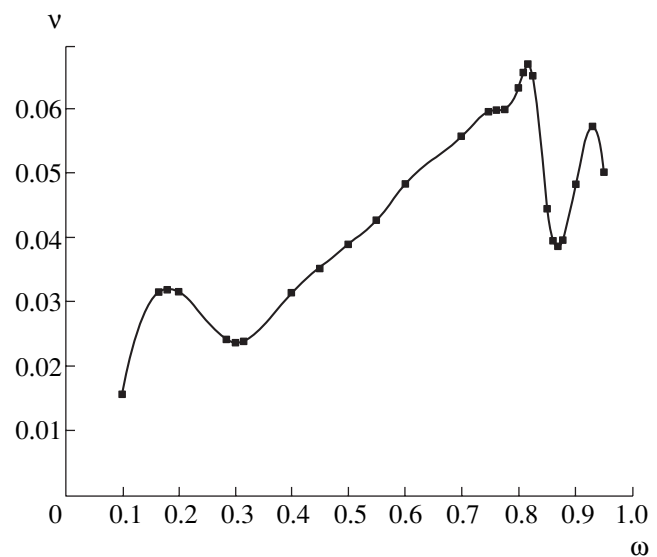
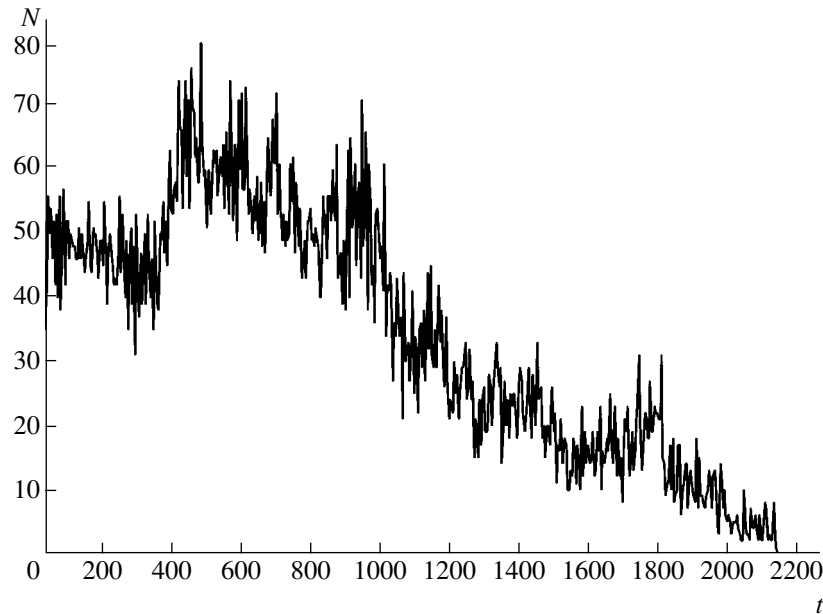**Fig. 3.** Dependence $\nu(\omega)$ ($G_1 = 1/50$, $G_3 = 0.3$).

Fig. 4. Number of spiral waves as a function of time in the case of the point action ($G_1 = 1/50$, $G_3 = 0.3$, $A = 6$).

case of a single source, so that the suppression of spiral waves occurs more rapidly by a factor of 3–5. If the sources are placed closely to each other, they begin to compete, thereby terminating the generation of circular waves.

An additional series of numerical experiments was carried out with an extended source in the form of a thin filament. It was found that the suppression efficiency rapidly dropped as the filament length was increased. For example, filaments of length $10l$ and longer, where l is the wave-front width, yielded the inverse effect; namely, the number of spiral-wave cores increased.

Thus, the most efficient method for the stabilization of the turbulent dynamics of excitable media is that of suppressing spiral waves by a weak point action in the form of a single or several sufficiently spaced small-size sources. In the future, we hope to find conditions that will allow us to reduce even more the amplitudes of the negative half-wave. This will result in a decrease in the total power of the action due to choosing a special pulse shape, and, hence, will allow us to suppress the spatio-temporal chaos by means of purposefully chosen low-intensity pulses. It would appear to be impossible to attain this effect with ordinary sinusoidal-shape pulses.

REFERENCES

1. A. T. Winfree, *When Time Breaks Down: The Three-Dimensional Dynamics of Electrochemical Waves and Cardiac Arrhythmias* (Princeton Univ. Press, Princeton, 1987).

2. D. P. Zipes and J. Jalife, *Cardiac Electrophysiology—from Cell to Bed-Side* (W.B. Saunders Co., Philadelphia, 1995).

3. S. Takagi, A. Pumir, D. Pazo, *et al.*, Phys. Rev. Lett. **93**, 058 101 (2004).

4. S. Alonso, F. Sagues, and A. S. Mikhailov, Science **299**, 1722 (2003).

5. N. A. Kovaleva and A. Yu. Loskutov, Dokl. Akad. Nauk **396**, 68 (2004).

6. A. T. Stamp, G. V. Osipov, and J. J. Collins, Chaos **12**, 931 (2002).

7. G. V. Osipov and J. J. Collins, Phys. Rev. E **60**, 54 (1999).

8. H. Zhang, B. Hu, and G. Hu, Phys. Rev. E **68**, 026134 (2003).

9. R. FitzHugh, Biophys. J. **1**, 445 (1961).

10. V. A. Vasil'ev, Yu. M. Romanovskiĭ, and V. G. Yakhno, *Autowave Processes* (Nauka, Moscow, 1987) [in Russian].

11. A. V. Panfilov and P. Hogeweg, Phys. Lett. A **176**, 295 (1993).

12. M.-A. Bray, S.-F. Lin, R. R. Aliev, *et al.*, J. Cardiovasc. Electrophysiol. **12**, 716 (2001).

13. R. Zou, J. Kneller, L. J. Leon, and S. Nattel, Chaos **12**, 764 (2002).

14. M.-A. Bray, IEEE Trans. Biomed. Eng. **49**, 1086 (2002).

15. R. H. Clayton and A. V. Holden, Phys. Med. Biol. **47**, 225 (2002).

Translated by G. Merzon

Crystal Symmetry and the Structure of Two-Electron States in High-Temperature Superconductors

V. G. Yarzhemsky* and Academician V. I. Nefedov

Received April 21, 2005

1. The main characteristic of unusual superconductors such as heavy-fermion superconductors and high-temperature superconductors (HTSCs) is that the superconducting order parameter (SOP) vanishes at points and lines of the Fermi surface [1–3]. For spherically symmetric interaction, the SOP coincides with the wave function of a Cooper pair.

Photoelectron spectroscopic investigations [2] of HTSC materials and measurements of their conductivity [3] revealed that both the wave function of the pseudogap (for $T^* > T_c$) and the SOP (for $T < T_c$) vanish on the diagonal of a square in the Cu–O bond plane. This characteristic of the pseudogap holds even in the presence of a magnetic field breaking superconductivity [3] and was attributed by the authors of [3] to the crystal symmetry. Thus, the vanishing of the SOP is associated with the features of the electronic structure of HTSCs for $T > T_c$. Since we are analyzing the property of HTSCs that holds for $T > T_c$, we use the term "two-electron wave function" instead of the term "Cooper pair" or the SOP. We consider only those two-electron states that are continuously transformed to Cooper pairs for $T < T_c$, i.e., those that satisfy the symmetry conditions formulated by Anderson [4].

There are two approaches to the generalization of the Anderson method to the crystal symmetry: the point-group approach [5, 6] and space-group approach [7–9]. The point-group approach is based on the representation of the SOP in terms of the basis functions of the irreducible representations of point groups. Although the point-group approach correctly reproduces the nodal structure of the order parameter in some cases, its results depend on the choice of the basis functions and are ambiguous [10]. The space-group approach [7–9], which is based on the induced-representation method [11], is free of the above disadvantages and allows basis-independent conclusions on the nodal structure of two-electron states.

Kurnakov Institute of General and Inorganic Chemistry,
Russian Academy of Sciences,
Leninskiĭ pr. 31, Moscow, 119907 Russia
* e-mail: vgyar@igic.ras.ru

In this work, using the projection-operator method, a new variant of the space-group approach has been developed using the singlet and triplet Anderson two-electron functions [4], on which the projection operators of a point group of a crystal act. Such an approach makes it possible to take into account the crystal symmetry and to obtain the dependence of the pair wave function on all prongs of the wavevector star. The possible singlet and triplet pair wave functions have been constructed for the D_{2h} and D_{4h} symmetries and their nodal structure has been analyzed. The theoretical results are used to interpret experimental data on the symmetry of two-electron states in HTSC materials.

2. In the spherically symmetric case, two electrons with opposite momenta are coupled to a Cooper pair [4]. The pair wave function is antisymmetric under permutations, is invariant under lattice translations, and is transformed according to an irreducible representation of a point group. Excluding symmetric points in the Brillouin zone, where small irreducible representations are two-dimensional [7], the wave function of the singlet and triplet pairs is even and odd, respectively [4–6].

In the *L–S* coupling approximation, the singlet two-electron function and three components of the triplet function are written in the form

$$\Psi^s = \Phi^s S_0, \tag{1}$$

$$\Psi^t_m = \Phi^t S^1_m, \quad m = -1, 0, 1, \tag{2}$$

where S^0 and S^1_m are the singlet and triplet spin functions, respectively. The corresponding spatial parts are given by the expressions

$$\Phi^s_1 = \varphi^1_1 \varphi^2_{25} + \varphi^1_{25} \varphi^2_1, \tag{3}$$

$$\Phi^t_1 = \varphi^1_1 \varphi^2_{25} - \varphi^1_{25} \varphi^2_1, \tag{4}$$

where the superscript and subscript correspond to the electron coordinate number and the prong of the star of the electron wavevector **k**, respectively. Subscript 1 corresponds to an arbitrarily chosen vector in the basis Brillouin zone and subscript 25 corresponds to the action

of the space inversion (h_{25} in Kovalev's notation [12]) on this vector.

Owing to the translation symmetry, the single-electron function of the crystal is characterized by the star $\{\mathbf{k}\}$ of the vector $\mathbf{k}$. A correct, translationally invariant, two-electron wave function is evidently antisymmetric under permutations and is expressed as a linear combination of functions belonging to all prongs of the star. The structure of this function depends on the choice of the vector $\mathbf{k}_1$ and the symmetry group of this vector. We begin with the general point of the Brillouin zone, where the single-electron wave function is determined by the wavevector star $\{\mathbf{k}\}$ whose dimension is equal to the number of the point-group elements.

To construct the pair wave function, we use the projection operator method [13]. Since the space inversion has already been used in the two-electron functions (3) and (4), only pure rotations are used in the projection operators. The singlet and triplet functions are obviously projected onto only even and odd irreducible representations, respectively.

Acting on wave functions (3) and (4) by the element h_2, which is the 180° rotation about the X axis, we obtain the two other basis functions

$$\Phi_2^s = \varphi_2^1 \varphi_{26}^2 + \varphi_{26}^1 \varphi_2^2, \tag{5}$$

$$\Phi_2^t = \varphi_2^1 \varphi_{26}^2 - \varphi_{26}^1 \varphi_2^2. \tag{6}$$

Two approximations—localized spins and spin space groups—are possible for the spin part of the wave function. In the localized-spin approximation, projection operators act only on the spatial parts of the singlet and triplet functions in Eqs. (1) and (2) and the spin part is common for all prongs of the star. In the spin space group approximation [11], the projection operators also act on the spin parts of the wave functions, which are associated with the prongs of the wavevector star.

In order to construct a complete basis set for the D_{2h} group, it is necessary to determine the functions $\Phi_3^{s(t)}$ and $\Phi_4^{s(t)}$ that are obtained by the action of the operators h_3 and h_4 of the 180° rotation about the Y and Z axes, respectively, on $\Phi_1^{s(t)}$. For the D_{4h} group, it is necessary to determine the basis functions corresponding to the elements h_{13} and h_{16} (180° rotation about the $(-1, 1, 0)$ and $(1, 1, 0)$ axes, respectively) and h_{14} and h_{15} (anticlockwise rotations about the Z axis by 90° and 270°, respectively).

Applying the standard projection-operator method [13], we obtain (Table 1) the total two-electron functions with zero total momentum for the D_{2h} group and (Table 2) results for the one-dimensional irreducible representations of the D_{4h} group. The projection operator method applied in this work is equivalent to the induced-representation method [7–9, 11]. Applying the

Table 1. Pair wave functions and planes in which they vanish for the D_{2h} group (the notation of symmetry elements is taken from [12])

Irreducible representation	Pair function	Zero planes
	Singlet pairs	
A_g	$\Phi_1^s + \Phi_2^s + \Phi_3^s + \Phi_4^s$	No
B_{1g}	$\Phi_1^s - \Phi_2^s - \Phi_3^s + \Phi_4^s$	σ_x, σ_y
B_{2g}	$\Phi_1^s - \Phi_2^s + \Phi_3^s - \Phi_4^s$	σ_z, σ_x
B_{3g}	$\Phi_1^s + \Phi_2^s - \Phi_3^s - \Phi_4^s$	σ_z, σ_y
	Triplet pairs	
A_u	$\Phi_1^t + \Phi_2^t + \Phi_3^t + \Phi_4^t$	$\sigma_x, \sigma_y, \sigma_z$
B_{1u}	$\Phi_1^t - \Phi_2^t - \Phi_3^t + \Phi_4^t$	σ_z
B_{2u}	$\Phi_1^t - \Phi_2^t + \Phi_3^t - \Phi_4^t$	σ_y
B_{3u}	$\Phi_1^t + \Phi_2^t - \Phi_3^t - \Phi_4^t$	σ_x

induced representation method for the general point of the Brillouin zone, one can show that the number of appearance of each irreducible representation is equal to its dimension [9]. This conclusion is consistent with the results of [5, 6]. Since the two-dimensional irreducible representations of the D_{4h} group appear twice, their qualification requires additional quantum numbers.

Beginning with the projection of the basis function Φ_1^s on the first row of the irreducible representation E_g, we arrive at the basis denoted as E_g^α. Similarly, beginning with the projection of the function Φ_1^s on the second row, we obtain the basis denoted as E_g^β.

As an initial vector $\mathbf{k}_1$, any wavevector in the basis Brillouin zone can be taken [11]. At the general point of the Brillouin zone, all even and odd irreducible representations are possible for singlet and triplet pairs, respectively. However, in the symmetry planes in the Brillouin zone, some linear combinations may vanish. Moving to the symmetry plane σ_h in the Brillouin zone, the vector $\mathbf{k}_i$ approaches its mirror image $\sigma_h \mathbf{k}_i$ and the basis functions Φ_i approach their mirror images $\sigma_h \Phi_i$. Two cases are possible in the symmetry plane σ_h. If the basis wave functions Φ_i and $\sigma_h \Phi_i$ enter a linear combination with opposite signs, such a linear combination vanishes in the symmetry plane. The intersection of such a plane with the Fermi surface gives the line of zeros of the pair wave function. If the basis wave functions Φ_i and $\sigma_h \Phi_i$ enter a linear combination with the same sign, there are no symmetry causes for the vanish-

Table 2. Pair wave functions and planes in which they vanish for the D_{4h} group (the notation of symmetry elements is taken from [12])

Irreducible representation	Pair function	Zero planes
	Singlet pairs	
A_{1g}	$\Phi_1^s + \Phi_2^s + \Phi_3^s + \Phi_4^s + \Phi_{13}^s + \Phi_{14}^s + \Phi_{15}^s + \Phi_{16}^s$	No
A_{2g}	$\Phi_1^s - \Phi_2^s - \Phi_3^s + \Phi_4^s - \Phi_{13}^s + \Phi_{14}^s + \Phi_{15}^s - \Phi_{16}^s$	$\sigma_x, \sigma_y, \sigma_{xy}, \sigma_{x-y}$
B_{1g}	$\Phi_1^s + \Phi_2^s + \Phi_3^s + \Phi_4^s - \Phi_{13}^s - \Phi_{14}^s - \Phi_{15}^s - \Phi_{16}^s$	$\sigma_{xy}, \sigma_{x-y}$
B_{2g}	$\Phi_1^s - \Phi_2^s - \Phi_3^s + \Phi_4^s + \Phi_{13}^s - \Phi_{14}^s - \Phi_{15}^s + \Phi_{16}^s$	σ_x, σ_y
$E_g^\alpha(1)$	$\Phi_1^s + \Phi_2^s - \Phi_3^s - \Phi_4^s$	σ_y, σ_z
$E_g^\alpha(2)$	$\Phi_{13}^s - \Phi_{14}^s + \Phi_{15}^s - \Phi_{16}^s$	σ_x, σ_z
$E_g^\beta(1)$	$\Phi_{13}^s + \Phi_{14}^s - \Phi_{15}^s - \Phi_{16}^s$	σ_y, σ_z
$E_g^\beta(2)$	$\Phi_1^s - \Phi_2^s + \Phi_3^s - \Phi_4^s$	σ_x, σ_z
	Triplet pairs	
A_{1u}	$\Phi_1^t + \Phi_2^t + \Phi_3^t + \Phi_4^t + \Phi_{13}^t + \Phi_{14}^t + \Phi_{15}^t + \Phi_{16}^t$	$\sigma_x, \sigma_y, \sigma_z, \sigma_{xy}, \sigma_{x-y}$
A_{2u}	$\Phi_1^t - \Phi_2^t - \Phi_3^t + \Phi_4^t - \Phi_{13}^t + \Phi_{14}^t + \Phi_{15}^t - \Phi_{16}^t$	σ_z
B_{1u}	$\Phi_1^t + \Phi_2^t + \Phi_3^t + \Phi_4^t - \Phi_{13}^t - \Phi_{14}^t - \Phi_{15}^t - \Phi_{16}^t$	$\sigma_x, \sigma_y, \sigma_z$
B_{2u}	$\Phi_1^t - \Phi_2^t - \Phi_3^t + \Phi_4^t + \Phi_{13}^t - \Phi_{14}^t - \Phi_{15}^t + \Phi_{16}^t$	$\sigma_z, \sigma_{xy}, \sigma_{x-y}$
$E_u^\alpha(1)$	$\Phi_1^t + \Phi_2^t - \Phi_3^t - \Phi_4^t$	σ_x
$E_u^\alpha(2)$	$\Phi_{13}^t - \Phi_{14}^t + \Phi_{15}^t - \Phi_{16}^t$	σ_y
$E_u^\beta(1)$	$\Phi_{13}^t + \Phi_{14}^t - \Phi_{15}^t - \Phi_{16}^t$	σ_x
$E_u^\beta(2)$	$\Phi_1^t - \Phi_2^t + \Phi_3^t - \Phi_4^t$	σ_y

ing of the pair wave function. Since the mirror reflection in the plane is equal to the product of the 180° rotation about the axis perpendicular to this plane by inversion and inversion has already been used to construct basis functions (3) and (4), to determine the nodal structure of the functions, it is sufficient to analyze their behavior only under rotations. The function of a singlet (triplet) pair vanishes in a plane if the 180° rotation about the axis perpendicular to this plane changes (does not change) the sign of this function. Tables 1 and 2 present the results of such an analysis of the pair wave functions. The results for one-dimensional representations are unambiguous. Since two-dimensional irreducible representations appear twice in the D_{4h} group, the symmetry-analysis results for them are ambiguous. This conclusion coincides with the results obtained in [5], where two and three types of the basis functions were obtained for two- and three-dimensional irreducible representations, respectively. The basis functions of the irreducible representation E_g^α vanish in the (010) and (001) planes. The basis functions of the irreducible representation E_g^β vanish in the (100) and (001) planes. At the same time, the linear combinations $E_g^\alpha + E_g^\beta$ and $E_g^\alpha - E_g^\beta$ vanish in the vertical planes (110) and (–110), respectively. In addition, both linear combinations vanish in the horizontal symmetry plane (001). Thus, for the irreducible representation E_g, only zeros of the pair wave function in the horizontal plane unambiguously follow from symmetry. The results obtained for weak spin–orbit interaction remain valid for singlet pairs in the case of strong spin–orbit interaction. To analyze the structure of triplet electron pairs in the case of strong spin–orbit interaction, the projection-operator method should be applied directly to functions (1) and (2) and the action of rotations on the pair spin should be taken into account. In the case of axial symmetry, the components S_{+1}^1 and S_{-1}^1 of the projection of the total spin of a triplet pair (ferromagnetic case [9]) are transformed independently of S_0^1 (antiferromagnetic case [9]) and the vanishing of the pair functions occurs in different planes. For this reason, there are usually no planes in which the functions of all triplet pairs vanish, this corresponding to the Blount theorem [6]. However, either the ferromagnetic or antiferromagnetic case is usually realized in the superconducting state; therefore, there are planes in which the triplet order parameter in the presence of strong spin–orbit interaction vanishes due to symmetry requirements [7–9]. The experimental zero planes and directions UPt$_3$ [1] completely coincide with the group-theoretical zeros for the irreducible representation E_{2u} [9]. This coincidence provides the conclusion that the SOP in UPt$_3$ has the E_{2u} symmetry [9]. However, as will be seen below, such a simple relation does not exist for HTSC materials.

3. Analyzing a wide variety of experimental data, most authors (see review [2]) conclude that the SOP in HTSC materials belongs to the irreducible representation A_g of the group D_{2h}. In this case, two possibilities—s pairing, i.e., without lines of zeros, and $d_{x^2-y^2}$ pairing with a line of zeros in the rectangle diagonal—are analyzed. Interplay between two pairing types has been found in some cases [2]. Photoelectron spectra with angular resolution [2] and conduction spectra [3] exhibit the anisotropy of the pseudogap and its vanishing in the rectangle diagonal. According to data presented in Table 1, (i) all irreducible representations except A_g in the singlet case corresponding to HTSC have zero lines in coordinate planes that are not observed experimentally and (ii) there is no irreducible representation that has zeros in the diagonal plane. From the first conclusion, it follows that A_g-type pairing is the most probable. The second conclusion is trivial, because the reflection in the diagonal plane is not an element of the D_{2h} group. Thus, the observed nodal structure of pairs is more complicated than the structure following from crystal symmetry. To describe the symmetry of such a wave function, we take two vectors $\mathbf{k}_1^\alpha$ and $\mathbf{k}_1^\beta$ that are symmetric with respect to the rectangle diagonal. The stars of these vectors (without inversion) in the projection onto the XY plane and the form of the photoelectron spectrum with angular resolution [2] are shown in Fig. 1. For two vectors $\mathbf{k}_1^\alpha$ and $\mathbf{k}_1^\beta$, the singlet wave functions corresponding to the irreducible representation A_g are obtained from Table 1 by introducing additional indices α and β. We emphasize that two-electron states corresponding to different single-electron vectors $\mathbf{k}$ belong to the same irreducible representation A_g and, in contrast to single-electron states belonging to different vectors $\mathbf{k}$, can interact with each other. We write the two resulting states in the form

$$\Phi_s^s = c_1(\Phi_{1,\alpha}^s + \Phi_{2,\alpha}^s + \Phi_{3,\alpha}^s + \Phi_{4,\alpha}^s)$$
$$+ c_2(\Phi_{1,\beta}^s + \Phi_{2,\beta}^s + \Phi_{3,\beta}^s + \Phi_{4,\beta}^s), \quad (7)$$

$$\Phi_{x^2-y^2}^s = c_2(\Phi_{1,\alpha}^s + \Phi_{2,\alpha}^s + \Phi_{3,\alpha}^s + \Phi_{4,\alpha}^s)$$
$$- c_1(\Phi_{1,\beta}^s + \Phi_{2,\beta}^s + \Phi_{3,\beta}^s + \Phi_{4,\beta}^s). \quad (8)$$

The first function does not vanish in the diagonal plane and is denoted by the subscript s. The second function approaches zero in the diagonal plane and is denoted by the subscript $x^2 - y^2$. It is worth noting that orthorhombicity, i.e., $\frac{b-a}{b+a}$, in YBCuO materials is as small as 2% [2] and can be treated as perturbation. For zero orthorhombicity, the D_{2h} symmetry is transformed to the D_{4h} symmetry and the functions with subscripts
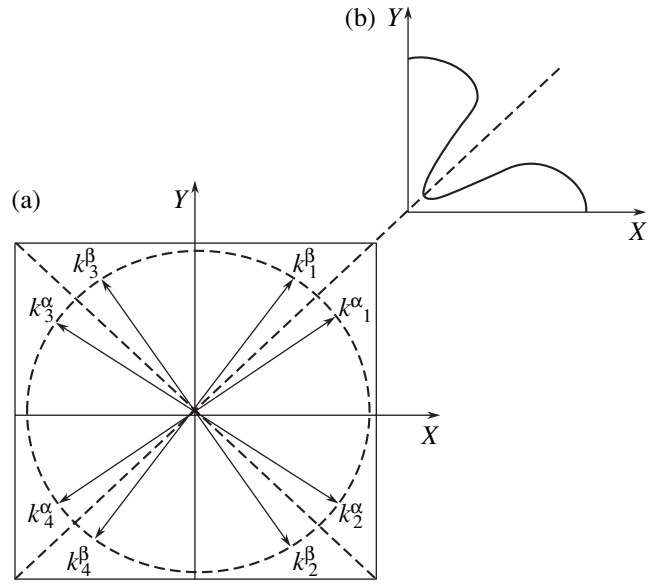

Fig. 1. (a) Single-electron wave vectors corresponding to functions (7) and (8) and (b) the angular distribution of photoelectron spectra for HTSC materials [2].

α and β are transformed to $\Phi_1^s + \Phi_2^s + \Phi_3^s + \Phi_4^s$ and $\Phi_{13}^s + \Phi_{14}^s + \Phi_{15}^s + \Phi_{16}^s$, respectively. In the D_{4h} symmetry group, functions (7) and (8) belong to the irreducible representations A_{1g} and B_{1g}, respectively, and the latter function vanishes in a diagonal, which corresponds to experiment [2]. Thus, as follows from the group-theoretical analysis, experimental data, and the small orthorhombicity of the crystal, the two-electron wave function in HTSC materials corresponds to the irreducible representation B_{1g} of the D_{4h} group rather than to the irreducible representation A_{1g} of the D_{2h} group.

Thus, using the projection-operator method, we have constructed the wave functions of two-electron states (Cooper pairs) for HTSC materials. These wave functions include all prongs of the wavevector stars and are transformed according to the irreducible representations of a point group. It has been shown that experimental data on the pseudogap symmetry are not described by the D_{2h} crystal symmetry and, according to the above group-theoretical analysis and available experimental data, correspond to the irreducible representation B_{1g} of the D_{4h} group.

Division of Chemistry and Materials Science, Russian Academy of Sciences.

REFERENCES

1. C. Broholm, G. Aeppli, R. N. Kleiman, *et al.*, Phys. Rev. Lett. **65**, 2062 (1990).
2. C. C. Tsuei and J. R. Kirtley, Rev. Mod. Phys. **72**, 969 (2000).
3. G. Koren, L. Shkedy, and E. Polturak, Physica A **403**, 45 (2004).
4. P. W. Anderson, Phys. Rev. B **30**, 4000 (1984).
5. G. E. Volovik and L. P. Gor'kov, Zh. Éksp. Teor. Fiz. **88** (4), 1412 (1985) [Sov. Phys. JETP **61**, 843 (1985)].
6. E. I. Blount, Phys. Rev. B **32**, 2935 (1985).
7. V. G. Yarzhemskiĭ and É. N. Murav'ev, Dokl. Akad. Nauk SSSR **317** (5), 1124 (1991) [Sov. Phys. Dokl. **36**, 323 (1991)].
8. V. G. Yarzhemsky, Z. Phys. B: Condens. Matter **99**, 19 (1995).
9. V. G. Yarzhemsky, Int. J. Quantum Chem. **80**, 133 (2000).
10. S. Yip and A. Garg, Phys. Rev. B **48**, 3304 (1993).
11. C. J. Bradley and A. P. Cracknell, *The Mathematical Theory of Symmetry in Solids. Representation Theory of Point Groups and Space Groups* (Clarendon, Oxford, 1972).
12. O. V. Kovalev, *Irreducible and Induced Representations and Corepresentations of Fedorov's Groups* (Nauka, Moscow, 1988) [in Russian].
13. M. Hamermesh, *Group Theory and Its Applications to Physical Problems* (Addison-Wesley, Reading, Mass., 1962; Mir, Moscow, 1966).

Translated by R. Tyapaev

====== **PHYSICS** ======

Time Dilation as a Cause of Elasticity of the Effective Riemannian Space

Academician S. S. Gershteĭn, Academician A. A. Logunov, and M. A. Mestvirishvili

The elasticity of the Riemannian space was previously discussed by Sakharov [1]. He related the cause of space elasticity to an effect of the space curvature on the quantum fluctuations of physical fields. In his opinion, it is these effects that result in the appearance of space elasticity. At the same time, these effects could form conditions that promote a transition from contraction to expansion in the vicinity of a singularity. However, this concept has not been further developed.

In [1], the Riemannian space was considered within the framework of general relativity theory (GRT) as a basis space, and its metric tensor $g_{\mu\nu}$ determined both the geometry of space–time and gravitation. Sakharov saw the essence of gravitation in the existence of the metric elasticity that counteracted space–time curving. In the present study, we treat the gravitational field as a physical field that is developed in the Minkowski space. The source of this field is the energy–momentum tensor of all physical fields, including the gravitational field. In this approach, the Riemannian space arises not as the initial one but as an effective space. It is this point of view that in reality leads to the appearance in gravitational field theory of the elasticity of the effective Riemannian space, which resists an unbounded increase in its curvature.

In this paper, we show that the cause of the appearance of space elasticity is the process of time dilation. It was established in [2] that in gravitational field theory the time dilation of physical processes, which is caused by the gravitational field, generates effective repulsive forces that confine the gravitational potential. This is the mechanism that realizes a termination of the collapse, eliminates the cosmological singularity, and ensures the cyclic development of the Universe. Thus, the passage from contraction to expansion and the elimination of the singularity do not require quantum vacuum fluctuations and occur due to the intrinsic gravitational-field property to limit its potential. At the same time, this property of the gravitational field results in

Russian Research Centre Institute for High Energy Physics, ul. Pobedy 1, Protvino, Moscow oblast, 142281 Russia
e-mail: gershtein@mx.ihep.ru; Anatoly.Logunov@ihep.ru

the elasticity of the effective Riemannian space, which also manifests itself in the fact that the curvature of this space is bounded as well. The elasticity counteracts space–time curvature.

We now consider, as an example, the gravitational field in a contracting (synchronous) coordinate system. The passage to this system from the inertial one is based on the transformations

$$dt = \frac{1}{U}[d\tau - dR(1 - U)],$$

$$dW = \sqrt{\frac{1 - U}{UV}}(dR - d\tau).$$

In the synchronous coordinate system, intervals of the Riemannian space and of the pseudo-Euclidean space are of the form

$$ds^2 = d\tau^2 - [1 - U(Z)]dR^2 - W^2(Z)(d\Theta^2 + \sin^2\Theta \, d\phi^2), \qquad (1)$$

$$d\sigma^2 = d\tau^2 \frac{1 - \dot{r}^2 U^2}{U^2} + 2dR \, d\tau \, \frac{\dot{r}^2 U^2 - (1 - U)}{U^2}$$
$$- dR^2 \frac{\dot{r}^2 U^2 - (1 - U)^2}{U^2} - r^2(d\Theta^2 + \sin^2\Theta \, d\phi^2); \qquad (2)$$

where $Z = R - \tau$ and $\dot{r} = \dfrac{dr}{dZ}$. The equations of relativistic gravitational theory (RGT) taken outside the substance for the problem described by Eqs. (1) and (2), namely,

$$R_{\mu\nu} = 8\pi G\left(T_{\mu\nu} - \frac{1}{2}g_{\mu\nu}T\right) + \frac{m^2}{2}(g_{\mu\nu} - \gamma_{\mu\nu}), \qquad (3)$$

$$D_\nu \tilde{g}^{\mu\nu} = 0 \qquad (4)$$

(here, $m = \dfrac{m_g c}{\hbar}$, where m_g is the graviton mass) lead to

equations of the form

$$R_{01} = \frac{2\ddot{W}}{W} + \frac{1}{(1-U)W}\dot{U}\dot{W} = \frac{m^2}{2}\left(\frac{1-U}{U^2} - \dot{r}^2\right), \quad (5)$$

$$R_{00} + R_{01} = \frac{1}{1-U}\left[\frac{1}{2}\ddot{U} + \frac{\dot{U}^2}{4(1-U)} + \frac{1}{W}\dot{U}\dot{W}\right]$$
$$= -\frac{m^2}{2}\frac{1-U}{U}. \quad (6)$$

Here, $\dot{W} = \dfrac{dW}{dZ}$ and $\dot{U} = \dfrac{dU}{dZ}$. In the variation region of the variable Z in which the graviton mass may be ignored due to its smallness, we find from Eqs. (5) and (6)

$$W = r_g^{1/3}\left(\frac{3}{2}Z\right)^{2/3}, \quad 1-U = \left(\frac{2}{3}r_g\right)^{2/3}Z^{-2/3}; \quad (7)$$

where r_g is the Schwarzschild radius arising as a consequence of the correspondence principle. From expression (7), it follows that the function U decreases with decreasing Z, the derivative $\dot{U}$ being positive. Such a decrease of the function U also occurs in the region of lower values of Z, since the value of $\dot{U}$ in Eq. (6) remains positive.

Insofar as (by virtue of the smallness of m) we can ignore the quantity

$$\frac{m^2}{2}(W^2 - r^2)$$

compared to unity, one can find from Eq. (3) that outside the substance

$$R_{22} = -\frac{UW}{1-U}\ddot{W} - \frac{U}{1-U}\dot{W}^2$$
$$- \frac{W(2-U)}{2(1-U)^2}\dot{U}\dot{W} + 1 = 0. \quad (8)$$

In the region of small values of U, $0 < U \ll 1$, Eq. (8) is slightly simplified and takes the form

$$UW\ddot{W} + U\dot{W}^2 + W\dot{U}\dot{W} - 1 = 0. \quad (9)$$

This equation has the solution

$$\dot{W} = \frac{Z}{UW}, \quad (10)$$

related to the stop point

$$\dot{W} = 0. \quad (11)$$

According to Eqs. (5) and (6), the second derivative $\ddot{W}$ at small values of U is positive, which testifies to the presence of a repulsive force. This is the point from which the expansion process begins to occur. The expansion ceases in the region of Z for which equalities (7) hold. In this region, the values of $\ddot{W}$ are negative:

$$\ddot{W} = -\frac{1}{2}r_g^{1/3}\left(\frac{3}{2}Z\right)^{-4/3}, \quad (12)$$

hence, the attraction takes place. Thus, if the stop point turns out to be outside the substance, then expansion follows upon the contraction. Further, the stoppage and the contraction occur again, etc. However, as we will show below, the actual gravitational field excludes this regime of motion.

As is shown in [3, 4], in the RGT, the following relationships are valid at a stop point:

$$U = \left(\frac{GMm_g}{\hbar c}\right)^2, \quad W = r_g = \frac{2GM}{c^2}. \quad (13)$$

In addition, for small values of U, the curvature invariant

$$R_{\mu\nu\alpha\beta}R^{\mu\nu\alpha\beta} = \frac{12}{W^4} - \frac{10m^2}{UW^2} + \frac{7}{2}\frac{m^4}{U^2} \quad (14)$$

as we see, is bounded. At the stop point, this invariant is equal to

$$R_{\mu\nu\alpha\beta}R^{\mu\nu\alpha\beta} = \frac{28}{r_g^4}. \quad (15)$$

In the framework of the GRT, this invariant is [5]

$$R_{\mu\nu\alpha\beta}R^{\mu\nu\alpha\beta} = \frac{48M^2}{W^6} \quad (16)$$

and may be arbitrarily large as W approaches zero. Comparing expressions (15) and (16), we can see that the repulsive forces arising in the field theory due to the time dilation terminate [in accordance with (13) and (15)] the rise of the effective Riemannian space, which is manifested in the form of space elasticity. In other words, the space resists an increase of its curvature. However, this elasticity is not associated with quantum fluctuations. It is determined by the fundamental properties of the gravitational field, namely, the possibility of constraining its potential. Insofar as the gravitational field (1) is produced by the substance, it follows from the given example that, in order to obtain the physical result, it is necessary to match the solutions inside and outside of the substance. To do this, it is necessary that the gravitational-field potential on the

body's surface be bounded in its absolute value by the inequality

$$\frac{|\phi|}{c^2} < 1. \qquad (17)$$

This is the solution that corresponds to the actual gravitational field and that leads to a scenario in which the stop point cannot be in vacuum. For this reason, it is impossible to reach even the value (15) of the curvature invariant in the actual gravitational field. Therefore, in the case when the value of expression (15) exceeds the magnitude of the curvature invariant, the world lines of particles that are at rest with respect to the contracting coordinate system will collide with the substance of the field source. In this case, for each observer, such collisions will occur for a finite time. These arguments exclude the regime of motion that was mentioned above. At the same time, they also exclude the appearance of black holes.

REFERENCES

1. A. D. Sakharov, Dokl. Akad. Nauk SSSR **177**, 70 (1967) [Sov. Phys. Dokl. **12**, 1040 (1967)].

2. S. S. Gershteĭn, A. A. Logunov, and M. A. Mestvirishvili, Dokl. Akad. Nauk **402**, 34 (2005) [Dokl. Phys. **50**, 227 (2005)].

3. A. A. Vlasov and A. A. Logunov, Teor. Mat. Fiz. **78** (3), 323 (1989).

4. A. A. Logunov, *The Theory of Gravity* (Nauka, Moscow, 2001) [in Russian].

5. A. S. Eddington, *Mathematical Theory of Relativity*, 2nd ed. (Cambridge Univ. Press, Cambridge, 1924; Gostekhizdat, Moscow, 1934).

Translated by G. Merzon

===================== **PHYSICS** =====================

Self-Organized Criticality in the Case
of Acoustic Cavitation of Liquids

Corresponding Member of the RAS V. P. Koverda, V. N. Skokov,
A. V. Reshetnikov, and A. V. Vinogradov

The propagation of high-intensity sound waves in liquids causes acoustic cavitation. The complicated nature of the interaction of arising vapor-gas bubbles both between themselves and with the acoustic field can result in the formation of various spatial structures. Structures formed by vapor-gas bubbles, which recall fractal clusters, were discovered experimentally when standing waves arose in the sound field [1]. Such structures were called acoustic Lichtenberg figures [1, 2]. In order to describe this phenomenon, a theoretical model was developed in [2]. In accordance with this model, an instability leading to self-organization arises in a system of cavitation bubbles placed into the acoustic field. When the size of the region occupied by the ultrasound-radiation field is comparable with the radiation wavelength, quasi-two-dimensional clusters can be formed near the radiator surface [3]. The complicated character of the interaction of cavitation pockets between themselves and with sound waves in an experimental cell can result in the formation of bistability and transitions between steady states [4, 5].

The formation of cavitation clouds can be considered as a nonequilibrium phase transition in the complicated system of interacting cavitation pockets and sound waves. In the acoustic field, a steady random process is formed with nonequilibrium phase transitions whose spectrum of power can be of the $\frac{1}{f}$ shape (*f* is frequency). Random processes displaying a spectrum of power that is inversely proportional to the frequency are rather interesting because they manifest the scale-invariant properties of the fluctuation distribution. These scaling properties may be associated with either the critical behavior of complicated systems or the self-organization occurring in them [6]. Many attempts have been made to explain a possible mechanism for the generation of scale-invariant fluctuations on the basis of the concept of self-organized criticality [6, 7], which is used to describe complicated systems with developed fluctuations.

Studies of the random processes observed in crisis regimes of boiling liquids have shown that fluctuations exhibiting the $\frac{1}{f}$ spectrum and self-organization of the critical state can arise as a result of the interaction of the subcritical and supercritical nonequilibrium phase transitions in the presence of white noise [8–10]. In this case, the stretched critical behavior of fluctuations is characterized by a self-similar distribution of the probability density, which is independent of time [10]. Alongside the crisis behavior of boiling liquids, the critical properties of fluctuations are observed in cavitation processes. In [11], results are presented of experimental studies of fluctuations observed in cavitation processes that occur in boiling water placed into the ultrasound field. These experiments were conducted using the laser-photometry method and the resistive method. A regime was found that exhibited the $\frac{1}{f}$ spectrum of power and the bimodal function of the local fluctuation distribution. As the ultrasound-field intensity was increased, some of the cavitation centers began to interact with each other, which was accompanied by the formation of various spatial structures.

In this paper, we describe experimental data that was obtained as a result of observations of spatial structures associated with the acoustic cavitation of liquids. For comparison, the results of numerical calculations performed in the framework of the theoretical model of interacting nonequilibrium phase transitions in a two-dimensional spatially distributed system are analyzed.

We have carried out the experiments using a standard magnetostriction radiator of ultrasound oscillations at a frequency of 22 kHz. The radiator was placed into an optical cell filled with water or glycerin. Having elevated the radiator power, we produced the cavitation in the cell. Varying the radiation intensity, we managed to observe resonance phenomena occurring in the cell,

Institute of Thermal Physics, Ural Division,
Russian Academy of Sciences, ul. Amundsena 106,
Yekaterinburg, 620016 Russia
e-mail: koverda@itp.uran.ru; vnskokov@itp.uran.ru;
reshav@itp.uran.ru

which led to variations of the pattern produced by interacting cavitation bubbles.

In the case of low radiation intensity, separate cavitation centers arose on the surface of a liquid (Fig. 1a). As a result of mutual attraction, bubbles lined up, forming chains. The number of cavitation centers increased with the radiator power. As a result of the cooperative interaction of bubbles near the radiator surface, aggregates redolent of fractal clusters were formed. The vapor-gas flux was directed from the peripheral part of the clusters to their central part. Certain clusters were able to escape from the surface and penetrate into the interior of the liquid. In the experiments with glycerin, the aggregates being formed were relatively long-lived and had a more contrasting shape.

With a further increase in the radiator power, the interacting cavitation centers formed a critically fluctuating surface (Fig. 1c). In this case, the large number of interacting centers allows us to present a simplified description of the fluctuation dynamics. To this end, we can use a variant of the concept of self-organized criticality to interpret nonequilibrium phase transitions [8–10, 12].

The stochastic equations that describe the fluctuation dynamics related to nonequilibrium phase transitions in a spatially distributed system can be written in the form [12]

$$\frac{\partial \phi}{\partial t} = D\left(\frac{\partial^2 \phi}{\partial x^2} + \frac{\partial^2 \phi}{\partial y^2}\right) - \phi\psi^2 + \psi + \Gamma_1(x, y, t),$$

$$\frac{\partial \psi}{\partial t} = -\psi\phi^2 + \phi + \Gamma_2(x, y, t). \tag{1}$$

Here, ϕ and ψ are the dynamic variables (order parameters), D is the diffusion coefficient, and Γ_1 and Γ_2 are the intensities of the Gaussian δ-correlated noise. When the set of equations is written in the form of (1), Γ_1 and Γ_2 can have different realizations but identical dispersions.

In order to numerically integrate the set of Eqs. (1), we have used the Euler difference scheme with periodic boundary conditions and different initial conditions. The functions $\Gamma_1(x, y, t)$ and $\Gamma_2(x, y, t)$ were approximated by samples of normally distributed random numbers.

The spectra of power for the stochastic variable ϕ within the wide variation range of governing parameters had the $\frac{1}{f}$ shape. Correspondingly, the spectrum of power for the stochastic variable ψ had the $\sim\frac{1}{f^2}$ shape. However, the spectra of power for the reciprocal quantity $\frac{1}{\psi}$ varied in inverse proportion to $\sim\frac{1}{f}$. The distribution function for the variables in the case of roughening the time and space scales becomes scale invariant. This result is analogous to those obtained in the course of

(a)

(b)

(c)
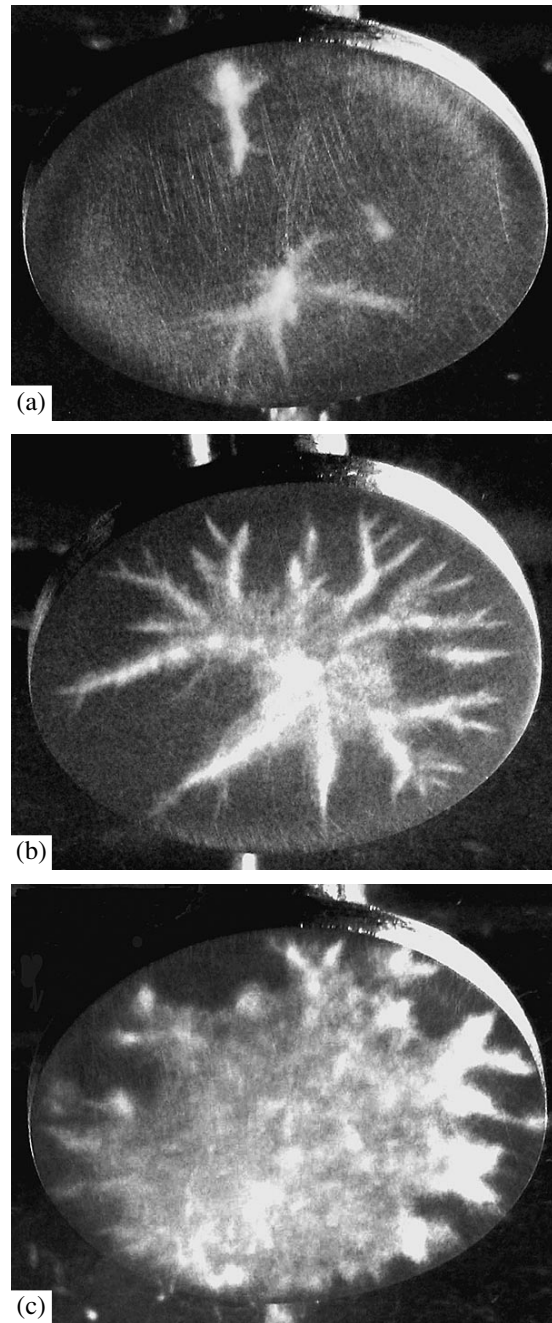
Fig. 1. Photographic pattern of cavitation regions on the radiator surface for different ultrasound-field intensities.

investigating the concentrated system [10] and the spatially distributed one-dimensional system [12]. Features inherent in studies of two-dimensional systems manifest themselves in the possibility of the appearance of spatial structures. Figure 2a illustrates the spatial configuration of the stochastic variable ϕ upon 8192 integration steps Δt ($\Delta t = 0.1$; the number of spatial steps is 1024×1024) for homogeneous initial conditions. The pattern presented in Fig. 2 is roughened over small-scale spatial fluctuations. Dark and light regions
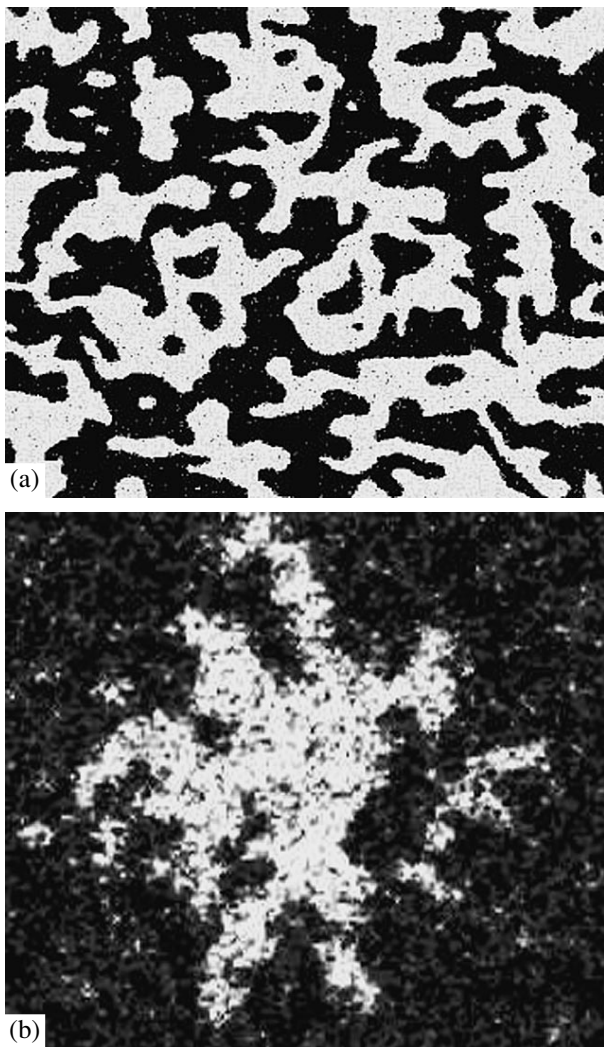
Fig. 2. Spatial distribution of the variable ϕ, which is roughened over small-scale fluctuations. The distribution was obtained by numerical calculation of the set of Eqs. (1): (a) homogeneous random-field intensity and (b) cluster growth in the case of setting a certain spatial inhomogeneity in the random-field intensity.

bubble interactions becomes more important. In this case, the evolution of the system should be described on the basis of hydrodynamics and nonlinear dynamics [1–5].

Thus, the acoustic cavitation of liquids is accompanied by the formation of various spatial structures, a low-frequency divergence in the spectrum of power, and the scale invariant fluctuation-distribution function. The experimental data obtained in this study are qualitatively consistent with the results of the numerical simulation based on the theory of $\frac{1}{f}$ fluctuations for nonequilibrium phase transitions in spatially distributed systems. The results obtained require no fine-tuning of governing parameters and testify to the existence of the regime of self-organized criticality.

REFERENCES

1. W. Lauterborn, E. Schmitz, and A. Judt, Int. J. Bifurcation Chaos **3** (3), 635 (1993).
2. I. Akhatov, U. Parlitz, and W. Lauterborn, Phys. Rev. E **54**, 4990 (1996).
3. A. Mousatov, C. Granger, and B. Dubus, Ultrason. Sonochem. **10**, 191 (2003).
4. A. O. Maksimov and E. V. Sosedko, Pis'ma Zh. Tekh. Fiz. **29** (3), 40 (2003) [Tech. Phys. Lett. **29** (2), 102 (2003)].
5. G. N. Sankin and V. S. Teslenko, Dokl. Akad. Nauk **393**, 362 (2003) [Dokl. Phys. **48**, 665 (2003)].
6. H. J. Jensen, *Self-Organized Criticality* (Cambridge Univ. Press, New York, 1998).
7. P. Bak, C. Tang, and K. Wiesenfeld, Phys. Rev. A **38**, 364 (1988).
8. V. P. Koverda, V. N. Skokov, and V. P. Skripov, Zh. Éksp. Teor. Fiz. **113**, 1748 (1998) [JETP **86**, 953 (1998)].
9. V. N. Skokov, A. V. Koverda, A. V. Reshetnikov, *et al.*, Int. J. Heat Mass Transf. **46**, 1879 (2003).
10. V. P. Koverda and V. N. Skokov, Dokl. Akad. Nauk **393**, 184 (2003) [Dokl. Phys. **48**, 615 (2003)].
11. V. P. Koverda, V. N. Skokov, A. V. Reshetnikov, *et al.*, Pis'ma Zh. Tekh. Fiz. **30** (22), 31 (2004) [Tech. Phys. Lett. **30** (11), 944 (2004)].
12. V. N. Skokov, V. P. Koverda, and A. V. Reshetnikov, Zh. Éksp. Teor. Fiz. **119**, 613 (2001) [JETP **92**, 535 (2001)].

correspond to positive and negative values of the variable ϕ, respectively. As is seen, a self-similar spatial structure corresponding to the critical state is formed in the system.

These structures are obtained as a result of the system evolution. Their shape weakly depends on the initial conditions and on the intensity of the external noise within the wide range of their variations. Cluster growth could be observed (Fig. 2b) upon setting a spatial inhomogeneity in the random-field intensity.

In the case of a high density of cavitation centers, the pattern obtained is not very sensitive to interaction details. Therefore, a simplified description of the system state, which uses the set of Eqs. (1), is possible. At lower densities of cavitation centers, the character of

Translated by G. Merzon

═════════════════════ **PHYSICS** ═════════════════════

Reconstruction of the Equilibrium of a Toroidal Plasma from Data of Optical and Magnetic Diagnostics

Corresponding Member of the RAS D. P. Kostomarov, F. S. Zaitsev, and A. A. Lukianitsa

INTRODUCTION

An important research area in controlled thermonuclear fusion is the development of methods for reconstructing the plasma parameters from experimental data obtained at setups with magnetic confinement. Such methods make it possible to acquire information on plasma characteristics that cannot be directly measured in experiment [1–3].

Reconstruction problems are usually very difficult, because many of them are incorrectly posed. In most cases, the solution of each inverse problem represents a special individual laborious investigation. In such problems, the volume of the input data and the volume of prior information on a desired solution are of key importance: the larger the input information volume, the more accurate the reconstruction results.

The methods previously applied towards solving the problem of the reconstruction of equilibrium are based on magnetic measurements and measurements of various integral characteristics of a plasma. In a proposed new method, in addition to the above-listed data, information on the position of the plasma boundary is used.

Such information can be extracted with a sufficiently high accuracy from plasma video images. For example, video recording is a standard diagnostic procedure for the MAST and JET setups.

The aim of this work is to develop a fast reliable algorithm for reconstructing the plasma boundary from optical data and to work out its application to the development of a new combined method for reconstructing the internal characteristics of the plasma from optical and traditional magnetic measurements. Moreover, the method is analyzed both theoretically and numerically.

FORMULATION OF THE PROBLEM

The problem of the equilibrium of a toroidal plasma column is mathematically formulated as follows. The Grad–Shafranov equilibrium equation [4] obtained from Ampere's law and the force balance in an axisymmetric magnetic field has the form

$$R\frac{\partial}{\partial R}\left(\frac{1}{R}\frac{\partial \psi}{\partial R}\right) + \frac{\partial^2 \psi}{\partial Z^2} = -\mu_0 R j_\eta, \qquad (1)$$

$$j_\eta(R, \psi) = \begin{cases} R\dfrac{\partial p(t, \psi)}{\partial \psi} + \dfrac{1}{2\mu_0 R}\dfrac{\partial F^2(t, \psi)}{\partial \psi} & \text{inside } D_\mathrm{p}(t), \\[2ex] \displaystyle\sum_{i=1}^{L} J_i(t)\delta(R - R_i)\delta(Z - Z_i) & \text{outside } D_\mathrm{p}(t). \end{cases} \qquad (2)$$

Here, (R, η, Z) are cylindrical coordinates such that the Z axis is the symmetry axis; $D_\mathrm{p}(t)$ is the region occupied by the plasma; $\Gamma_\mathrm{p}(t)$ is the boundary of the domain $D_\mathrm{p}(t)$; $j_\eta(t, R, Z)$ is the toroidal current density; $\psi(t, R, Z)$ is the poloidal flux function; $F(t, \psi)$ is the poloidal current function; $p(t, \psi)$ is the kinetic pressure; and the summation with respect to subscript i on the right-hand side of Eq. (1) outside the plasma is performed over all the ring currents of a setup that flow in a solenoid, driving coils of the poloidal field, and chamber walls.

Owing to the axial symmetry, the problem is two-dimensional and is considered in the unbounded space of two variables (R, Z). The chamber wall is simulated by a set of elementary ring currents [3]. The following

Faculty of Computational Mathematics and Cybernetics, Moscow State University, Vorob'evy gory, Moscow, 119992 Russia
e-mail: zaitsev@cs.msu.su

additional conditions are taken into account:

$$\lim_{R \to 0} \psi = \lim_{\substack{R \to \infty \\ Z \to \infty}} \psi = 0, \qquad (3)$$

$$F(t, \psi)|_{\Gamma_p(t)} = \frac{\mu_0}{2\pi} I_{\mathrm{rod}}(t), \qquad (4)$$

$$I_p(t) = \int_{D_p} j_\eta ds. \qquad (5)$$

The known input data are $\psi(t, R, Z)$ values at the points (R, Z), where the magnetic field is measured; the total toroidal current $I_p(t)$ in the plasma; the current $I_{\mathrm{rod}}(t)$ through the central rod creating the toroidal magnetic field; and the current $J_i(t)$, $i = N_{\mathrm{PFC}, 1}, \ldots, N_{\mathrm{PFC}, 2}$, $i = N_{\mathrm{sol}, 1}, \ldots, N_{\mathrm{sol}, 2}$. The plasma boundary $\Gamma_p(t)$ found from optical measurements is also considered as known. It is necessary to determine the functions $j_\eta(t, R, Z)$, $\psi(t, R, Z)$, $F(t, \psi)$, and $p(t, \psi)$ and currents $J_i(t)$, $i = N_{\mathrm{wall}, 1}, \ldots, N_{\mathrm{wall}, 2}$ in the chamber walls.

The problem given by Eqs. (1)–(5) is an inverse problem for the Grad–Shafranov equation. In contrast to the approaches that are usually used, the problem is solved in two steps: the plasma boundary $\Gamma_p(t)$ is first reconstructed from optical data, and the internal plasma parameters are then reconstructed using traditional magnetic measurements.

RECONSTRUCTION OF THE BOUNDARY

The reconstruction of the shape and position of the plasma boundary is based on the processing of images obtained by a fast video camera. The basic physical effect used for the processing is an increased brightness of the plasma boundary.

The difficulty of the problem is determined by several factors: the inner surface of the toroidal chamber usually has mirror properties; synchronous change in the exposition time is complicated due to the fast dynamics of the process; and an image is distorted due to the optical properties of the chamber. Despite these difficulties, a fast reliable algorithm has been developed for calculating the cylindrical coordinates (R, Z) of the boundary of the axisymmetric plasma.

It is proposed that the compensation of the spherical distortions of the chamber and its calibration be performed in a manner similar to that in [5, 6].

It is convenient to formulate the problem in the polar coordinate system (r, ϕ) in the image plane (u, v). A certain point (u_0, v_0) close to the magnetic axis is taken to be the origin of the coordinate system. Let us introduce uniform grids in radius $r_i = i\Delta r$, $i = 0, \ldots, N_r(j)$ and angle $\phi_j = j\Delta\phi$, $j = 0, \ldots, N_\phi$, where Δr and $\Delta\phi$ are the grid steps. The number of points in the radius, $N_r(j) + 1$, depends on the ordinary number j of the

angle, because the photograph is rectangular. Let $r_{i(j)} \equiv r_i(\phi_j)$ be the r_i radius value on the jth ray.

To determine the plasma boundary on the photograph, among the set Ω of all sequences $\{r_i(\phi_j)\}$, $j = 0, 1, \ldots, N_\phi$, of grid points $\{r_i, \phi_j\}$, it is necessary to find a sequence $\{r_i^*(\phi_j)\}$ for which the total luminescence intensity I_{pixel} including constraints is maximal:

$$\Phi(\{r_{i(j)}\}) \equiv \sum_{j=0}^{N_\phi} (I_{\mathrm{pixel}}(r_i(\phi_j), \phi_j) + R_{i(j-1), i(j), i(j+1)}), \qquad (6)$$

where

$$R_{i(j-1), i(j), i(j+1)} \equiv \alpha_1 R_{1, i(j)}$$
$$- \alpha_2 R_{2, i(j-1), i(j)} - \alpha_3 R_{3, i(j-1), i(j), i(j+1)}$$
$$+ \alpha_4 R_{4, i(j-1), i(j), i(j+1)} + \alpha_5 R_{5, i(j-1), i(j), i(j+1)}.$$

Here, R_k are the constraints that enable one to distinguish the most "reasonable" solution of the problem of the plasma boundary: R_1 is the maximum-radius condition, R_2 is the condition of the minimum distance between the neighboring points of the boundary, R_3 is the smoothness condition, R_4 is the derivative-smoothness condition, and R_5 is the convexity condition. In particular, the constraint R_5 has the form

$$R_{5, i(j-1), i(j), i(j+1)} = (r_{i(j)}(r_{i(j-1)} + r_{i(j+1)}) - 2r_{i(j-1)}r_{i(j+1)}\cos(\Delta\phi)).$$

The weight coefficients $\alpha_1, \ldots, \alpha_5$ determine the contributions of the respective constraints into the functional $\Phi_{i(j)}$ and are chosen by fitting the plasma boundary reconstructed in test calculations to the original boundary. The values once found are suitable for a sufficiently wide class of plasma images comparable in scale.

The problem of maximizing functional (6) is solved by the dynamic programming method. If the number of grid points is not too small, the method always provides a certain solution. As a result, we obtain the parameterization $\{r_i^*(\phi_j)\}$ of the boundary image and use it to reconstruct its cylindrical coordinates $(R, Z) \in \Gamma_p$:

$$R = \frac{R_c|\tan\alpha|}{\sqrt{1 + \tan^2\alpha}}, \quad Z = \frac{v - v_0}{a_v}\frac{R_c}{1 + \tan^2\alpha}, \qquad (7)$$

where

$$\tan\alpha = \frac{u - u_0}{a_u}.$$

Here, $u = r^*(\phi)\cos\phi + u_0$, $v = r^*(\phi)\sin\phi + v_0$, α is the angle between the normal vector to the image plane and

the straight line passing through both the objective center and a point on the plasma-bounding surface; R_c is the R value at the objective center; and a_u and a_v are the calibration parameters of the video camera.

The prior and posterior estimates of the error of reconstructing the coordinates of Γ_p, which is associated with the discreteness of the photo receiver of the camera and the thickness of the luminescence layer, are no more than 1–2%, which is a very good result.

RECONSTRUCTION OF THE CURRENT DENSITY

The method of elementary ring currents is proposed in [3] for solving the inverse problem given by Eqs. (1)–(5). The use of the boundary Γ_p as input information is a fundamental point in the method. The new algorithm described in the preceding section allows for the accurate calculation of Γ_p from optical data.

In [3], it was proposed to determine the pressure p and poloidal current function F in the form of the partial sums of power series. A new algorithm for solving this problem will be formulated below.

Let us take into account Eq. (2), which means that the function j_η inside the plasma in equilibrium is represented as the sum of two functions

$$A(\rho)R + \frac{B(\rho)}{R} = \varphi(R, Z), \qquad (8)$$

where $\rho = \rho(R, Z) \in [0, 1]$ for $(R, Z) \in D_p$. The functions $\rho(R, Z) = \rho(\psi(R, Z))$ and $\varphi(R, Z)$ are given. In the general case, the problem of determining the functions A and B from the known φ function is evidently incorrectly posed. Nevertheless, the problem has a meaningful solution. The point is that the factors R and $\frac{1}{R}$ in Eq. (8) separate the values of the desired functions in space; i.e., the second and first terms dominate for small and large R values, respectively. Such a separation is particularly strong in spherical tokamaks for which a more accurate reconstruction of p and F should be expected. This assumption is corroborated by calculations.

Let us formulate theorems clarifying the uniqueness, existence, and construction of the solution of problem (8). The proof is omitted in this short publication.

Theorem 1. *Let at least two points* (R_1, Z_1) *and* (R_2, Z_2) *exist on the contour* $\Gamma(R, Z) = \{(R, Z): \rho(R, Z) = const\}$ *such that* $R_1 \neq R_2$. *If the solution* $(A(\rho), B(\rho))$ *of problem* (8) *exists on* $\Gamma(R, Z)$, *it is unique.*

Theorem 2. *Let problem* (8) *be solvable and P be the set of all contours* $\Gamma(R, Z) = \{(R, Z): \rho(R, Z) = const\}$ *on each of which there are at least two points*

(R_1, Z_1) *and* (R_2, Z_2) *such that* $R_1 \neq R_2$. *In this case, the functions*

$$A(\rho) = \frac{\varphi(R_1, Z_1)R_1 - \varphi(R_2, Z_2)R_2}{R_1^2 - R_2^2}, \qquad (9)$$

$$B(\rho) = \frac{R_1 R_2(\varphi(R_2, Z_2)R_1 - \varphi(R_1, Z_1)R_2)}{R_1^2 - R_2^2} \qquad (10)$$

constructed on the set P satisfy Eq. (8) *and are unique.*

Theorem 3. *Let all points* (R_1, Z_1) *of the contour* $\Gamma(R, Z) = \{(R, Z): \rho(R, Z) = const\}$ *in a certain deleted neighborhood of the point* (R, Z) *be such that* $R_1 \neq R$. *For the existence of a solution of problem* (8) *at the point* (R, Z), *it is sufficient that the function* $\varphi(R, Z)$ *can be represented as* $\varphi(R, Z) = \Phi(R, \rho)$, *where* $\Phi(R, \rho)$ *has the partial derivative with respect to R. In this case, the solution of Eq.* (8) *at the point* (R, Z) *can be found by the formulas*

$$A(\rho) = \frac{1}{2}\frac{\partial \Phi(R, \rho)}{\partial R} + \frac{\Phi(R, \rho)}{2R}, \qquad (11)$$

$$B(\rho) = \frac{1}{2}R\Phi(R, \rho) - \frac{R^2}{2}\frac{\partial \Phi(R, \rho)}{\partial R}. \qquad (12)$$

If the function $\Phi(R, \rho)$ *is such that the right-hand sides of Eqs.* (11) *and* (12) *are constant on the contour* $\rho(R, Z) = const$, *the solution of problem* (8) *exists on the entire contour.*

Formulas (9) and (10) enable one to construct a numerical algorithm for calculating the functions $A(\rho)$ and $B(\rho)$. In the ideal case, according to theorem 2, to determine the functions $A(\rho)$ and $B(\rho)$, it would be sufficient to take two points on the contour $\Gamma(R, Z)$. However, the input data of problem (8) include measurement errors and errors of solving the approximate problems of the previous steps. Therefore, for different points of the contour $\Gamma(R, Z)$, the different $A(\rho)$ and $B(\rho)$ values are generally obtained. Regularization is necessary.

As is seen from estimates, the errors ΔA and ΔB of the functions $A(\rho)$ and $B(\rho)$, respectively, approach zero as the errors of the input data approach zero if the coordinates R_1 and R_2 of the points chosen for calculating the functions $A(\rho)$ and $B(\rho)$ are consistent with the errors of the input data; i.e., R_1 is not too close to $R_2 : |R_1 - R_2| \geq R_{min}$.

The following regularizing algorithm is acceptable for calculating the functions $A(\rho)$ and $B(\rho)$. For each ρ

value, we calculate the average over the pairs (R_i, Z_i) and (R_j, Z_j) of the contour $\Gamma(R, Z)$ and set

$$
A(\rho) \approx \sum_{\substack{(R_i, Z_i),\, (R_j, Z_j)\, \in\, \Gamma(R, Z) \\ |R_i - R_j| \geq R_{\min}}} \frac{|R_i - R_j|}{C(\rho)} \tag{13}
$$
$$
\times \frac{\varphi(R_i, Z_i)R_i - \varphi(R_j, Z_j)R_j}{R_i^2 - R_j^2},
$$

$$
B(\rho) \approx \sum_{\substack{(R_i, Z_i),\, (R_j, Z_j)\, \in\, \Gamma(R, Z) \\ |R_i - R_j| \geq R_{\min}}} \frac{|R_i - R_j|}{C(\rho)} \tag{14}
$$
$$
\times \frac{R_i R_j(\varphi(R_j, Z_j)R_i - \varphi(R_i, Z_i)R_j)}{R_i^2 - R_j^2},
$$

$$
C(\rho) \equiv \sum_{\substack{(R_i, Z_i),\, (R_j, Z_j)\, \in\, \Gamma(R, Z) \\ |R_i - R_j| \geq R_{\min}}} |R_i - R_j|.
$$

The weight $|R_i - R_j|$ reduces the contribution to the sum from the terms with close R_i and R_j values that determine the accuracy of the solution.

The method proposed for calculating p and F is much simpler in its realization than that proposed in [3]; however, it has a low accuracy near $\rho = 0$. In contrast, the method proposed in [3] is inaccurate near the plasma boundary, where $\rho \sim 1$. For this reason, it is appropriate to construct the final result of reconstruction using two methods.

On the whole, theoretical analysis and various test calculations using SCoPE code [7] show that the accuracy of reconstructing j_n, ψ, p, and F by the elementary ring-current method using optical data and Eqs. (13) and (14) is comparable with the perturbation of the input data. It is expected that the above algorithm proposed for solving the inverse problem will ensure higher practical accuracy than the previously applied algorithms, because it involves more input information, including data on the plasma boundary position.

CONCLUSIONS

A new method has been proposed for solving the inverse problem given by Eqs. (1)–(5) in the most complex formulation, when all three functions ψ, F, and p are desired. The data of optical and magnetic diagnostics have been jointly used for the first time.

The algorithm for constructing the plasma boundary is realized in the VIP (Video Image Processing) code, which makes it possible to follow its evolution synchronously with the measured plasma characteristics or to process data in the packet regime. The results obtained

by the VIP code can be used as an additional constraint for various algorithms for reconstructing the plasma equilibrium.

The application of the procedure developed for reconstructing the plasma boundary from photographs to other problems is promising. For example, the high speed of the algorithm makes it hopeful that an on-line system will be created in the near future for controlling the shape and position of the plasma with the feedback based on the processing of video images. Several cameras will make it possible to reconstruct the three-dimensional image of the plasma and to acquire quantitative information on the plasma rotation and on the toroidal-angle dependence of its shape for the axisymmetric case.

The algorithm proposed for processing images or its analogs can be used for numerous problems of reconstructing the coordinates of curves from photographs or video films.

REFERENCES

1. Yu. N. Dnestrovskiĭ and D. P. Kostomarov, *Numerical Simulation of Plasmas* (Mir, Moscow, 1982; Springer, New York, 1986).

2. Yu. N. Dnestrovskiĭ and D. P. Kostomarov, in *Ill-Posed Problems of Natural Science*, Ed. by A. N. Tikhonov and A. V. Goncharovskiĭ (Mosk. Gos. Univ., Moscow, 1987) [in Russian].

3. F. S. Zaitsev, A. B. Trefilov, and R. J. Akers, in *Proceedings of 30th European Conference on Controlled Fusion and Plasma Physics, St. Petersburg, Russia, 2003* (St. Petersburg, 2003), Vol. 27A, p. 2; http://epsppd.epfl.ch.

4. V. D. Shafranov, in *Problems of Plasma Theory* (Gosatomizdat, Moscow, 1963), No. 2, pp. 92–131 [in Russian].

5. R. Mohr and B. Trigs, Projective Geometry for Image Analysis, ISPRS96 (1996).

6. Z. Zhang, Techn. Rep. MSR-TR, 22 (1998).

7. F. S. Zaitsev, A. G. Shishkin, and D. P. Kostomarov, Comput. Phys. Commun. **157** (2), 107 (2004).

Translated by R. Tyapaev

$==$ **PHYSICS** $==$

Fracture of Crystalline Iron Subjected to High-Rate Tension. Molecular Dynamics Simulation

G. É. Norman, V. V. Stegaĭlov, and A. V. Yanilkin

Presented by Academician V.E. Fortov May 3, 2005

Received May 25, 2005

There are several descriptive levels for the fracture of the solid phase. Thermodynamic analysis provides the determination of the stability boundary for the solid phase in the negative-pressure region [1]. The propagation of cracks is described by methods of continuous mechanics [2]. When the fracture time is comparable with the duration of the loading action (e.g., in shock wave experiments), high-speed fracture is of a relaxation character and depends strongly on the kinetics of damage accumulation [3]. In view of this circumstance, problems concerning the initial stages of arising damages are of interest. The atomistic simulation methods such as molecular dynamics and the Monte Carlo method that are based on classical models of interatomic interaction allow investigations of microscopic fracture mechanisms (formation of defects, dislocations, discontinuities, propagation of cracks) for nonzero temperatures (see, e.g., [4–9]). At the same time, modern methods for the *ab initio* calculation of the electronic structure make it possible to precisely determine the cold curves and theoretical ultimate strength of substances (see, e.g., [10]).

In this work, a mechanism of the loss of stability and the process of plastic deformation in crystalline iron subjected to high-rate uniaxial tension are studied using the molecular dynamics method.

MODEL AND CALCULATION METHOD

The model under consideration is an atomic lattice whose initial undeformed state has the bcc structure. The three-dimensional periodic boundary conditions are used. The calculations are performed for systems with sizes $15 \times 15 \times 20$, $20 \times 20 \times 20$, $25 \times 25 \times 20$, and $30 \times 30 \times 20$ unit cells, i.e., for the number of atoms

Institute of High Energy Densities,
Joint Institute for High Temperatures,
Russian Academy of Sciences, ul. Izhorskaya 13/19,
Moscow, 125412 Russia
e-mail: henry_n@orc.ru; stegailov@ihed.ras.ru;
ale-yanilkin@yandex.ru

from 9000 to 36000. The trajectories of atoms are calculated by numerically integrating the system of classical equations of motion using the standard second-order difference scheme with a step of 0.76 fs. The interatomic interaction in iron is described by the embedded atom method potential in the parameterization proposed in [11]. This parameterization ensures good quantitative agreement with a rich variety of experimental and *ab initio* data, including the lattice constant of α-Fe, elastic moduli, point-defect energies, the energy of bcc–fcc transition, the density and structure factor of the liquid phase, and melting temperature.

The instantaneous temperature T and stress tensor $\sigma_{\alpha\beta}$ ($\alpha, \beta \in \{x, y, z\}$) averaged over the calculation-cell volume are calculated as
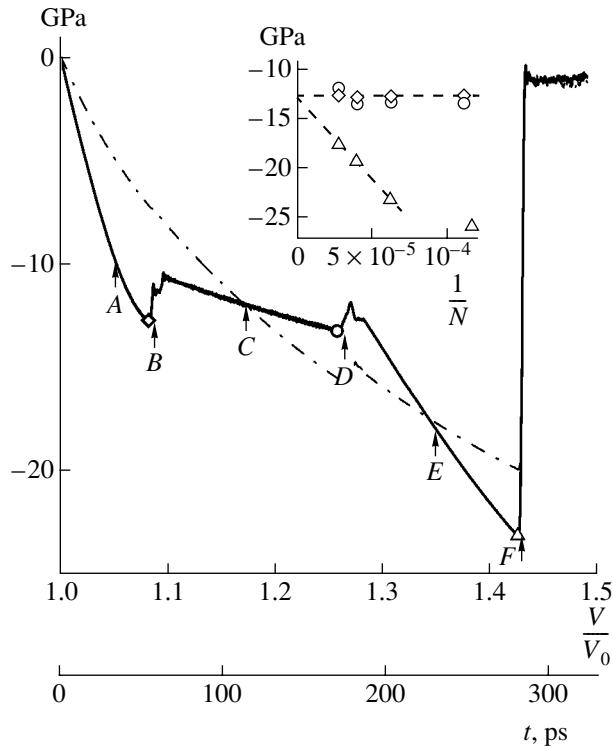
$$T = \frac{2m}{3k_{\mathrm{B}}N} \sum_{i=1}^{N} \frac{\mathbf{v}_i^2}{2},$$

$$\sigma_{\alpha\beta} = \frac{1}{V}\left(\sum_{i=1}^{N} m_i v_{i\alpha} v_{i\beta} - \sum_{i<j} \frac{\partial U}{\partial r_{ij}} \frac{r_{ij\alpha} r_{ij\beta}}{r_{ij}} \right),$$

$$r_{ij} = |\mathbf{r}_i - \mathbf{r}_j|,$$

where k_{B} is the Boltzmann constant; m is the atomic mass; $\mathbf{r}_i$ and $\mathbf{v}_i$ are the coordinate and velocity of the ith atom at the current integration step, respectively; V is the calculation-cell volume; and $U = U(\mathbf{r}_1, \ldots, \mathbf{r}_N)$ is the potential energy of the system. The initial temperature is specified in the thermostabilization scheme: additional Langevin terms—self-consistent white noise and friction force [12], whose total effect is small compared to the interatomic interaction—are introduced into the equations of motion. The uniaxial tension with a constant rate $\dot{V}$ is simulated by scaling of the simula-

Fig. 1. Stresses (solid line) σ_{zz} and (dash–dotted line) σ_{yy} along and across the tension axis, respectively, vs. the relative volume change $\dfrac{V}{V_0}$ and tension time t for $T = 300$ K and $\dfrac{\dot{V}}{V_0} = 1.3 \times 10^9 \text{ s}^{-1}$. The arrows show the states ($A, B, \ldots, F$) for which the atomic structure in the simulation box is shown in Fig. 2. The states corresponding to the local minima of the $\sigma_{zz}(V)$ plot are marked by diamonds for the nucleation of clusters of an alternating body-centered tetragonal lattice, by circles for the end of the martensitic transformation, and by triangles for the nucleation of cavities. The inset shows the stress at the times of the above transitions for various calculation-cell sizes (N is the number of particles). The dashed lines are the extrapolations of the diamonds and triangles in the limit $N \longrightarrow \infty$, $\dfrac{N}{V} =$ const.

tion box and atomic coordinates in the [001] direction at each integration step.[1]

To analyze structural transformations and to visualize changes in the simulation box in the sequential times, the coordination number K and the symmetry parameter of the local environment C [13, 14] are calculated for each atom. It is convenient to take the coordination-sphere radius as $r_K = \dfrac{r_2 + r_3}{2}$, where r_2 and r_3

<hr>

[1] Periodic boundary conditions in the tension direction do not considerably affect the conservation of the total momentum of the system, because the thermal atomic velocities are much higher than the tension rate and atomic diffusion through the boundaries of the simulation box is immaterial under these conditions.

are the distances to the second and third nearest neighbors in the initial undeformed bcc lattice, which corresponds to $K = 14$. The symmetry of the positions of neighboring atoms with respect to the ith atom is quantitatively given by the parameter

$$C_i = \frac{\displaystyle\sum_{m=1}^{K_i/2} D_{im}}{2\displaystyle\sum_{n=1}^{K_i} |\mathbf{d}_{in}|^2},$$

where $\mathbf{d}_{in}$ are distances to the nearest neighbors of the ith atom ($|\mathbf{d}_{in}| \le r_K$) and $D_{im} = |\mathbf{d}_{i(n')} - \mathbf{d}_{i(n'')}|$ are the distances between the corresponding (opposite) nearest neighbors n' and n''.

In order to form the initial configuration, a preliminary molecular dynamics simulation was performed with approaching a given temperature T, beginning with the perfect bcc lattice. The lattice constant a was chosen from the condition of zero pressure in the system for a given initial temperature. From the resulting equilibrium configuration, simulation was performed for the adiabatic conditions for uniaxial tension with a constant rate $\dot{V}$.

RESULTS AND DISCUSSION

To illustrate the typical tension-degree dependences of stresses σ_{zz} and σ_{yy} along and across the tension axis, respectively, as well as corresponding structural transformations, F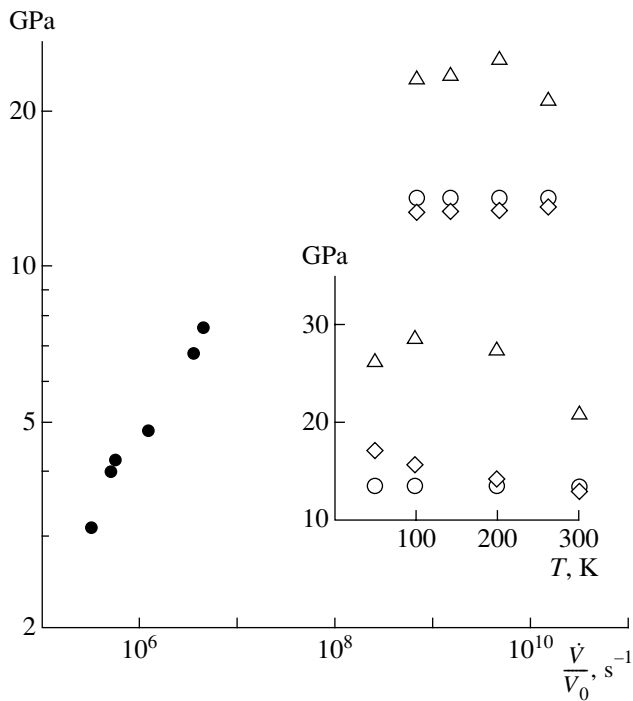igs. 1 and 2 show the simulation results for $\dfrac{\dot{V}}{V_0} = 1.3 \times 10^9 \text{ s}^{-1}$ and $T = 300$ K for the system with $20 \times 20 \times 20$ unit cells in the initial configuration ($a = 2.86$ Å, V_0 is the undeformed calculation-cell volume). First, the body-centered tetragonal (bct) lattice, which is formed in uniaxial tension, is homogeneously deformed. The lattice constant $a_{[001]}$ in the tension direction increases gradually. In this direction, the lattice rigidity decreases gradually, atomic oscillations become anharmonic, and the oscillation amplitude increases, which leads to the appearance of pairs of defect atoms with the coordination number $K = 13$ (see Fig. 2a). As the tension degree increases, the number of such pairs increases and, at $a_{[001]} \approx 3$ Å ($V_B = 1.08V_0$), the lattice loses homogeneity due to the formation of atom clusters with $K = 12$, which form another modification of the bct lattice with $a_{[001]} \approx 3.8$ Å (Fig. 2b). The time of the loss of homogeneity corresponds to a local minimum in the $\sigma_{zz}(V)$ plot in Fig. 1. Since the formation of clusters of the new bct phase is of a local character, it is expected to occur similarly in larger systems, which is checked in this work up to the system consisting of $30 \times 30 \times 20$ unit cells.
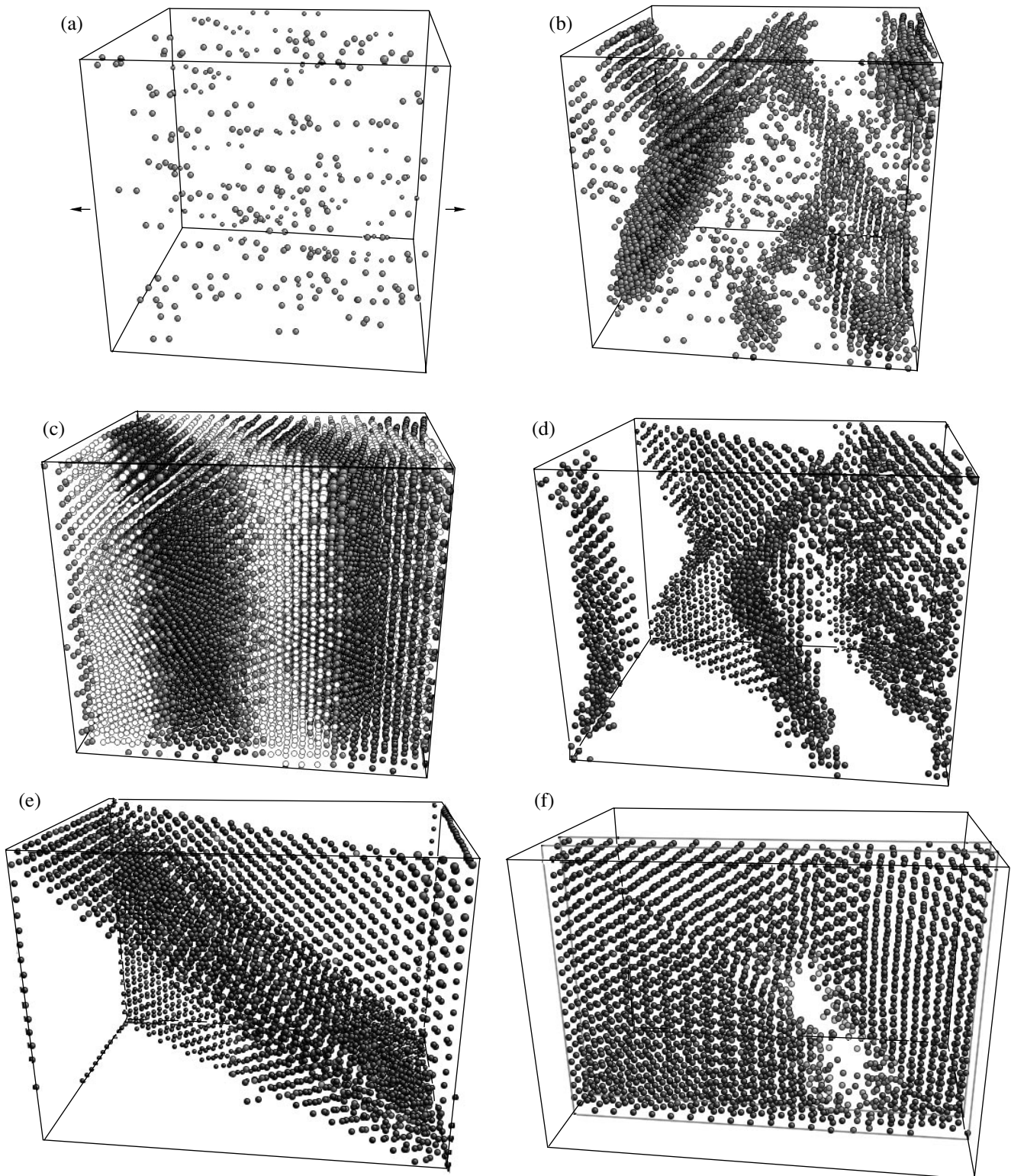
Fig. 2. Arrangements of particles in the simulation box that correspond to the respective points in Fig. 1: (a) atoms with the coordination number $K = 13$ ($r_K = 3.4525$ Å) are shown in grey color, most atoms have $K = 14$ (they are not shown); (b) similar to (a), but atoms with $K = 12$ are also shown in black color; (c) similar to (b), but all atoms are shown (those with $K = 14$, in white color); (d) and (e) atoms for which the local-environment symmetry parameter is $0.033 < C < 0.5$; and (f) to visualize cavities, the structure cross-section in the simulation box is shown, atoms with different coordinate numbers are shown in different colors (most atoms have $K = 12$ and are shown in black color).

Fig. 3. Stress at the times of the characteristic structure changes in the molecular dynamics simulations with various tension rates $\frac{\dot{V}}{V_0}$ for $T = 300$ K. The triangles, circles, and diamonds have the same meaning as in Fig. 1. The closed circles are experimental data for the spall strength of iron [15]. The inset shows the stress at the times of characteristic structural changes for various temperatures at $\frac{\dot{V}}{V_0} = 1.5 \times 10^{10}$ s^{-1}. The calculations are shown for the system with $20 \times 20 \times 20$ unit cells in the initial configuration.

In a time on the order of 10 ps, both crystalline phases bct$_1$ and bct$_2$ with $a_{[001]} \approx 3$ Å, $K = 14$ and $a_{[001]} \approx 3.8$ Å, $K = 12$, respectively, form a layered structure (see Fig. 2c), where the part of the bct$_1$ phases transformed to the bct$_2$ phases increases with further tension. This transition can be classified as a martensitic transformation, because the transition of atoms from one phase to the other in the process of the phase transformation occurs due to displacements by distances smaller than mean interatomic distances, the phase interface holds order, and the rather slight change in the stress σ_{zz} with change in the volume fraction of two phases (*B–C–D* section) indicates that it is a first-order transition. In the calculation-cell size interval, the form of the dependences of σ_{zz}, σ_{xx}, and σ_{yy} on $\frac{V}{V_0}$ does not change. However, in the largest system under investigation ($30 \times 30 \times 20$ unit cells), bct-phase clusters are not joined into layers and the interface has a complex shape in the transition process.

After the end of the martensitic transformation ($V_D = 1.26V_0$), the atomic structure in the simulation box consists of bct$_2$-phase domains separated by boundaries with broken atomic packing. Such a structure is unstable and decays in about 10 ps with the formation of dislocations (see Fig. 2d). As a result of the interaction between dislocations, a structure consisting of several dislocation planes forms in the system. Figure 2e shows a typical example. The number and orientation of the planes depend on the tension rate, temperature, calculation-cell size, and choice of the initial configuration. It is worth noting that the planes are closed to themselves due to periodic boundary conditions. As a result, several grains with the same orientation of the bct$_2$ lattice that are separated by shear planes arise in the system. This structure ensures hardening due to which the crystalline structure exists without qualitative changes to the rather large tension degrees, when cavities are formed ($V_F = 1.43V_0$). In some cases, in the hardening section, the further interaction of dislocation planes or appearance of new planes is possible, which is accompanied by small jumps in the $\sigma_{zz}(V)$ plot. The formation of the cavities occurs primarily in the lines of intersection of dislocation planes at the places of the largest break in the regular packing (see Fig. 3).

The extreme accessible stress depends on the system size (see the inset in Fig. 1). The extrapolation of the calculation results shows that, as the calculation-cell size increases, the difference between the stresses decreases at the time of the formation of cavities, at the time of the loss of the initial lattice homogeneity, and in the further bct$_1$–bct$_2$ phase transition.

Figure 3 shows the calculation results for various tension rates and temperatures. It is interesting that the stress at the end of the bct$_1$–bct$_2$ phase transition is virtually independent of both temperature and the tension rate. Using the available results, one cannot unambiguously determine the dependence of the stress σ_{zz} at the time of the loss of continuity on the tension rate and temperature. As was mentioned above, the time of the formation of cavities depends significantly on the system size and choice of the initial configuration. As the tension rate decreases, the stress corresponding to the time of the loss of the homogeneity of the initial crystalline structure decreases slightly. As temperature decreases, the stress σ_{zz} in the given transition increases, because the formation of bct$_2$-lattice clusters is of a spontaneous fluctuation character and, therefore, may begin at lower tension degrees due to longer "waiting" times or higher temperatures. Owing to computational restrictions, the minimum tension rate used in the molecular dynamics simulations in this work is two orders of magnitude higher than the maximum tension rate in experiment [15]. The dependence of the stress σ_{zz} at the time of the loss of continuity that is observed in the tension-rate interval under investigation is much weaker than (although does not contradict) the depen-

dence of shear strength obtained in shock-wave experiments with iron single crystals [15].

CONCLUSIONS

Mechanisms of elastoplastic deformation and of the loss of the continuity of crystalline iron subjected to high-rate uniaxial tension has been investigated by the molecular dynamics method for strain rates from 1.3×10^7 to 1.3×10^{10} s^{-1}. Sharp structural transitions occur at the times of the loss of mechanical stability and are separated by longer sections of smooth variations.

The transition of deformation from the elastic regime to the plastic one is accompanied by the concentration of defects in clusters forming an alternating crystalline phase. The first stage of plastic deformation is a martensitic transformation between two bct phases. At this stage, the possibility of forming a characteristic layered structure is found. At the second stage of plastic deformation, hardening occurs due to the formation of the system of dislocation (shear) planes. The formation of discontinuities (nuclei of microcracks) is of a random character of heterogeneous nucleation and occurs primarily at places of the intersection of dislocation planes.

Stress at the time of the loss of continuity has been obtained for various strain rates and temperatures. The results do not contradict the experimental data [15] on the shear strength of iron.

ACKNOWLEDGMENTS

REFERENCES

1. V. P. Skripov and M. Z. Faĭzullin, *Crystal–Fluid–Vapor Phase Transitions and Thermodynamic Similarity* (Fizmatlit, Moscow, 2003) [in Russian].

2. L. B. Freund, *Dynamic Fracture Mechanics* (Cambridge Univ. Press, Cambridge, 1998).

3. G. I. Kanel', S. V. Razorenov, A. V. Utkin, and V. E. Fortov, *Shock–Wave Phenomena in Condensed Matter* (Yanus-K, Moscow, 1996) [in Russian].

4. C. G. Wang, U. Landman, R. L. B. Selinger, and W. M. Gelbart, Phys. Rev. B **44**, 378 (1991).

5. R. M. Lynden-Bell, J. Phys.: Condens. Matter **7**, 4603 (1995).

6. J. Belak, J. Comput.-Aided Mater. Des. **5**, 193 (1998).

7. A. Machová and G. J. Ackland, Modell. Simul. Mater. Sci. Eng. **6**, 521 (1998).

8. R. E. Rudd and J. F. Belak, Comput. Mater. Sci. **24**, 148 (2002).

9. A. M. Krivtsov, Fiz. Tverd. Tela (St. Petersburg) **46**, 1025 (2004) [Phys. Solid State **46**, 1055 (2004)].

10. G. V. Sin'ko and N. A. Smirnov, Pis'ma Zh. Éksp. Teor. Fiz. **79**, 665 (2004) [JETP Lett. **79** (11), 537 (2004)].

11. M. I. Mendelev, S. Han, D. J. Srolovitz, *et al.*, Philos. Mag. **83** (35), 3977 (2003).

12. A. A. Valuev, G. É. Norman, and V. Yu. Podlipchuk, in *Mathematical Simulation. Physicochemical Properties of Substances*, Ed. by A. A. Samarskiĭ and N. N. Kalitkin (Nauka, Moscow, 1989), pp. 5–40 [in Russian].

13. C. L. Kelchner, S. J. Plimpton, and J. C. Hamilton, Phys. Rev. B **58**, 11085 (1998).

14. Ju Li, Modell. Simul. Mater. Sci. Eng. **11**, 173 (2003).

15. S. V. Razorenov, G. I. Kanel', and V. E. Fortov, Pis'ma Zh. Éksp. Teor. Fiz. **80**, 395 (2004) [JETP Lett. **80**, 348 (2004)].

Translated by R. Tyapaev

===== **MECHANICS** =====

3D Configurations of Broken Body Fragments in a Supersonic Flow

I. A. Zhdan, V. P. Stulov*, and P. V. Stulov

Presented by Academician G.G. Chernyǐ May 11, 2005

The current state of computers and computational methods has made it possible to conduct numerical aerodynamic experiments for complicated solid systems. We consider a supersonic flow over systems of spheres whose centers form spatial configurations relative to the uniform flow.

It was previously suggested [1] that the study of a supersonic flow over systems of spherical bodies given the simplest configuration of their elements—when the centers of all spheres are located in the flow plane—could provide conclusions that apply to the more complicated cases of spatial and irregular locations. To verify this assumption, we studied flows over spheres whose centers lie in the plane perpendicular to the incoming flow, as well as flows over pyramids and prisms. The results of the calculations and their analysis are discussed in this study.

Nine configurations were chosen for the investigation of supersonic aerodynamics. In six cases, the centers of the spheres were located in one plane, while in the other three cases they lay in the vertices and in the middles of the edges of a tetrahedron and two prisms. For convenience of reference, the systems of spheres are designated by letters, following the designations from [1], where configurations *a–d* were considered. These designations, along with brief descriptions of the sphere center configurations, are as follows:

(*e*) three spheres with the centers at the vertices of a regular triangle with the side $2(h+1)$;

(*f*) four spheres at the vertices of a square with the side $2(h+1)$;

(*g*) six spheres in the vertices and middles of the edges of the triangle with the side $4(h+1)$;

(*h*) nine spheres equally spaced in the square with the side $4(h+1)$;

(*i*) 16 spheres uniformly located in the square with the side $6(h+1)$;

(*j*) an infinite rectangular lattice with the step $2(h+1)$;

(*k*) four spheres at the vertices of a tetrahedron with the side $2(h+1)$;

(*l*) 12 spheres at the vertices and middles of the edges of a right triangular prism with the sides $4(h+1)$ and height $2(h+1)$;

(*m*) 18 spheres at the vertices and in the middles of the edges, as well as at the centers of side faces, of the right triangular prism with the sides $4(h+1)$.

In six cases (*e–j*), the uniform incoming flow is perpendicular to the plane of the sphere centers; the incoming flow in the case *k* is orthogonal to the face of the tetrahedron; and the flow in the cases *l* and *m* is orthogonal to the side face of the prism.

The characteristic configuration size *h* is equal to the ratio of half the distance between the two nearest points of neighboring spheres to the sphere radius *R*. All calculations are conducted for the perfect gas flow with $\gamma = 1.4$ and M = 6. The aim of the calculations is to determine the drag coefficients, transverse forces, and the configuration of shock waves as functions of *h*.

Let us note that the main characteristics of the supersonic flow over systems of spherical bodies considered previously for the configurations *a–d* [1] are retained in these calculations. The mutual influence of the spheres is almost eliminated at $h = 0.5$. Drag coefficients c_x approach the value for an isolated sphere in an unbounded flow. Similar to [1], the exception is the situation in which the side regions of the bow shock waves or reflected shock waves fall on the front surface of the sphere from the rear rows. In this case, c_x at much larger distances can significantly exceed c_x of an isolated sphere.

The coefficient of the force that lies in the plane orthogonal to the incoming flow and passes through the sphere center is taken as a coefficient of transverse force c_y. This coefficient also vanishes at $h = 0.5$. The common bow shock wave at the front of all configurations breaks into individual shock waves in front of each sphere at $h \sim 0.5$.

Institute of Mechanics, Moscow State University, Michurinskiǐ pr. 1, Moscow, 119192 Russia
* *e-mail: stulov@imec.msu.ru*

Table 1. Drag coefficients c_x of the spheres

Case, sphere	0.025*	0.1	0.2	0.25	0.3	0.4	0.5
e	1.131	1.090	1.030	0.978	0.796	0.813	0.842
f	1.165	1.135	1.072	0.796	0.804	0.810	0.823
g, middle	1.365	1.276	1.209	1.169	0.713	0.753	–
g, corner	1.090	1.089	1.070	1.040	0.800	0.816	–
i, inner	1.529	1.441	1.326	0.660	0.658	0.755	0.783
i, middle	1.283	1.256	1.185	0.754	0.757	0.791	0.821
i, corner	1.103	1.111	1.090	0.797	0.797	0.818	0.841
j	–	1.630	1.486	0.677	0.690	0.771	0.780

* Hereafter, the h values are given in horizontal.

Table 2. Transverse force coefficients c_y of the spheres

Case, sphere	0.025	0.1	0.2	0.25	0.3	0.4	0.5
e	0.455	0.430	0.417	0.398	0.160	0.038	0.001
f	0.501	0.488	0.460	0.156	0.087	0.018	0.004
g, middle	0.486	0.439	0.406	0.409	0.199	0.034	–
g, corner	0.431	0.443	0.429	0.418	0.151	0.034	–
i, inner	0.047	0.055	0.046	0.031	0.013	0.004	0.002
i, middle	0.516	0.469	0.426	0.099	0.054	0.003	0.008
i, corner	0.553	0.538	0.500	0.138	0.082	0.012	0.011

Numerous individual features of the flow over the configurations under study allow us to significantly broaden the understanding of the aerodynamics of a system of bodies in the supersonic flow.

The flows over configurations $e–j$ were previously studied in computations [2] and experiments with wind tunnels [3]. Seven configurations were considered in [2] and two of them coincide with our cases b [1] and e. The calculated pressure fields including pressure distributions on the sphere surfaces under the interference conditions were presented. However, the values of the transverse force were not given in [2].

The experimental values of the separation of a shock wave in the supersonic flow over a square flat lattice with the side L as a function of lattice permittivity were provided in [3]. The separation of the shock wave decreases with an increase in permittivity. These data can be used to verify the computational model of a flow over a cloud with a large number of fragments.

The drag coefficients c_x calculated for the systems e, f, g, i, and j are presented in Table 1. Note that the sphere centers in these systems lie in the plane orthogonal to the incoming flow. The following terminology is used: the center of the corner sphere lies at the verti-

ces of the triangle in systems e and g and of the square in systems f and h; the middle sphere is located in the middles of the triangle sides in the system g and on the sides of the outer square in the system i; and the inner sphere is located at the vertex of the square that has the side $2(h +1)$ and lies inside the outer square with the side $6(h +1)$ in the system i.

When the distances between spheres are small ($h < 0.25$), the drag coefficient c_x depends strongly on the "load factor," i.e., on the number of spheres in the system and on their locations. This dependence is clearly seen in Fig. 1, where the dependences $c_x(h)$ are presented for configurations e and i. The differences are caused by the shape of the common bow shock wave under the specified conditions. It is seen that the coefficient c_x of the spheres located closer to the system center exceeds the coefficient c_x for peripheral spheres; i.e., the value of the flow spreading accompanied by the pressure fall on the front surface exceeds the flow spreading value for the inner spheres. Correspondingly, the parts of the bow shock wave in front of the inner spheres are closer to the normal shock than those for the peripheral spheres (the corner spheres for the configurations e and i).
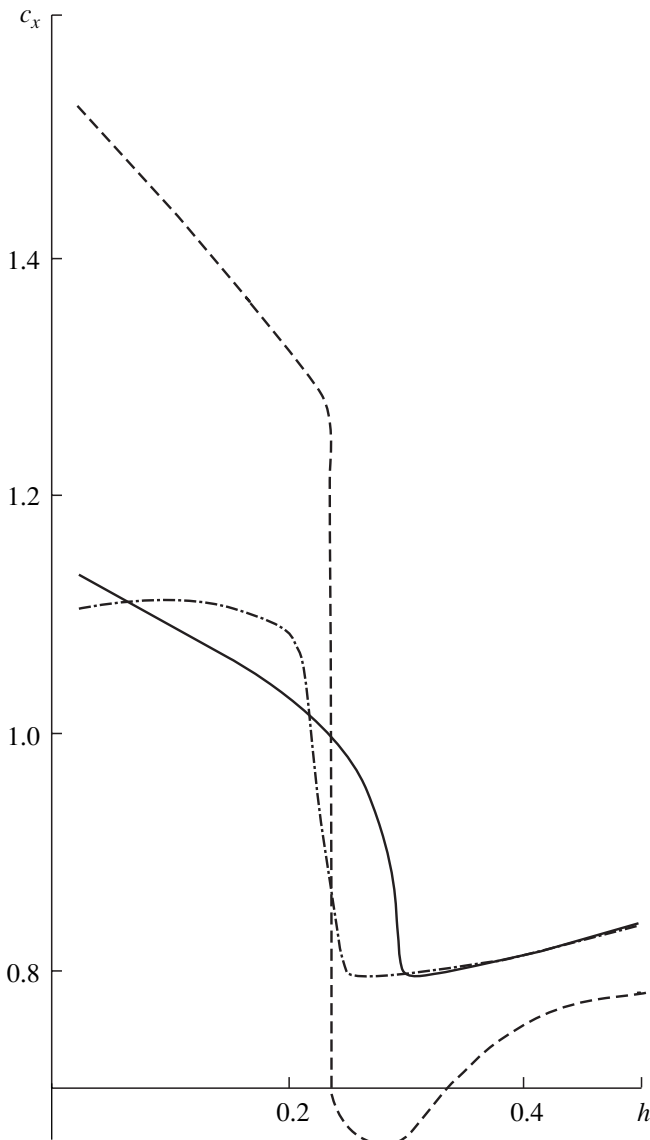
Fig. 1. Drag coefficient in cases (solid line) *e* and (dashed line for the corner sphere and dash–dotted line for the inner sphere) *i*.

Note also a certain decrease in c_x at $h \geq 0.3$ in comparison with an isolated sphere. This decrease is attributed to the fall of the reflected shock on the rear part of the sphere, which leads to a certain increase in bottom pressure. This fact was not previously mentioned in [1], because the decrease in c_x there was attributed to the more significant increase in the bottom pressure due to the support effect from the rear rows of the spheres. The support effect due to the reflected shocks is significantly higher for the inner sphere than for the corner spheres.

The transverse force coefficients c_y calculated for the systems *e*, *f*, *g*, and *i* are presented in Table 2. Figure 2 shows $c_y(h)$ for the same cases as in Fig. 1.
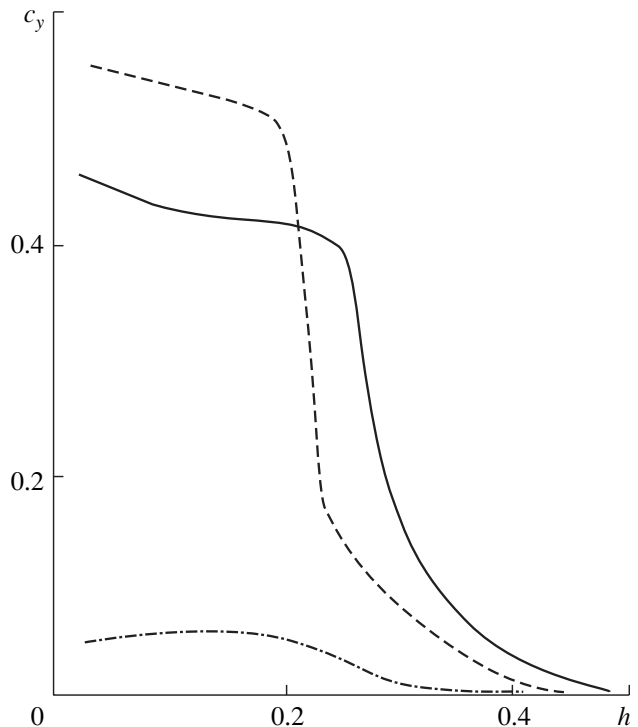
Fig. 2. Same as in Fig. 1, but for the transverse force coefficient.

We first point to the increase in the transverse force coefficient as compared to the simplest case of the flow over two spheres [1]. The dependence $c_y(h)$ remains qualitatively unchanged. Finally, it should be noted that the transverse force in the configuration *i* for the inner spheres is significantly smaller than the value for the peripheral spheres. All these facts can be explained by the character of the evolution of the bow shock wave with an increase in *h*. For example, the decrease in c_y for the inner spheres can be explained by the fact that the reflected shock waves fall on the inner spheres from both sides for almost all *h* values, whereas they fall on the peripheral spheres from one, inner side.

The above features allow us to generalize the computation procedure developed in [4] for the scattering of two fragments to the case of multiple breakups. First, the c_y value in the equations in [4] should be increased at the matching point of linear approximations for the multiple breakups. Second, the solution should be modified taking into account the stage-by-stage separation of peripheral fragments. At each stage, the debris cloud should be considered as a binary complex, consisting of one central and several peripheral fragments.

The above-described important property of the supersonic flow over the debris cloud is also demonstrated in Fig. 3 by the example of pressure distribution for the cases *h* and *i*. This figure illustrates the pressure change related to the pressure in the incoming flow along the large circle of cross sections of the corner

(case h) and inner (case i) spheres. These cross sections contain the incoming flow velocity and are orthogonal to a side of the square formed by the centers of the corner spheres. The value $s = \sin\varphi$, $-\dfrac{\pi}{2} \leq \varphi \leq \dfrac{3\pi}{2}$ is shown along the abscissa with the upstream point of the sphere corresponding to $\varphi = -\dfrac{\pi}{2}$. Solid lines are the results for the case h; the curve with a local maximum corresponds to the inner side of the sphere $\left(\text{i.e., to the configuration facing inside, } -\dfrac{\pi}{2} \leq \varphi \leq \dfrac{\pi}{2}\right)$, and the smooth curve corresponds to the outer side $\left(\dfrac{\pi}{2} \leq \varphi \leq \dfrac{3\pi}{2}\right)$. The dashed lines refer to the configuration i, where the upper curve is for $-\dfrac{\pi}{2} \leq \varphi \leq \dfrac{\pi}{2}$ and the lower curve is for $\dfrac{\pi}{2} \leq \varphi \leq \dfrac{3\pi}{2}$. The corner (case h) and inner (case i) spheres experience the reflected shock from one and both sides, respectively. It is this small difference between the dashed curves that results in the small value of the transverse force coefficient for the inner sphere, which is shown in Fig. 2.

The calculation results for the tetrahedron (case k) and two prisms (cases l and m) are shown in Fig. 4. The calculation results for prisms are presented in detail in Table 3. For convenience of illustration, the double scale (linear for $0 \leq 2h \leq 1$ and logarithmic for $1 \leq 2h \leq 5$) is used for abscissa in Fig. 4. For the flow over the tetrahedron, the solid line is the drag coefficient c_x for the first-row sphere, the dashed line is the drag coefficient c_x for the second-row sphere at the vertex of the tetrahedron, and the dash–dotted line is the transverse-force coefficient for the first-row sphere. As h increases, the coefficients c_x and c_y change qualitatively in a manner that is similar to the case of three spheres with the centers lying in the plane along the flow direction (case c in [1]). The drag of the rear sphere grew sharply due to the effect of bow shock waves from the front spheres.

The markers in Fig. 4 illustrate the aerodynamic coefficients of 4 out of 18 spheres of the prism in the case m. The upper and lower markers in each pair show c_x and c_y, respectively. The same data are presented in Table 3 for 12 spheres of the system l and all 18 spheres of the system m at two values of the distance h. The change in c_x as compared to the isolated sphere in the unbounded flow is again determined by three factors. First, the support effect of the rear rows reduces the drag of the front spheres. Second, the fall of the
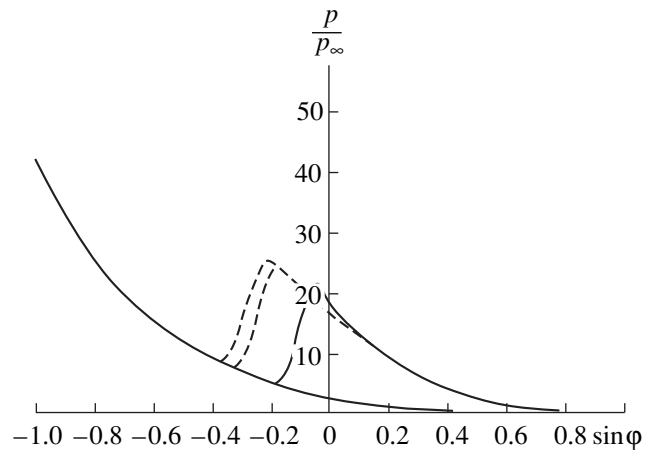

Fig. 3. Pressure distribution over a large circle in cases (solid lines) h and (dashed lines) i.
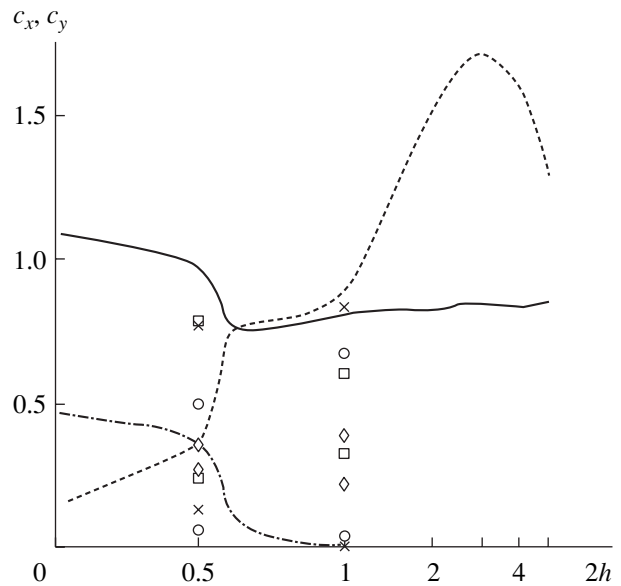

Fig. 4. Drag coefficient and transverse force coefficient for cases k (the solid and dashed lines are c_x for the first- and second-row spheres, respectively, and the dash–dotted line is c_y) and m (circles correspond to the middle sphere in the first row and side layer, crosses are for the corner sphere in the first row and side layer, squares correspond to the second-row sphere in the central layer, and diamonds are for the third-row sphere in the side layer. In all cases, $c_x > c_y$).

reflected shock on the rear side of the sphere reduces drag. Third, the fall of the front-sphere shock on the front side of the rear sphere increases drag. The combined action of all three factors is possible in the complex configurations discussed above.

Computations have shown that the evolution of the bow shock wave in complex configurations with an increase in h is similar to the evolution in simple systems: the monotonic decay of the common shock wave

Table 3. Drag coefficient c_x and transverse force coefficient c_y of the spheres

Case, sphere	0.25		0.5	
	c_x	c_y	c_x	c_y
l, middle in the first row	0.524	0.115	0.645	0.018
l, corner in the first row	0.756	0.138	0.803	0.008
l, second row;	0.602	0.323	0.632	0.170
l, third row	0.374	0.247	0.365	0.201
m, middle in the first row and central layer	0.203	0	0.527	0
m, middle in the first row and side layer	0.493	0.063	0.668	0.033
m, corner in the first row and central layer	0.646	0.112	1.121	0.471
m, corner in the first row and side layer	0.744	0.133	0.821	0.009
m, second row and central layer	0.773	0.258	0.601	0.325
m, second row and side layer	0.639	0.379	0.627	0.199
m, third row and central layer	0.616	0	0.353	0
m, third row and side layer	0.365	0.269	0.368	0.222

Note: The first, second, and third rows are enumerated streamwise, and the central and side layers are counted across the flow.

into the individual shock waves in front of each sphere occurs at least in the front rows.

REFERENCES

1. I. A. Zhdan, V. P. Stulov, and P. V. Stulov, Dokl. Akad. Nauk **399** (2), 199 (2004) [Dokl. Phys. **49**, 315 (2004)].
2. A. A. Andreev and A. S. Kholodov, Zh. Vychisl. Mat. Mat. Fiz. **29** (1), 142 (1989).
3. S. V. Guvernyuk, G. S. Ul'yanov, and S. A. Antonova, *Flows Over Multiply Connected Bodies*, Available from VINITI, No. 6614-V86 (Moscow, 1986).
4. N. G. Barri, Vestn. Mosk. Univ., Ser. 1: Mat., Mekh. **4**, 54 (2005).

Translated by B. Chernyavsky

===== **MECHANICS** =====

On the Solution of Equations of the Linear Oscillator with Respect to the Matrix of the Inertial Trihedron

Academician V. F. Zhuravlev

Received March 24, 2005

It is known that problems of mechanics underlain by Newton's laws consist either in determining the applied forces by a given motion (the first problem of mechanics) or in determining the motion by given forces (the second problem of mechanics).

The third problem of mechanics consists in determining the motion of the noninertial frame in which the behavior of some material system under the action of a specified force is known from observation. This statement of the problem is typical of inertial navigation [1, 2].

A possible way to solve this problem consists in assuming that the following are known: the projections of the angular velocity of the moving frame of reference, as well as the projections of the absolute acceleration of its origin, onto its axes. Then, the attitude of the moving axes is determined by solving the Poisson kinematic equations; the velocity and location of the moving origin are determined by integrating the acceleration already projected onto the inertial axes.

To solve this problem, three gyroscopes and three newton-meters are required.

In this paper, complete information about the behavior of the moving frame of reference is obtained from the observed vibrations of a spatial isotropic oscillator.

First, we assume that the moving object rotates about a fixed point, which coincides with the center of vibration of the oscillator. Then, in the inertial reference system, the equations of the spatial isotropic oscillator exposed only to elastic forces have the form

$$\ddot{\mathbf{x}} + \mathbf{x} = 0, \quad \mathbf{x} = (x_1, x_2, x_3). \tag{1}$$

Here, the natural frequency of the oscillator determines the time unit measure.

To write the equations of motion in the object-centered reference system

$$\ddot{\mathbf{y}} + \mathbf{y} + 2A^T \dot{A}\dot{\mathbf{y}} + A^T \ddot{A}\mathbf{y} = 0, \tag{2}$$

Institute for Problems in Mechanics,
Russian Academy of Sciences,
pr. Vernadskogo 101, Moscow, 119526 Russia

we pass from $\mathbf{x}$ to $\mathbf{y}$ by an orthogonal transformation with matrix A:

$$\mathbf{x} = A\mathbf{y}. \tag{3}$$

In the most general statement, the problem formulated for Eqs. (2) consists in reconstructing the orientation matrix $A(t)$ by the observed vibrations $y(t)$ of the oscillator in the object-centered reference system.

Introduce the angular velocity matrix $\Omega = A^T \dot{A}$. Then, the second-order equations (2) with respect to the desired matrix A can be written as a system of two equations of the first order:

$$\dot{\Omega}\mathbf{y} = -\Omega^2\mathbf{y} - 2\Omega\dot{\mathbf{y}} - \ddot{\mathbf{y}} - \mathbf{y},$$

$$\dot{A} = A\Omega.$$

Here, the first equation is the Riccati equation for the angular velocity matrix Ω and the second one is the Poisson equation for matrix A.

Now, we assume that the natural frequency of the oscillator is far above the modulus of the angular velocity of the moving object. Then, an approximate solution to system (2) with respect to matrix $A(t)$ can be sought in the form of a step function $A(t) = \text{const}$ for

$$2\pi(n-1) < t < 2\pi n.$$

Here, n runs through all integers (Fig. 1).

It is known from the theory of the Riemann integral that a sequence of step functions uniformly converges to a function $A(t)$ if this function is continuous or has discontinuities of only the first kind. This means that, for any accuracy of calculation of matrix A, one can always choose a natural period of vibrations of the oscillator such that the required accuracy is guaranteed. In particular, if function $A(t)$ is smooth, then the natural period of vibrations can be easily estimated from above with the use of the upper estimate for the norm of the derivative of this function.
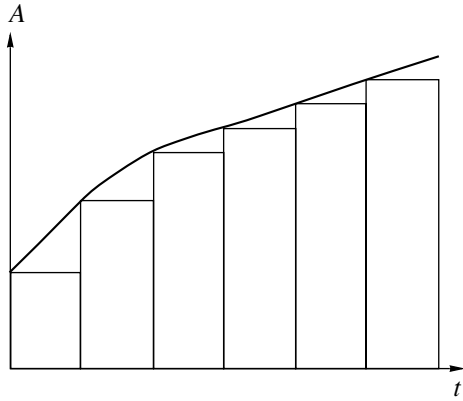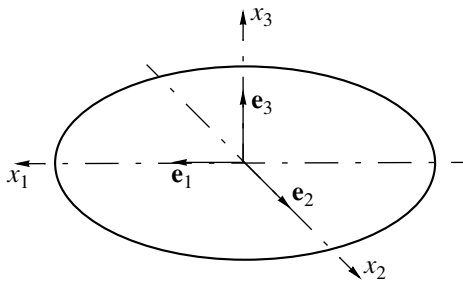
Fig. 1.

Fig. 2.

On each interval, the general solution to system (2) has the form

$$\mathbf{y} = \mathbf{u}\cos t + \mathbf{v}\sin t, \tag{4}$$

where $\mathbf{u}$ and $\mathbf{v}$ are arbitrary three-dimensional constant vectors. It is obvious that such a solution is exact for equations in the inertial reference system. The meaning of the approximate solution (4) is clear: during one period of vibration of the oscillator, the vibration shape in the object-centered reference system is changed negligibly.

Relations (4) determine the parametric representation of an arbitrary ellipse including the particular cases of straight line segments passing through the origin and circles centered at the same origin. Introduce the following notation (see Fig. 2):

$\mathbf{e}_1$ is the unit vector of the major semiaxis of the ellipse, and r is the length of this semiaxis;

$\mathbf{e}_2$ is the unit vector of the minor semiaxis, and k is the length of this semiaxis;

$\mathbf{e}_3$ is the unit normal to the ellipse plane ($\mathbf{e}_3 = \mathbf{e}_1 \times \mathbf{e}_2$).

These vectors are the columns of the matrix $A = \|\mathbf{e}_1\ \mathbf{e}_2\ \mathbf{e}_3\|$. This matrix relates the representation of the

ellipse in the moving axes with that in the inertial reference system:

$$A(\mathbf{u}\cos t + \mathbf{v}\sin t) = \left\|\begin{array}{c} r\cos(t+\tau) \\ k\sin(t+\tau) \\ 0 \end{array}\right\|$$

$$= \left\|\begin{array}{c} r\cos\tau \\ k\sin\tau \\ 0 \end{array}\right\|\cos t + \left\|\begin{array}{c} -r\sin\tau \\ k\cos\tau \\ 0 \end{array}\right\|\sin t. \tag{5}$$

Here, angle τ determines the point location on the ellipse at instant $t = 0$.

Let us explicitly express this matrix in terms of arbitrary constant vectors $\mathbf{u}$ and $\mathbf{v}$. For this purpose, we note that relation (5) is equivalent to the following two relations:

$$A\mathbf{u} = \left\|\begin{array}{c} r\cos\tau \\ k\sin\tau \\ 0 \end{array}\right\|, \quad A\mathbf{v} = \left\|\begin{array}{c} -r\sin\tau \\ k\cos\tau \\ 0 \end{array}\right\|, \tag{6}$$

and calculate the vector product of vectors (6):

$$A\mathbf{u} \times A\mathbf{v} = \left\|\begin{array}{c} r\cos\tau \\ k\sin\tau \\ 0 \end{array}\right\| \times \left\|\begin{array}{c} -r\sin\tau \\ k\cos\tau \\ 0 \end{array}\right\| = \left\|\begin{array}{c} 0 \\ 0 \\ K \end{array}\right\|. \tag{7}$$

The value $K = rk$ is the modulus of the angular momentum of the vibrating particle; it is called the quadrature (πrk is the ellipse area).

By virtue of the rotational invariance of the vector product, the identity $A\mathbf{u} \times A\mathbf{v} = A(\mathbf{u} \times \mathbf{v})$ holds, and we can write the following matrix equation:

$$A\|\mathbf{u}\ \mathbf{v}\ \mathbf{u}\times\mathbf{v}\| = \left\|\begin{array}{ccc} r\cos\tau & -r\sin\tau & 0 \\ k\sin\tau & k\cos\tau & 0 \\ 0 & 0 & K \end{array}\right\| = B. \tag{8}$$

This equation may be explicitly solved for matrix A:

$$A = B\|\mathbf{u}\ \mathbf{v}\ \mathbf{u}\times\mathbf{v}\|^{-1} \quad (\mathbf{u}\times\mathbf{v} \neq 0). \tag{9}$$

If $\mathbf{u} \times \mathbf{v} = 0$, then the ellipse degenerates into a straight line segment, the information about the object rotation around this straight line is lost, and this results in the degeneration of the matrix A.

Expressing r, k, and τ in terms of arbitrary constant vectors $\mathbf{u}$ and $\mathbf{v}$, we can express matrix A, which determines the attitude of ellipse (4) relative to the original trihedral, in terms of only $\mathbf{u}$ and $\mathbf{v}$, i.e., in terms of the observation data only. Since ellipse (4) remains fixed in

the inertial reference system under rotations of this trihedral, matrix A determines the attitude of the moving object in the absolute space.

To find the required parameters, let us calculate the scalar product of vectors (6) and their scalar squares:

$$\mathbf{u} \cdot \mathbf{u} = A\mathbf{u} \cdot A\mathbf{u} = \left\| \begin{matrix} r\cos\tau \\ k\sin\tau \\ 0 \end{matrix} \right\| \cdot \left\| \begin{matrix} r\cos\tau \\ k\sin\tau \\ 0 \end{matrix} \right\|$$
$$= r^2\cos^2\tau + k^2\sin^2\tau;$$

$$\mathbf{u} \cdot \mathbf{v} = A\mathbf{u} \cdot A\mathbf{v} = \left\| \begin{matrix} r\cos\tau \\ k\sin\tau \\ 0 \end{matrix} \right\| \cdot \left\| \begin{matrix} -r\sin\tau \\ k\cos\tau \\ 0 \end{matrix} \right\|$$
$$= (k^2 - r^2)\cos\tau\sin\tau; \tag{10}$$

$$\mathbf{v} \cdot \mathbf{v} = A\mathbf{v} \cdot A\mathbf{v} = \left\| \begin{matrix} -r\sin\tau \\ k\cos\tau \\ 0 \end{matrix} \right\| \cdot \left\| \begin{matrix} -r\sin\tau \\ k\cos\tau \\ 0 \end{matrix} \right\|$$
$$= r^2\sin^2\tau + k^2\cos^2\tau.$$

Relations (10) imply

$$\mathbf{u}^2 + \mathbf{v}^2 = r^2 + k^2, \quad \mathbf{u}^2 - \mathbf{v}^2 = (r^2 - k^2)\cos 2\tau. \tag{11}$$

This finally gives

$$\binom{r}{k} = \sqrt{\frac{1}{2}[\mathbf{u}^2 + \mathbf{v}^2 \pm \sqrt{(\mathbf{u}^2 - \mathbf{v}^2)^2 + 4(\mathbf{u} \cdot \mathbf{v})^2}]},$$
$$\tag{12}$$
$$\tan 2\tau = \frac{2\mathbf{u} \cdot \mathbf{v}}{\mathbf{v}^2 - \mathbf{u}^2}, \quad \mathbf{u}^2 - \mathbf{v}^2 \neq 0.$$

Note that the quadrature $K = rk$ present in (8) and (9) can also be calculated directly via u and v. Relations (12) imply

$$rk = \sqrt{\mathbf{u}^2\mathbf{v}^2 - (\mathbf{uv})^2} = |\mathbf{u} \times \mathbf{v}|. \tag{13}$$

In the case where $\mathbf{u}^2 - \mathbf{v}^2 = 0$ and $\mathbf{u} \cdot \mathbf{v} = 0$ at the same time, angle τ is undefined, and it is seen from (12) that the point traces out a circle.

Together with (9), equalities (12) complete the construction of matrix A, which determines the attitude of the moving trihedron with respect to the fixed one, in the case where the trajectory of the oscillator in the inertial reference system is neither a line segment nor a circle.

Relations (9) and (12) are of a general nature; they are independent of the way the vector constants $\mathbf{u}$ and $\mathbf{v}$

are calculated by the measurement data. However, these expressions can be significantly simplified by particularizing the measurement procedure for $\mathbf{u}$ and $\mathbf{v}$. Assume that the test oscillator involved in the measurements has the same frequency as the oscillator under consideration. This oscillator allows determining $\mathbf{y}(t)$ at particular time instants. Therefore, in accordance with (4), the required constants may be found in the following way:

$$\mathbf{u} = \mathbf{y}(2\pi(n-1)), \quad \mathbf{v} = \mathbf{y}\left(\frac{\pi}{2} + 2\pi(n-1)\right),$$
$$n = 1, 2, \ldots. \tag{14}$$

Then, using the feedback, one can introduce a correction for the test oscillator frequency, which is proportional to the scalar product of vectors (14): $\dot{\tau} = a(\mathbf{u} \cdot \mathbf{v})$. By virtue of (10), this gives the equation

$$\dot{\tau} = a(k^2 - r^2)\sin\tau\cos\tau, \tag{15}$$

which implies that, for $a > 0$, the test oscillator adjusts itself to the asymptotically stable mode, in which $\tau = 0$. At the measurement instants chosen in this way, the product $\mathbf{u} \cdot \mathbf{v} = 0$ and formulas (12) take the form

$$r = |\mathbf{u}|, \quad k = |\mathbf{v}|, \quad \tau = 0. \tag{16}$$

This allows finding matrix A in the form

$$A = \left\| \begin{matrix} |\mathbf{u}| & 0 & 0 \\ 0 & |\mathbf{v}| & 0 \\ 0 & 0 & |\mathbf{u} \times \mathbf{v}| \end{matrix} \right\| \|\mathbf{u} \ \mathbf{v} \ \mathbf{u} \times \mathbf{v}\|^{-1}$$
$$= \left\| \frac{\mathbf{u}}{|\mathbf{u}|} \ \frac{\mathbf{v}}{|\mathbf{v}|} \ \frac{\mathbf{u} \times \mathbf{v}}{|\mathbf{u} \times \mathbf{v}|} \right\|^T. \tag{17}$$

In the second equality here, the inverse matrix is replaced with the transposed one, which is the same due to its orthogonality.

The elliptic trajectory (4) of the isotropic spatial oscillator (2) is not stable under indefinitely small perturbations. In particular, the rigidity being slightly varied

$$\ddot{\mathbf{x}} + (E + C)\mathbf{x} = 0$$

(here, E is the identity matrix and C is a symmetrical matrix with a small norm), the trajectory is generally no longer planar and closed and the above algorithm for constructing matrix A is unrealizable.

Here, if perturbation C is small, then the fall of the trajectory outside the plane can be treated as a slow rotation of this plane in the inertial space, i.e., as a "deviation" of the gyroscope constructed above. In this case, the implementation of the above presented algo-
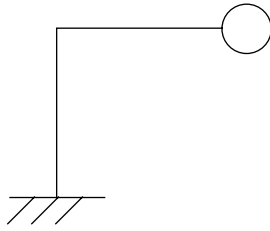
Fig. 3.

rithm runs into no difficulties. The situation is different if the ellipse evolves within the plane. For small variations of the rigidity, the ellipse alternately (with a certain period) degenerates into a circle and into a straight line segment. These are the cases in which the measurements cannot be made.

In the case of a small dissipation

$$\ddot{\mathbf{x}} + D\dot{\mathbf{x}} + \mathbf{x} = 0,$$

the vibration amplitude tends to zero, which makes the measurements impossible.

In order for the spatial isotropic oscillator to be realizable in practice as a gyroscope, control actions that provide its stability under small perturbations should be introduced into Eqs. (2). However, it is impossible in principle to ensure the stability of the plane of vibrations of the oscillator, i.e., to guarantee such a gyroscope from deviation. For this reason, we do not even pose this problem. On the other hand, the orbital asymptotic stability of a specified elliptic trajectory in the vibration plane can be ensured and this circumstance is sufficient for the above-presented algorithm for constructing the orientation matrix A to be realizable.

This problem is solved in [3, 4], where it is demonstrated that the equation

$$\ddot{\mathbf{x}} + \mathbf{x} = \mu(K - K_0)J\mathbf{x} + \varepsilon(1 - \mathbf{x}^2 - \dot{\mathbf{x}}^2)\dot{\mathbf{x}}, \qquad (18)$$

where

$$\mathbf{x} = \left\| \begin{matrix} x_1 \\ x_2 \end{matrix} \right\|, \quad J = \left\| \begin{matrix} 0 & 1 \\ -1 & 0 \end{matrix} \right\|,$$

possesses the asymptotically stable integral variety

$$2E = \mathbf{x}^2 + \dot{\mathbf{x}}^2 = r^2 + k^2 = 1, \quad |\mathbf{x} \times \dot{\mathbf{x}}| = K = K_0. \quad (19)$$

The first relation in (19) signifies the constancy of the vibration energy and the second relation signifies the constancy of the quadrature. System (18) determines the plane oscillator into which the original oscillator can be brought by means of transformation with

matrix A (9). With (3) in mind, one can write the three-dimensional version of Eq. (18) in the form

$$\ddot{\mathbf{y}} + \mathbf{y} = \mu(K - K_0)J^*\mathbf{y} + \varepsilon(1 - \mathbf{y}^2 - \dot{\mathbf{y}}^2)\dot{\mathbf{y}} \\ + 2A^T\dot{A}\dot{\mathbf{y}} + A^T\ddot{A}\mathbf{y} = 0, \qquad (20)$$

where

$$J^* = A^T \left\| \begin{matrix} 0 & 1 & 0 \\ -1 & 0 & 0 \\ 0 & 0 & 0 \end{matrix} \right\| A.$$

In this equation, it is taken into account that the quadrature K and the total energy E are invariant under the action of the orthogonal group.

The forces applied to the pendulum in accordance with (20) stabilize the vibrations with constant amplitude and constant quadrature and provide the validity of the above-presented algorithms.

In practice, such a gyroscope can be implemented, for example, with the use of six Γ-shaped elastic rods that make up a spatially isotropic elastic suspension (see Fig. 3).

The rods are of square section and are equipped with piezoelectric force sensors and information sensors mounted on their side faces. Devices of this kind should be considered as low-accuracy vibratory gyroscopes for wide use [5, 6].

The gyroscope can also be implemented with the use of a uniform ball in an electromagnetic suspension.

Remark 1. It is assumed above that the moving object only rotates about the center of the oscillator. If the motion is of a general nature, then the right-hand sides of system (2) contain slowly varying terms due to the projections of the apparent acceleration onto the axes of the device. As a result, the harmonic high-frequency solution (4) should be corrected by means of the addition of a slowly varying component. In this case, the realization of the algorithm described above should be preceded by filtering out the harmonic component from the signal. Then, the slowly varying component reprojected onto the axes of the inertial trihedral with the use of matrix A provides information about the absolute acceleration. Thus, the above-considered device can play the role of both a three-dimensional attitude sensor and a three-dimensional sensor of absolute acceleration at the same time. To realize the discrete filtering, in the course of calculating matrix A, one can determine $\mathbf{u}$ and $\mathbf{v}$ as

$$\mathbf{u} = \frac{1}{2}[\mathbf{y}(2\pi(n-1)) - \mathbf{y}(\pi + 2\pi(n-1))].$$

The information about the acceleration may be

obtained by calculating

$$\frac{1}{2}\left[\mathbf{y}(2\pi(n-1)) + \mathbf{y}(\pi + 2\pi(n-1))\right].$$

Remark 2. Unlike the vibratory gyroscopes of the type in [5, 6], the above considered device is not balanced: the vibrating oscillator loads the mount with the reactions of the elastic constraints. This problem seems to be solvable with the use of purely constructive methods by means of adjusting two antiphased oscillators of the above type.

ACKNOWLEDGMENTS

REFERENCES

1. A. Yu. Ishlinskiĭ, *Orientation, Gyroscopes and Inertial Navigation* (Nauka, Moscow, 1976) [in Russian].

2. D. M. Klimov, *Inertial Navigation on the Sea* (Nauka, Moscow, 1984) [in Russian].

3. V. F. Zhuravlev, Izv. Ross. Akad. Nauk, Mekh. Tverd. Tela, No. 3, 6 (1993).

4. V. F. Zhuravlev, Izv. Ross. Akad. Nauk, Mekh. Tverd. Tela, No. 6, 27 (1997).

5. P. Leger, in *Proceedings of 3rd St.-Petersburg Conference on Integrated Navigation Systems, St.-Petersburg, Russia, 1996* (Russian Research Center Élektropribor, St. Petersburg, 1996), Vol. 1, p. 143.

6. Cl. Charcosset and Ch. Bonjour, Demande de Brevet Eur., Bulletin No. 20, EP 0773429 (1997).

Translated by A. Pankrat'ev

====== **MECHANICS** ======

Pressure of a Paraboloidal Die on a Thin Elastic Layer

I. I. Argatov

Presented by Academician N.F. Morozov February 24, 2005

Received March 16, 2005

The nonclassical contact problem for an elastic layer is analyzed under the assumption that the thickness of the layer is small as compared to the a priori unknown contact area. The asymptotic behavior is found for the internal stressed state. Explicit expressions are derived for the boundary layer and variation of the elliptic contact domain. The asymptotic behavior is found for the contact pressure and its resultant.

FORMULATION OF THE PROBLEM

Let us constructively consider the nonlinear problem concerning the pressure of an elliptic-paraboloidal die on an elastic layer with thickness H:

$$x_3 = -\Phi(x_1, x_2),$$
$$\Phi(x_1, x_2) = (2R_1)^{-1} x_1^2 + (2R_2)^{-1} x_2^2. \tag{1}$$

The displacement vector $\mathbf{u}$ is determined as the solution of the Lamé system that satisfies the condition of the absence of friction and the Signorini boundary condition (see, e.g., [1, 2]):

$$u_3(\varepsilon; \mathbf{x}', 0) \geq \delta_0 - \Phi(\mathbf{x}'), \quad \sigma_{33}(\mathbf{u}; \mathbf{x}', 0) \leq 0,$$
$$[u_3(\varepsilon; \mathbf{x}', 0) - \delta_0 + \Phi(\mathbf{x}')]\sigma_{33}(\mathbf{u}; \mathbf{x}', 0) = 0, \tag{2}$$
$$\mathbf{x}' = (x_1, x_2) \in \mathbb{R}^2,$$

respectively. Here, δ_0 is the die displacement and $\sigma_{3j}(\mathbf{u})$ are the stress tensor components. For definiteness, we assume that the lower surface of the elastic layer ($x_3 = H$) is coupled with an undeformable support (see also [3, Sect. 1.4]). The standard regularity conditions are taken at infinity (see, e.g., [4, Sect. 1]). Assuming that the layer is relatively thin, we set

$$H = \varepsilon H^*, \quad \delta_0 = \varepsilon \delta_0^*, \quad R_1 = \varepsilon^{-1} R_1^*,$$
$$R_2 = \varepsilon^{-1} R_2^*, \tag{3}$$

―――――――――――
Admiral Makarov State Maritime Academy,
Kosaya liniya 15-A, St. Petersburg, 199026 Russia
e-mail: argatov@home.ru

where δ_0^*, R_1^*, and R_2^* are assumed to be comparable with H^*.

An important characteristic of the problem is the contact-pressure distribution

$$p_\varepsilon(\mathbf{x}') = -\sigma_{33}(\mathbf{u}; \mathbf{x}', 0), \quad \mathbf{x}' \in \omega_\varepsilon. \tag{4}$$

Here, the contact domain ω_ε, where the settling of the elastic layer surface is directly determined by the die shape [see Eq. (2)], i.e., $u_3(\varepsilon; \mathbf{x}', 0) = \delta_0 - \Phi(\mathbf{x}')$, is unknown and should be determined in the process of solving the problem.

As is known [5, 6], the distribution of the contact pressure over the domain ω_ε is nonuniform; i.e., the domain ω_ε is separated into the following: a region in which the pressure is mainly proportional to the settling of the die; and a narrow boundary strip (with a thickness on the order of the elastic layer thickness) over the contour Γ_ε of the domain ω_ε, in which the contact pressure distribution is significantly nonuniform in the direction orthogonal to the contour Γ_ε. The contact problem for a die circular in plan was studied in [6–8, 4]. The asymptotic behavior for the problem of the one-side contact of the die with the surface with positive Gaussian curvature was constructed in [9].

INTERNAL STRESSED STATE

We introduce the dimensionless coordinates

$$\boldsymbol{\xi} = (\xi_1, \xi_2), \quad \xi_j = H_*^{-1} x_j, \quad j = 1, 2, \tag{5}$$

and the "extended" dimensionless longitudinal coordinate

$$\zeta = \varepsilon^{-1} H_*^{-1} x_3. \tag{6}$$

The substitution of Eqs. (5) and (6) reduces the Lamé system for the vector $\mathbf{u} = (\mathbf{v}, w)$, where $\mathbf{v} = $

(v_1, v_2) is the transverse displacement vector to the form

$$\varepsilon^2(\nabla_\xi \cdot \nabla_\xi \mathbf{v} + (1-2v)^{-1}\nabla_\xi\nabla_\xi \cdot \mathbf{v})$$

$$+ \varepsilon(1-2v)^{-1}\nabla_\xi\frac{\partial w}{\partial\zeta} + \frac{\partial^2 \mathbf{v}}{\partial\zeta^2} = 0,$$

$$\varepsilon^2\nabla_\xi \cdot \nabla_\xi w + \varepsilon(1-2v)^{-1}\nabla_\xi \cdot \frac{\partial \mathbf{v}}{\partial\zeta}$$

$$+ \frac{2(1-v)}{1-2v}\frac{\partial^2 w}{\partial\zeta^2} = 0.$$

(7)

In this case, the boundary conditions of the absence of friction and a rigid attachment assume the form

$$\varepsilon\nabla_\xi w + \frac{\partial \mathbf{v}}{\partial\zeta}\bigg|_{\zeta=0} = 0, \quad \mathbf{v}|_{\zeta=1} = 0, \quad w|_{\zeta=1} = 0. \quad (8)$$

Under the assumption that the point $\boldsymbol\xi$ belongs to the domain ω_ε^* and in view of the second of Eqs. (3), the Signorini boundary condition given by the second of Eqs. (2) is reduced to the equality

$$w(\boldsymbol\xi, 0) = (\delta_0^* - \Phi^*(\boldsymbol\xi)),$$

$$\Phi^*(\boldsymbol\xi) = H_*^2[(2R_1^*)^{-1}\xi_1^2 + (2R_2^*)^{-1}\xi_2^2]. \quad (9)$$

Finally, formula (4) is transformed as

$$\varepsilon\nabla_\xi\mathbf{v} + \frac{1-v}{v}\frac{\partial w}{\partial\zeta}\bigg|_{\zeta=0} = -\frac{1-2v}{2v\mu}\varepsilon H_* p_\varepsilon(\boldsymbol\xi),$$

$$\boldsymbol\xi \in \omega_\varepsilon^*. \quad (10)$$

Following the algorithm described in [10, 11], the solution of system (7) determining the displacement field under the die far from the edge of the contact domain ω_ε^* is obtained in the form

$$\mathbf{v}(\boldsymbol\xi, \zeta) = \frac{\varepsilon^2}{1-2v}\nabla_\xi\varphi_0^*(\boldsymbol\xi)\left(-2v(1-\zeta) + \frac{1}{2}(1-\zeta)^2\right), \quad (11)$$

$$w(\boldsymbol\xi, \zeta) = \varepsilon\varphi_0^*(\boldsymbol\xi)(1-\zeta) + \varepsilon^2\Delta_\xi\varphi_0^*(\boldsymbol\xi)(1-\zeta)$$

$$\times\frac{v(1+2v)}{6(1-v)(1-2v)} - \varepsilon^3\Delta_\xi\varphi_0^*(\boldsymbol\xi)$$

$$\times\left\{-\frac{2v}{1-2v}\frac{(1-\zeta)^3}{6} + \frac{v}{(1-v)(1-2v)}\frac{(1-\zeta)^2}{2}\right\}. \quad (12)$$

According to Eqs. (10)–(12), the contact-pressure

density is expressed as

$$p_\varepsilon^0(\boldsymbol\xi) = \frac{2\mu(1-v)}{(1-2v)H_*}$$

$$\times\left\{\varphi_0^*(\boldsymbol\xi) - \varepsilon^2\Delta_\xi\varphi_0^*(\boldsymbol\xi)\frac{v(1-4v)}{3(1-v)(1-2v)}\right\}. \quad (13)$$

The stressed state under the die bottom is determined by the components

$$-\sigma_{33} = \frac{2\mu(1-v)}{H_*(1-2v)}\varphi_0^*(\boldsymbol\xi) + \varepsilon^2\Delta_\xi\varphi_0^*(\boldsymbol\xi)\frac{2\mu v}{H_*(1-2v)}$$

$$\times\left(\frac{1+2v}{6(1-2v)} - (1-\zeta) + \frac{1}{2}(1-\zeta)^2\right),$$

$$-\sigma_{jj} = \frac{2\mu v}{H_*(1-2v)}\varphi_0^*(\boldsymbol\xi) + \varepsilon^2\frac{2\mu}{1-2v}\frac{H_*}{R_j^*}$$

$$\times\left(-2v(1-\zeta) + \frac{1}{2}(1-\zeta)^2\right) + \varepsilon^2\Delta_\xi\varphi_0^*(\boldsymbol\xi)\frac{2\mu}{H_*}$$

$$\times\left\{\frac{v^2(1+2v)}{6(1-v)(1-2v)^2} + \frac{v^2(1-\zeta)}{(1-v)(1-2v)} - \frac{v(1-\zeta)^2}{2(1-2v)}\right\},$$

$$\sigma_{31}\mathbf{e}_1 + \sigma_{32}\mathbf{e}_2 = \varepsilon\nabla_\xi\varphi_0^*(\boldsymbol\xi)\frac{2\mu v}{(1-2v)H_*}\zeta, \quad \sigma_{12} = 0.$$

(14)

PLANE BOUNDARY LAYER

The leading term of the asymptotic expansion of the contact pressure given by Eq. (13) determines the contact domain in the first approximation. In particular, the equation $\varphi_0^*(\boldsymbol\xi) = 0$ specifies the ellipse Γ_0^* with a semimajor axis and eccentricity that are given by the respective expressions

$$a^* = \frac{1}{H^*}\sqrt{2\delta_0^* R_1}, \quad e^2 = 1 - \frac{R_2^*}{R_1^*}. \quad (15)$$

Let the equations $\xi_1 = f_1^*(s)$ and $\xi_2 = f_2^*(s)$ give a natural parameterization of the contour Γ_0^*. In this case, the inward unit normal vector to the contour Γ_0^* is determined as

$$\mathbf{n}^0(s) = -f_2^{*'}(s)\mathbf{e}_1 + f_1^{*'}(s)\mathbf{e}_2. \quad (16)$$

To describe the behavior of the solution of the problem near the edge of the contact domain, we introduce

the local coordinates s, n, and ξ_3 near the contour Γ_0^* such that

$$\xi_1 = f_1^*(s) + n n_1^0(s), \quad \xi_2 = f_2^*(s) + n n_2^0(s),$$
$$\xi_3 = H_*^{-1} x_3. \tag{17}$$

Then, in planes orthogonal to the contour Γ_ε^*, we introduce the extended coordinates

$$n = \varepsilon \nu, \quad \xi_3 = \varepsilon \zeta. \tag{18}$$

Correspondingly, we have

$$\delta_0 - \Phi(x_1, x_2) = \varepsilon^2 H_*^2 [\nu b_1^*(s) + \varepsilon \nu^2 b_2^*(s)]; \tag{19}$$

$$b_1^*(s) = -\frac{f_1^*(s) n_1^0(s)}{R_1^*} - \frac{f_2^*(s) n_2^0(s)}{R_2^*},$$
$$2 b_2^*(s) = -\frac{n_1^0(s)^2}{R_1^*} - \frac{n_2^0(s)^2}{R_2^*}. \tag{20}$$

The boundary layer near the smooth contour Γ_0^* is sought in the form

$$\mathbf{u}(\varepsilon; \mathbf{x}) \simeq \varepsilon^2 (W_1^*(s; \nu, \zeta) \mathbf{n}^0(s) + W_2^*(s; \nu, \zeta) \mathbf{e}_3), \tag{21}$$

where $\mathbf{W}^* = (W_1^*, W_2^*)$ is the solution of the Lamé system in the band $\zeta \in (0, 1)$, $\nu \in \mathbb{R}$ satisfies the boundary conditions of the absence of friction and the rigid fixation of the support, as well as the following condition of the unilateral contact given by Eq. (2) [see Eqs. (19) and (21)]:

$$W_2^*(s; \nu, 0) \geq H_*^2 b_1^*(s) \nu, \quad \tau_{22}(\mathbf{W}^*; \nu, 0) \leq 0,$$
$$[W_2^*(s; \nu, 0) - H_*^2 b_1^*(s) \nu] \tau_{22}(\mathbf{W}^*; \nu, 0) = 0, \tag{22}$$
$$\nu \in \mathbb{R}.$$

Here, $\tau_{jk}(\mathbf{W}^*)$ are the two-dimensional stress tensor components.

Let the contour Γ_ε^* in the coordinates given by Eqs. (17) be given by the equation

$$n = h_\varepsilon^*(s), \quad h_\varepsilon^*(s) = \varepsilon h^*(s). \tag{23}$$

In this case, the contact problem for an elastic strip with the Signorini condition given by Eq. (22) under the assumption that the contact occurs over the semi-infinite interval $\nu \in (h^*(s), +\infty)$ is reduced to the integral equation (see [4, Sect. 12])

$$\int_{h^*(s)}^{+\infty} q^{**}(s, \nu') N(\nu' - \nu) d\nu' = \pi^2 \vartheta H_* b_1^*(s) \nu, \tag{24}$$

$$N(t) = \pi \int_0^{+\infty} \frac{\mathcal{L}(u)}{u} \cos ut \, du; \quad \vartheta = \frac{\mu}{1 - \nu}. \tag{25}$$

For the elastic strip rigidly coupled with the undeformable basis, we have

$$\mathcal{L}(u) = \frac{2\kappa \sinh 2u - 4u}{2\kappa \cosh 2u + 1 + \kappa^2 + 4u^2}, \quad \kappa = 3 - 4\nu. \tag{26}$$

The function $q^{**}(s, \nu)$ has the meaning of the reduced contact-pressure density, i.e.,

$$q^{**}(s, \nu) = -H^{-1} \tau_{22}(\mathbf{W}^*; \nu, 0). \tag{27}$$

Thus, taking into account Eqs. (4) and (27), near the contact boundary we have

$$p_\varepsilon(x_1, x_2) \simeq \varepsilon q^*(s, \nu). \tag{28}$$

The solution of Eq. (24) is obtained using the Wiener–Hopf method and results from [12, 13]. Following [6], we approximate the function $\mathcal{L}(s)$ by the function

$$\tilde{\mathcal{L}}(u) = u \frac{\sqrt{u^2 + B^2}}{u^2 + C}. \tag{29}$$

The functions $u^{-1}\mathcal{L}(u)$ and $u^{-1}\tilde{\mathcal{L}}(u)$ satisfy the requirements formulated by Koiter [14] only under the condition

$$\frac{B}{C} = \mathcal{A}, \quad \mathcal{A} = \lim_{u \to 0} \frac{\mathcal{L}(u)}{u}. \tag{30}$$

Additionally, following Aleksandrov [6], we set

$$\frac{1}{C} - \frac{1}{2B^2} = -2m_1, \quad m_1 = \frac{1}{2\mathcal{A}} \lim_{u \to 0} \frac{d^2}{du^2} \frac{\mathcal{L}(u)}{u}. \tag{31}$$

The positive solution of Eq. (24) with Eq. (29) exists under the condition

$$h^*(s) = \sqrt{\frac{\mathcal{A}}{B} - \frac{1}{2B}} \tag{32}$$

and has the form

$$\tilde{q}^{**}(s, \nu) = \vartheta H_* b_1^*(s) \mathcal{A}^{-1}$$
$$\times \left\{ \nu \operatorname{erf}\sqrt{B(\nu - h^*)} + \sqrt{\frac{\nu - h^*}{\pi B}} \exp(-B(\nu - h^*)) \right\}, \tag{33}$$

where $\operatorname{erf}(x)$ is the error function.

RESULTANT OF THE CONTACT PRESSURE

Separating the leading term of the asymptotic expansion for $\nu \longrightarrow +\infty$, we represent the boundary layer given by Eq. (33) in the form

$$\tilde{q}^{**}(s, \nu) = \vartheta H_* b_1^*(s) \mathcal{A}^{-1} \nu + \tilde{q}_0^{**}(s, \nu - h^*). \tag{34}$$

Here, the function

$$\tilde{q}_0^{**}(s, \tau) = \vartheta H_* b_1^*(s) \mathscr{A}^{-1}$$

$$\times \left\{ (\tau + h^*) \mathrm{erfc} \sqrt{B\tau} + \sqrt{\frac{\tau}{\pi B}} \exp(-B\tau) \right\}, \quad (35)$$

where erfc(x) is the additional error function, decreases exponentially for $\tau \longrightarrow +\infty$.

Let $\chi(t)$ be a smooth cutoff function such that $\chi(t) = 1$ for $t \in [0, \frac{1}{3}]$ and $\chi(t) = 0$ for $t \in \left[\frac{2}{3}, +\infty\right)$ and $\chi(t)$ decreases monotonically from 1 to 0 for $t \in \left(\frac{1}{3}, \frac{2}{3}\right)$. In this case, combining the internal distribution of the contact pressure given by Eq. (13) and the boundary layer given by Eq. (35), we arrive at the global approximate representation

$$p_\varepsilon(H_* \xi_1, H_* \xi_2) \approx p_\varepsilon^0(\xi_1, \xi_2)$$

$$+ \varepsilon \chi\left(\frac{n - h_\varepsilon^*}{\sqrt{\varepsilon} \rho_0^*}\right) \tilde{q}_0^{**}\left(s, \frac{n - h_\varepsilon^*}{\varepsilon}\right), \quad (36)$$

where ρ_0^* is the minimum value of the curvature radius of the contour Γ_0^*.

We emphasize that the h^* value given by Eq. (32) is positive (the domain ω_0 is an upper estimate for the contact domain ω_ε^*) and, therefore, representation (36) is correct.

The calculation of the resultant of the contact-pressure density given by Eq. (36) yields

$$P = \iint\limits_{\omega_\varepsilon} p_\varepsilon(x_1, x_2) dx_1 dx_2 \approx \mathscr{I}_\varepsilon^1 + \mathscr{I}_\varepsilon^2, \quad (37)$$

where $\mathscr{I}_\varepsilon^1 = \mathscr{I}_\varepsilon^3 - \mathscr{I}_\varepsilon^4$ and

$$\mathscr{I}_\varepsilon^2 = \varepsilon H_*^2 \iint\limits_{\tilde{\omega}_\varepsilon^*} \chi\left(\frac{n - h_\varepsilon^*}{\sqrt{\varepsilon} \rho_0^*}\right) \tilde{q}_0^{**}\left(s, \frac{n - h_\varepsilon^*}{\varepsilon}\right) d\xi_1 d\xi_2,$$

$$\mathscr{I}_\varepsilon^3 = H_*^2 \iint\limits_{\omega_\varepsilon^0} p_\varepsilon^0(\xi_1, \xi_2) d\xi_1 d\xi_2,$$

$$\mathscr{I}_\varepsilon^4 = H_*^2 \iint\limits_{\omega_\varepsilon^0 \setminus \tilde{\omega}_\varepsilon^*} p_\varepsilon^0(\xi_1, \xi_2) d\xi_1 d\xi_2.$$

The integral $\mathscr{I}_\varepsilon^3$ is calculated by transforming the domain ω_0^* into a circular one and is given by the expression

$$\mathscr{I}_\varepsilon^3 = \delta_0^* \sqrt{R_1^* R_2^*} \frac{2\pi(1 - \nu)\mu}{(1 - 2\nu)H_*}$$

$$\times \left\{ \delta_0^* + \varepsilon^2 \frac{4H_*^2}{R^*} \frac{\nu(1 - 4\nu)}{3(1 - \nu)(1 - 2\nu)} \right\}. \quad (38)$$

Passing to the local coordinates given by Eqs. (17) in the integrals $\mathscr{I}_\varepsilon^2$ and $\mathscr{I}_\varepsilon^4$, where integration is performed over a narrow band, and changing the integration variable n according to Eq. (18), we obtain

$$\mathscr{I}_\varepsilon^2 = \varepsilon^2 H_*^2 \int\limits_{\Gamma_0^*} \int\limits_0^{+\infty} \tilde{q}_0^{**}(s, \tau) d\tau \, ds + O(\varepsilon^3), \quad (39)$$

$$\mathscr{I}_\varepsilon^4 = \varepsilon^2 H_*^2 B_1^* \frac{2\mu(1 - \nu)}{1 - 2\nu} \left(\int\limits_0^{h^*} H_* \nu \, d\nu \right) + O(\varepsilon^3), \quad (40)$$

$$B_1^* = \int\limits_{\Gamma_0^*} b_1^*(s) ds.$$

Calculating integrals (39) and (40), substituting the resulting expressions into Eq. (37), and taking Eq. (38) into account, we arrive at the expression

$$P \approx \delta_0^* \sqrt{R_1^* R_2^*} \pi \vartheta \mathscr{A}^{-1} H_*^{-1} (\delta_0^* - \varepsilon^2 \cdot 4 H_*^2 (R^*)^{-1} m_1)$$

$$+ \varepsilon^3 H_*^3 \vartheta \mathscr{A}^{-1} B_1^* \left(\frac{h^*}{2B} + \frac{7}{8B^2} - \frac{(h^*)^2}{2} \right), \quad (41)$$

where the constant B_1^* is given by the second of Eqs. (40). In the case of Eqs. (1) and (19), we have

$$B_1^* = -2\pi \delta_0^* H_*^{-2} (R_1^* + R_2^*)(R_1^* R_2^*)^{-1/2}.$$

REFERENCES

1. G. Duvaut and J. L. Lions, *Les inequations en mecanique et en physique* (Dunod, Paris, 1972); *Inequalities in Mechanics and Physics* (Springer, Berlin, 1976).

2. A. S. Kravchuk, *Variational and Quasivariational Inequalities in Mechanics* (Mosk. Gos. Akad. Priborostroeniya Informatiki, Moscow, 1997) [in Russian].

3. S. M. Aleĭnikov, *Boundary Element Method in Contact Problems for Spatially Inhomogeneous Elastic Bases* (Assotsiatsiya Stroit. Vuzov, Moscow, 2000) [in Russian].

4. I. I. Vorovich, V. M. Aleksandrov, and V. A. Babeshko, *Mixed Dynamic Problems of the Theory of Elasticity* (Nauka, Moscow, 1974) [in Russian].

5. V. M. Aleksandrov, Prikl. Mat. Mekh. **28** (1964).

6. V. M. Aleksandrov, Prikl. Mat. Mekh. **33** (1969).

7. V. M. Aleksandrov, V. A. Babeshko, and V. A. Kucherov, Prikl. Mat. Mekh. **30** (1966).

8. V. A. Babeshko and V. A. Garagulya, Izv. Akad. Nauk SSSR, Mekh. Tverd. Tela, No. 1, 76 (1971).

9. V. A. Babeshko, Dokl. Akad. Nauk SSSR **206** (5), 1074 (1973) [Sov. Phys. Dokl. **17**, 973 (1973)].

10. A. L. Gol'denveĭzer, Prikl. Mat. Mekh. **21** (1962).

11. M. G. Dzhavadov, Differ. Uravn. **4** (10), 1901 (1968).

12. V. M. Aleksandrov and V. A. Babeshko, Izv. Akad. Nauk SSSR, Mekh., No. 2, 95 (1965).

13. J. B. Alblas and M. Kuipers, Acta Mech. **9**, 292 (1970).

14. W. T. Koiter, in *Applications of the Theory of Functions to Continuum Mechanics* (Nauka, Moscow, 1965), pp. 15–31 [in Russian].

Translated by R. Tyapaev

=========== **MECHANICS** ===========

Class of Dynamic Systems with Constraints

Corresponding Member of the RAS V. G. Veretennikov and V. A. Sinitsyn

Systems with constraints were first studied in [1], in which a constrained system of a kind more general than mechanical systems was considered, the principle of the elimination of constraints being applied to this system.

The class of dynamic systems with constraints is studied when they contain restrictions (constraints) realized by "reaction constraints" (reactions in what follows). The problem is to develop mathematical models for a wide variety of physical phenomena presented as constraint conditions. In the general approaches to describing a constrained motion, it is natural to use the principle of the elimination of constraints (in a wide sense) and different means for the natural and artificial realization of constraints.

The existence of a common problem made it possible to focus attention on new aspects of the interrelation between the mathematical and physical parts of the theory. In particular, for different solutions of the same differential equations (in the case when they have several solutions), it has been assumed that systems differing by constraints should be assigned different constrained systems (we call a new type of constraint, found in the process of solving the equations of motion, "hidden constraints"). It becomes possible to extend the range of application of the virtual work principle and the D'Alembert–Lagrange principle while also observing Newton's principle of determinacy.

The new type of systems with constraints is the systems with hidden constraints, which are found when the differential equations of motion have several solutions. Let us consider a simple example of such a system. One of the solutions of the equations of motions describes the equilibrium state. For this reason, we will discuss simultaneously the application of the virtual work principle [2] for the systems with ideal bilateral constraints:

$$\delta' A = \sum_k \mathbf{F}_k \cdot \delta \mathbf{r}_k = 0, \qquad (1)$$

_____

Moscow Aviation Institute
(State University of Aerospace Technologies),
Volokolamskoe sh. 4, Moscow, 125080 Russia

where $\delta' A$ is the "virtual work" of the active forces $\mathbf{F}_k$ along any virtual displacement $\delta \mathbf{r}_k$ of the kth material point.

Let the motion of a system with one degree of freedom in the case when a generalized point force is active be described by the differential equation (force is divided by mass and the dot signifies the derivative with respect to time t)

$$\ddot{x} = \alpha x^\beta, \quad \alpha = \text{const} > 0, \quad \beta = \frac{1}{3}. \qquad (2)$$

Let the virtual work of the force be equal to zero $F \delta x = 0$; then, at $\delta x \neq 0$ and from the expression for force in (2), it follows that $x = 0$ is the equilibrium position and $x = 0$ and $\dot{x} = 0$ is the equilibrium state. According to the Galilean inertia principle, the equilibrium state will be preserved, because there is no cause that would force a material point to leave the state of rest.

Along with the solution $x \equiv 0$, Eq. (2) has the other solutions

$$x = \pm at^b, \quad a = \left(\frac{\alpha}{6}\right)^{3/2}, \quad b = 3, \qquad (3)$$

which satisfy the initial conditions $x(0) = 0$, $\dot{x}(0) = 0$, and $\ddot{x}(0) = 0$. However, at $t > 0$, it is possible for the system to be in a state other than that of equilibrium. At $t > 0$, for the motions given by Eqs. (3), the force is not equal to zero and, if virtual displacements occur, i.e., $\delta x \neq 0$, then Eq. (1) is not satisfied (the necessary condition of equilibrium is not valid).

Although the initial conditions of motion obeying Eq. (3) correspond to the initial conditions of the equilibrium state at $t = 0$, the system is not in the equilibrium state later. A point force cannot cause motion from this state (see above). Therefore, considering the time $t = 0$, we arrive at the known restriction conclusions:

(i) general equation (1) is not the sufficient condition of the equilibrium of the system [3];

(ii) solution (2) is not a subject of mechanics, because Newton's principle of determinacy is not fulfilled.

What is the way out of such a situation?

Let us consider the second solution as a model of motion of another mechanical system described by the same differential equation (2) (and similarly on the third solution in (3) with the minus sign). This new system can be obtained from free system (2) by imposing the ideal nonstationary bilateral holonomic constraint

$$x - at^b = 0, \quad \delta x = 0. \tag{4}$$

The constrained system [with constraint (4)] is described by the equations

$$\ddot{x} = \alpha x^\beta + \lambda \quad (x - at^b = 0), \tag{5}$$

where λ is the constraint factor (reaction related to unit mass). To find the reaction, we substitute $\ddot{x}$ expressed from constrained-motion equation (5) into the twice differentiated constraint equation ($\ddot{x} - 6at = 0$). As a result, we obtain

$$\lambda = -\alpha x^\beta + 6at. \tag{6}$$

The substitution of reaction (6) into Eq. (5) indicates that the equation of motion (2) is identical to the twice differentiated constraint equation. In addition, the equation of the free system is identical to the equation of the constrained system, because reaction (6) equals zero (expressing the second term in Eq. (6) in terms of the coordinate, we obtain $\ddot{x} = \alpha x^\beta - \alpha x^\beta + \alpha x^\beta$ instead of Eq. (5); then, if the first or last term on the right-hand side is taken, the equation of free or bounded motion is, respectively, obtained).

Thus, one equation (2) describes three different systems: one free system and two constrained systems. The free system has the equilibrium state; the constrained systems do not. Newton's principle of determinacy is valid for each of these systems. The absence of the reaction in the equation of the constrained system masks the presence of the constraint. The procedure of expressing time in terms of coordinate is performed here only for illustration, although the reaction in (6) actually consists of two components (static and dynamic). It is also worth noting that, in the free and constrained systems of this example, the conditions for the application of Eqs. (1) are different: the free system has one degree of freedom, while the constrained systems have no degrees of freedom (from the general equation of statics, it is impossible to draw a conclusion for them concerning equilibrium, because $\delta x = 0$ in Eq. (4)).

Thus, in the case of several solutions, there are hidden (not explicitly given) constraints the inclusion of which makes it possible to assign a certain mechanical system to each solution. The answer to the question on the time instant of passage from the model of the free system to the model of a constrained system (one of them can be in the equilibrium state; the other cannot) is obtained from the dynamic system $\ddot{x} = \alpha\beta x^{-2\beta}\dot{x}$, from which (under the initial conditions $x = 0$ and $\dot{x} = 0$) under the conditions of the indeterminacy of the right-hand side, three models—$\ddot{x} = 0$ and $\ddot{x} = \pm 6a$—are chosen.

Remark. It is of interest that the passage from one model to another corresponds to natural phenomena such as "the calm before the storm" (before an earthquake), the formation of a giant wave under calm conditions, etc. The applications of Eq. (1) are as follows. It provides the necessary equilibrium conditions (both the forces and the system of material points); in other words, the principle of virtual velocities represents the general properties of the equilibrium of material points (Galileo). Descartes and Wallis took the principle to be a real cause of equilibrium [2], but this would mean that the general equation is also a sufficient condition. Strictly speaking, the determination of causes is not an aim of mathematics, but in the case of hidden constraints (and not only this case), it is mathematics that helps find the incompleteness of the initial (at first glance, faultless) model of motion. Equation (1) made it possible to reveal the absence of a cause of motion in the equilibrium position of the free system. In "new" constrained systems, the equilibrium positions are absent.

Analysis of the simplest purely mechanical system leads to a dynamic system presented in the form

$$\dot{\mathbf{x}} = \mathbf{f}(\mathbf{x}, t), \quad \mathbf{x} \in R^n, \tag{7}$$

where $\mathbf{x}$ is the phase-coordinate vector with dimension n (the phase space with Euclidean metrics and the coordinates of the vector $\mathbf{f}$ are the differentiable functions of their arguments).

Motion described by Eqs. (7) can be changed by the bilateral (explicit) constraint

$$\varphi(\mathbf{x}, t) = 0, \tag{8}$$

where φ is the continuous differentiable regular function (for simplicity, we assume that it is single). We assume that constraint (8) is realized as reactions—additive actions of the same physical nature as those described by the functions on the right-hand sides of the corresponding equations of system (7).

According to the principle of the elimination of constraints (in a wide sense), we write the equations of bounded motion

$$\dot{\mathbf{x}} = \mathbf{f}(\mathbf{x}, t) + \mathbf{r}_*, \tag{9}$$

which are considered along with constraint equation (8). On the right-hand sides of Eqs. (9), the reactions ($\mathbf{r}_*$) are objective actions changing the components of the phase velocity of the marked (according to the properties of the system) phase coordinates (we denote this vector as $\mathbf{x}_* = (x_1, \dots, x_l, 0, \dots, 0)^T, l \le n$; the coordinates of the vector $\mathbf{r}_*$ from $l + 1$ to n are taken to be equal to zero).

If certain phase coordinates are the time derivatives of other phase coordinates, the reaction is introduced only into the equation with the highest order derivative.

In the purely mechanical part of the system, reactions are forces. In the Chetaev systems, in addition to the reactions affecting the change in accelerations (derivatives of the velocities), reactions are also introduced into the first-order equations [1]. The formulation of problems concerning the bounded motion of systems with constraints of higher orders, Hamiltonian systems with constraints, etc., is similar.

Model (8) and (9) must be complemented: information concerning the problem of the realization of constraints is needed. The problem on the ways of the realization of constraints represents one of the basic problems in the dynamics of constrained systems [4]. The way of realizing the constraints can be disregarded due to the property of the ideality of constraints. Similar to analytical mechanics, this property can be formulated by using the notion of virtual displacements (see, e.g., [5]) for which we have the varied constraint equation

$$(\varphi_{\mathbf{x}_*})^T \delta\mathbf{x}_* = 0,$$

$$\varphi_{\mathbf{x}_*} = \left(\frac{\partial\varphi}{\partial x_1}, ..., \frac{\partial\varphi}{\partial x_l}, 0, ..., 0\right)^T, \qquad (10)$$

where $\delta\mathbf{x}_*$ is the vector of virtual variations (infinitesimal virtual changes in the coordinates of the vector $\mathbf{x}_*$ that satisfy constraint condition (8): the first l virtual variations fulfill Eq. (10) and the remaining variations are arbitrary). When writing the equations for virtual variations, we fix both the time and those phase coordinates in equations for which the reactions are absent.

We axiomatically introduce the criterion of the ideality of a constraint:

$$\mathbf{r}_*^T \delta\mathbf{x}_* = 0. \qquad (11)$$

A hypothesis of the physical realization of reactions formed by constraints, $\mathbf{r}_* = \lambda\varphi_{\mathbf{x}_*}$, corresponds to the property of ideality given by Eqs. (10) and (11). The undetermined multiplier λ can be found by using the same procedure as in the above example.

Taking into account the property of ideality, we obtain the general equation of bounded dynamic systems with constraints:

$$[\ddot{\mathbf{x}} - \mathbf{f}(\mathbf{x}, t)]^T \delta\mathbf{x}_* = 0. \qquad (12)$$

General equation (12) is considered together with constraint equations (8) and the equations (10) for the virtual variations. It does not contain the reactions of ideal constraints and provides equations whose number is equal to the number of independent virtual variations.

In the investigation of a dynamic system with constraints, in the case of finding hidden constraints, an additional stage appears that is associated with the consideration of these constraints in new models of motion.

REFERENCES

1. N. G. Chetaev, in *Stability of Motion. Works on Analytical Mechanics* (Akad. Nauk SSSR, Moscow, 1962), pp. 329–334 [in Russian].

2. J. L. Lagrange, *Mécanique Analytique*, 4th ed. (Gauthier-Villars, Paris, 1888; Gostekhizdat, Moscow, 1950).

3. Ya. L. Geronimus, *Theoretical Mechanics* (Nauka, Moscow, 1973) [in Russian].

4. V. V. Kozlov, Prikl. Mat. Mekh. **56**, 692 (1991).

5. V. G. Veretennikov and V. A. Sinitsyn, *Method of Varying Action* (Fizmatlit, Moscow, 2003) [in Russian].

Translated by Yu. Vishnyakov

MECHANICS

Application of the Theory of the Leray–Schauder Degree for the Approximation of Oscillations of a Satellite on an Elliptic Orbit

I. I. Kosenko

Presented by Academician V.V. Rumyantsev March 23, 2005

Received March 30, 2005

The rotational motion of an asymmetric satellite in the elliptic-orbit plane about an axis that passes through its center of mass and is perpendicular to this plane is considered. It is easy to verify [1] that the equation of oscillations of the satellite on the orbit has the form

$$
\ddot{\theta} = -3\frac{GM}{R(t)^3}\frac{A-C}{B}\sin(\theta-\nu(t))\cos(\theta-\nu(t))
$$
$$
+ c\sin(\theta-\varphi)|\sin(\theta-\varphi)|. \tag{1}
$$

Here, G is the gravitational constant; M is the mass of the attracting center; a known time function $R(t)$ is the Kepler radius of the satellite orbit; A, B, and C are the principal central moments of inertia of the satellite; θ is the rotation angle of the satellite with respect to an inertial reference frame (it is measured from the direction to the orbit periapsis); a known time function $\nu(t)$ is the true anomaly of the Kepler motion; c is the constant representing the reflecting properties of the satellite surface; and φ is the azimuth of the light-source position as measured from the direction to the periapsis.

As is known [2], for the Kepler motion, $R = \dfrac{p}{1+e\cos\nu}$, where p is the focal parameter and e is the eccentricity of the satellite orbit. The appropriate choice of the dimensional quantities ensures the conditions $GM = 1$, $p = 1$. Passing to the new independent variable ν, which is the true anomaly, we transform differential equation (1) to the form [1]

$$
x'' - \frac{2e\sin\nu}{1+e\cos\nu}x' = -\frac{\mu}{1+e\cos\nu}\sin(x-2\nu)
$$
$$
+ \frac{c}{(1+e\cos\nu)^4}f(x-2\varphi). \tag{2}
$$

Moscow State University of Service, ul. Glavnaya 99,
Cherkizovo-1, Moscow oblast, 141221 Russia
e-mail: kosenko@ccas.ru

Here, $x = 2\theta$ is the new unknown function and $\mu = \dfrac{3(A-C)}{B}$ is the dynamic asymmetry parameter of the satellite. The light pressure is taken into account by means of the function

$$
f(\alpha) = \begin{cases} 1-\cos\alpha & \text{for} \quad \sin\dfrac{\alpha}{2} \geq 0, \\[2mm] -1+\cos\alpha & \text{for} \quad \dfrac{\sin\alpha}{2} < 0, \end{cases}
$$

which has only one continuous derivative.

For $e = 1$, Eq. (2) has the singular points $\nu = \pi + 2k\pi$ ($k \in \mathbf{Z}$). Let us consider deformations of the solution of the Cauchy problem for differential equation (2) with the initial conditions specified in the middle of the solution definition interval $(-\pi, \pi)$: $x(\nu_0) = x_0$, $x'(\nu_0) = x'_0$, where $\nu_0 = 0$. These deformations are constructed as functions of the orbit eccentricity $e \in [0, 1]$. The parameters μ, c, and φ characterizing the dynamic asymmetry of the satellite, reflecting capability of its surface, and azimuth of the light source, respectively, are considered to be fixed parameters. In what follows, we replace the eccentricity e by a new parameter ε that is small near the singular value $e = 1$ and is such that

$$
e = \frac{1-\varepsilon^2}{1+\varepsilon^2}, \quad -1 \leq \varepsilon \leq 1.
$$

According to this relation, two ε values correspond to one e value. Such a change makes it possible to "regularly immerse" the limiting case $e = 1$ of the parabolic orbit into the region of the parametric analysis of the problem.

The Cauchy problem for differential equation (2) can be represented by the functional equation

$$
A(\varepsilon)z = D(z, \varepsilon), \tag{3}
$$

where $A(\varepsilon)$: $Z \longrightarrow Z$ is a linear operator and $D(\cdot, \varepsilon)$: $Z \longrightarrow Z$ is a nonlinear operator. Both operators depend

on the parameter ε and are given by the formulas

$$[A(\varepsilon)z](\nu) = z(\nu) - \frac{2e(\varepsilon)\sin\nu}{1 + e(\varepsilon)\cos\nu} y[z, x_0'](\nu),$$

$$[D(z, \varepsilon)](\nu) = -\mu \frac{\sin(x[z, x_0, x_0'](\nu) - 2\nu)}{1 + e(\varepsilon)\cos\nu}$$
$$+ c\frac{f(x[z, x_0, x_0'](\nu) - 2\varphi)}{(1 + e(\varphi)\cos\nu)^4}.$$

Here, the unknown function $z(\nu)$ is the second derivative of the configuration variable $x(\nu)$ and, according to [1], should be taken in the weight space $Z = L_{2, \omega_2}[-\pi, \pi]$, where $\omega_2(\varepsilon) = (1 + \cos\nu)^8$. In this case, the first derivative $x'(\nu) = y[z, x_0'](\nu)$ and configuration variable $x(\nu) = x[z, x_0, x_0'](\nu)$ automatically fall into the weight spaces $Y = L_{2, \omega_1}[-\pi, \pi]$, $\omega_1(\nu) = (1 + \cos\nu)^7$ and $X = L_{2, \omega_0}[-\pi, \pi]$, $\omega_0(\nu) = (1 + \cos\nu)^6$, respectively. In [1], it was proved that the operators $A(\varepsilon)z$ and $D(z, \varepsilon)$ are uniformly bounded with respect to ε. The latter operator is also uniformly bounded in $z \in Z$.

The affine operator $A(\varepsilon): Z \longrightarrow Z$ appears to be continuous and to have a continuous inverse operator uniformly in the parameter $\varepsilon \in [-1, 1]$. In what follows, we also discuss the dependence of the constructed operators on this parameter. Let us analyze the properties of the constructed mappings $A, A^{-1}, D: Z \times [-1, 1] \longrightarrow Z$ as functions of two variables z and ε.

Statement 1. *The operators A, A^{-1}, D: $Z \times [-1, 1] \longrightarrow Z$ are continuous.*

Proof. The proof is reduced to the application of the Lebesgue theorem on the passage to limit in the integrand.

The property of the compactness of the operator $D(\cdot, \varepsilon): Z \longrightarrow Z$ is important for the development of algorithms for approximating solutions of Eq. (3). Moreover, this property is valid uniformly throughout the entire interval of the parameter $\varepsilon \in [-1, 1]$.

Considering a sequence bounded in Z, using the regularity of the weight-norm integrals together with the Arzelà theorem, and applying the Lebesgue theorem, we arrive at the following statement.

Statement 2. *The operator D: $Z \times [-1, 1] \longrightarrow Z$ is compact.*

The operator $D: Z \times [-1, 1] \longrightarrow Z$ that is continuous and compact is usually called completely continuous [4] or simply compact [5].

In view of the further application of the Schauder fixed point theorem [7] and the theory of the Leray–Schauder degree [8], we first transform Eq. (3) to the equivalent form

$$z = H(z, \varepsilon), \tag{4}$$

where $H(z, \varepsilon) = A^{-1}(\varepsilon)D(z, \varepsilon)$ should be taken. Following the above analysis, we conclude that H: $Z \times [-1, 1] \longrightarrow Z$ is a completely continuous operator.

Theorem 1. *For any $\varepsilon \in [-1, 1]$ and any given parameters μ and c and initial data x_0 and x_0', Eq. (4) has a single solution $z(\varepsilon)$ in Z. Moreover, for sufficiently large $R > 0$, the strict bound*

$$\|z(\varepsilon)\|_Z < R \tag{5}$$

is valid uniformly in the parameter $\varepsilon \in [-1, 1]$.

Proof. The proof is based on the Schauder principle [7] and takes into account that the mapping H: $Z \times [-1, 1] \longrightarrow Z$ is uniformly bounded. Thus, for the given initial data, the family of solutions $x(\nu, \varepsilon)$ of the Cauchy problem for Eq. (2) that depends on the parameter $\varepsilon \in [-1, 1]$ specifies the bounded mapping $z = x''$: $[-1, 1] \longrightarrow Z$, $z: \varepsilon \mapsto z(\varepsilon)$, where $[x(\varepsilon)](\nu)$ is the solution of Eq. (2).

Following [1], one can verify the next statement.

Statement 3. *The function z: $[-1, 1] \longrightarrow Z$ is continuous.*

The above results allow the construction of the expansions of the function $z(\nu, \varepsilon)$ in the bases of the space Z with Fourier coefficients continuously depending on the parameter ε. In order to simplify the further consideration, we take certain basis $\{\chi_k(\nu)\}_{k=0}^\infty$ in the space Z and use it to construct an infinite sequence of finite-dimensional spaces $Z_1 \subset Z_2 \subset \ldots \subset Z_m \subset \ldots$ in Z such that $Z_m = \mathrm{Span}(\chi_1, \chi_2, \ldots, \chi_m)$ and $\bigcup_{m=1}^\infty Z_m$ is dense in Z. Let P_m be a projector P_m: $Z \longrightarrow Z_m$ such that $P_m^2 = P_m$ and $P_m Z = Z_m$.

To approximate the solutions of initial equation (4), we consider the finite-dimensional Galerkin equation

$$z = P_m H(z, \varepsilon). \tag{6}$$

If this equation has a solution $z_m(\varepsilon)$, then $z_m(\varepsilon) \in Z_m$. We now analyze the existence and convergence of approximate solutions to the exact solution for $m \longrightarrow \infty$.

Theorem 2. *For given initial conditions $x_0, x_0' \in \mathbf{R}$, there is a natural number M independent of ε such that Galerkin equation (6) for $m > M$ has a solution $z_m(\varepsilon) \in Z_m$. The sequence of solutions $\{z_m(\varepsilon)\}$ converges for $m \longrightarrow \infty$ to the solution of exact equation (4) uniformly in ε.*

Proof. The proof leads to the following conclusions according to [5]. On the one hand, since the mapping H: $Z \times [-1, 1] \longrightarrow Z$ is continuous and compact, the completely continuous vector field G: $(z, \varepsilon) \mapsto z - H(z, \varepsilon)$ is homotopic to the identical field G: $(z, \varepsilon) \mapsto z$. On the other hand, according to the Banach–Steinhaus theorem, the compact operator H allows a uniform finite-dimensional approximation. Therefore, the Leray–Schauder degree of the finite-dimensional oper-

ator G: $(z, \varepsilon) \mapsto z - P_m H(z, \varepsilon)$ is nonzero, which ensures the existence of a solution of Galerkin equation (6) according to the Leray–Schauder theorem [8]. The convergence of approximate solutions to the exact solution can be proved using an appropriate modification of the known Krasnosel'skii theorem [4].

The above consideration illustrates a situation that arises when approximating solutions of differential equations with singular disturbances. In the problem under consideration for the satellite, solutions on the rotation period for $e \longrightarrow 1$ can be constructed numerically by using a regularizing independent variable. However, for $e \longrightarrow 1$, the computational complexity of this problem increases unlimitedly; i.e., unlimitedly large time is required for numerical integration. Such an approach leads to algorithms that singularly depend on the parameter.

In this work, we have presented an approach ensuring the regularization of the numerical algorithm for $\varepsilon \longrightarrow 0$ ($e \longrightarrow 1$). Indeed, the solutions of the finite-dimensional equation approximate the exact solution equally well throughout the entire interval of the parameter $\varepsilon \in [-1, 1]$. The approximation algorithm itself is "insensitive" to the passage through the singular parameter value $\varepsilon = 0$. Such a regularization of the numerical procedure is obtained due to the refusal of the uniform metric in the phase space and the use of weight integral metrics. Thus, the topology of the Sobolev weight space that is coarser than the uniform topology can be treated as a measure of the computational complexity of the problem of approximating the solutions of the equation of satellite oscillations.

REFERENCES

1. I. I. Kosenko, in *Research Problems of Stability and Stabilization of Motion* (Vychislitel'nyĭ Tsentr Ross. Akad. Nauk, Moscow, 2001), Part 2, pp. 84–104 [in Russian].

2. G. N. Duboshin, *Celestial Mechanics. Basic Problems and Methods*, 2nd ed. (Nauka, Moscow, 1968) [in Russian].

3. M. A. Krasnosel'skiĭ, *Topological Methods in the Theory of Nonlinear Integral Equations* (GITTL, Moscow, 1956; Pergamon, Oxford, 1964).

4. L. Nirenberg, *Functional Analysis* (Courant Institute, New York Univ., New York, 1975; Mir, Moscow, 1977).

5. J. Schauder, Math. Z. **26** (5), 47 (1927).

6. J. Leray and J. Schauder, Ann. Ec. Norm. Suppl. **13**, 45 (1934).

Translated by R. Tyapaev

<div align="center">══════════════ MECHANICS ══════════════</div>

Integro-Differential Approach to Solving Problems of Linear Elasticity Theory

G. V. Kostin and V. V. Saurin

Presented by Academician D.M. Klimov February 7, 2005

Received February 15, 2005

In order to construct efficient algorithms for solving problems of linear elasticity theory, the approach is used based on the introduction of integral relations between components of the stress and strain tensors. In the framework of the model proposed, the integro-differential boundary value problem is reduced to a variational problem to which well-developed methods of numerical analysis are applicable [1, 2]. To demonstrate the potentialities of the proposed approach, we employ the numerical-analytical method of finding approximations for desired stress functions and displacement functions.

1. We consider an elastic body that occupies a certain region Ω with boundaries γ. We assume that the displacement and stresses are given at the parts γ_u and γ_σ of the boundary, respectively, ($\gamma_u \cap \gamma_\sigma = 0$, $\gamma_u \cup \gamma_\sigma = \gamma$). The stress–strain state of the body is described by the set of differential equations of the linear elasticity theory:

$$\sigma_{ij,\,j} = 0, \tag{1}$$

$$\sigma_{ij} = C_{ijkl}\varepsilon_{kl}^0, \tag{2}$$

$$\varepsilon_{kl}^0 = \frac{1}{2}(u_{k,\,l} + u_{l,\,k}). \tag{3}$$

The boundary conditions are written in the form

$$\sigma_{ij}n_j = \bar{\sigma}_j, \quad x \in \gamma_\sigma, \tag{4}$$

$$u_k = \bar{u}_k, \quad x \in \gamma_u, \tag{5}$$

where σ_{ij}, ε_{ij}^0, u_k, and n_j are the components, respectively, of the stress and strain tensors σ and ε^0, of the displacement vector $\mathbf{u}$, and of the unit vector $\mathbf{n}$ directed along the normal to the boundary in a certain Cartesian coordinate system $\{x_1, x_2, x_3\}$; $\bar{\sigma}_j$ and $\bar{u}_k$ are the components of the given vector functions of $\bar{\boldsymbol{\sigma}}$ and $\bar{\mathbf{u}}$ dependent on the coordinates x_i. The constants C_{ikjl} are the components of the tensor of the elastic moduli $\mathbf{C}$ ($C_{ijkl} = C_{ijlk} = C_{klij}$). In the present study, we assume the bulk forces to be absent.

The set of equations of the elasticity theory and boundary conditions (1)–(5) are the Euler equations and boundary conditions of the variational problem (principle of the potential-energy minimum [1]):

$$\Pi = \int_\Omega A(\mathbf{u})d\Omega - \int_{\gamma_\sigma}(\bar{\sigma}, \mathbf{u})d\gamma_\sigma \to \min_\mathbf{u}, \tag{6}$$

where A is the density of the strain energy, which is determined as the convolution of two of the second-rank tensors σ and ε^0:

$$A(\mathbf{u}) = \frac{1}{2}\boldsymbol{\sigma} \cdot \boldsymbol{\varepsilon}^0. \tag{7}$$

It is well known that relationships (1)–(3) describe the stress–strain state at an arbitrary inner point of a body. In this case, we consider that stresses in the inner body's points must continuously pass to stresses at the boundary, i.e., relationships (4) must hold. In the same manner, displacements of the inner body's points continuously pass to the boundary conditions described by equality (5). We should note that the continuity of the passage to the body's boundary γ of components of the elasticity-modulus tensor $\mathbf{C}$ defined at the inner body's points is implicitly assumed [1]. On the other hand, it is necessary to take into account that boundary conditions (4) and (5) cannot be given without allowance for the physical arguments generating these conditions. For example, a certain part of the boundary can be the interface between two or more media. In this case, the tensor of elastic moduli at the given boundary segment, generally speaking, is not defined.

In order to take into account the indeterminacy of the tensor $\mathbf{C}$ at the body's boundary, we propose the following integral formulation of Hooke's law:

$$\int_\Omega (\boldsymbol{\sigma} - \mathbf{C}\boldsymbol{\varepsilon}^0) \cdot (\boldsymbol{\sigma} - \mathbf{C}\boldsymbol{\varepsilon}^0)d\Omega = 0. \tag{8}$$

Institute for Problems in Mechanics,
Russian Academy of Sciences,
pr. Vernadskogo 101, Moscow, 119526 Russia
e-mail: kostin@ipmnet.ru; saurin@ipmnet.ru

From this equality, it follows that the components of the tensors $\boldsymbol{\sigma}$ and $\mathbf{C}\boldsymbol{\varepsilon}^0$ are identical to each other everywhere in the region Ω, with the possible exception of the points that constitute a zero-measure manifold. Similar approaches have been analyzed by a number of authors (see, e.g., [3]).

Using the definition of Hooke's law in the form of relationship (8), we arrive at the integro-differential problem (1), (8), (3)–(5). Below, for the sake of convenience, we introduce two new tensors $\boldsymbol{\sigma}^0$ and $\boldsymbol{\varepsilon}$ related to tensors $\boldsymbol{\varepsilon}^0$ and $\boldsymbol{\sigma}$ by the linear relations $\boldsymbol{\sigma}^0 = \mathbf{C}\boldsymbol{\varepsilon}^0$ and $\boldsymbol{\sigma} = \mathbf{C}\boldsymbol{\varepsilon}$. Using the tensors $\boldsymbol{\varepsilon}^0$, $\boldsymbol{\sigma}^0$, $\boldsymbol{\varepsilon}$, and $\boldsymbol{\sigma}$, we can rewrite integral relationship (8) in the form

$$\Phi_1 = \int_\Omega (\boldsymbol{\sigma} - \boldsymbol{\sigma}^0) \cdot (\boldsymbol{\sigma} - \boldsymbol{\sigma}^0) d\Omega = 0. \tag{9}$$

It can be shown that if relationship (9) holds, then the equalities

$$\Phi_2 = \int_\Omega (\boldsymbol{\varepsilon} - \boldsymbol{\varepsilon}^0) \cdot (\boldsymbol{\varepsilon} - \boldsymbol{\varepsilon}^0) d\Omega = 0, \tag{10}$$

$$\Phi_3 = \int_\Omega (\boldsymbol{\sigma} - \boldsymbol{\sigma}^0) \cdot (\boldsymbol{\varepsilon} - \boldsymbol{\varepsilon}^0) d\Omega = 0 \tag{11}$$

are also valid.

The proposed integral formulation of Hooke's law (8) makes it possible to reduce the integro-differential problem (1), (8), (3)–(5) of the linear elasticity theory to the variational problem. Indeed, if the solution $\boldsymbol{\sigma}^*$ and $\mathbf{u}^*$ to this set of equations does exist, then the functionals Φ_i reach their minima for this solution, namely,

$$\Phi_i(\boldsymbol{\sigma}^*, \mathbf{u}^*) = \min_{\boldsymbol{\sigma}, \mathbf{u}} \Phi_i(\boldsymbol{\sigma}, \mathbf{u}) = 0, \quad i = 1, 2, 3. \tag{12}$$

Hence, integro-differential problem (1), (8), (3)–(5) can be reduced to problems of the minimization of the functionals Φ_i with constraints (1), (3)–(5).

2. We now consider one of the possible algorithms of the approximate solution to the problems of the conditional minimization of the functionals Φ_i ($i = 1, 2, 3$) for the two-dimensional problem of the linear elasticity theory. This algorithm is based on the polynomial approximation of unknown functions for the components $\sigma_{ij}(x, y)$ and $u_i(x, y)$ of the stress tensor and displacement vector, respectively ($i, j = 1, 2, 3$) [4, 5]. We restrict our analysis to the case in which the given region Ω is a convex body with the piece-wise linear boundary γ. At each side of the polygon Ω, we set in the polynomial form the boundary conditions either for displacements or for stresses. We assume that the bulk forces are absent and approximate the unknown functions of the components of the stress tensor $\boldsymbol{\sigma}$ and of the

displacement vector $\mathbf{u}$ by polynomial functions of the form

$$\tilde{\sigma}_{ij} = \sum_{k=0}^{n_\sigma} \sum_{l=0}^{k} \sigma_{ij}^{kl} x^l x^{k-l}, \quad i, j = 1, 2, \tag{13}$$

$$\tilde{u}_i = \sum_{k=0}^{n_u} \sum_{l=0}^{k} u_i^{kl} x^l x^{k-l}, \quad i, j = 1, 2. \tag{14}$$

Here, σ_{ij}^{kl} and u_i^{kl} are certain unknown coefficients, whereas n_σ and n_u are the given degrees of the corresponding approximating complete polynomials $\tilde{\sigma}_{ij}$, $\tilde{u}_i$.

For the convex polygon Ω, this representation of the stress functions and displacement functions makes it possible to satisfy precisely the polynomial boundary conditions (4) and (5) and equilibrium equations (1) under an appropriate choice of the polynomial dimensions n_σ and n_u.

In order to satisfy equilibrium equations (1), which in the two-dimensional case are of the form

$$\frac{\partial \tilde{\sigma}_{11}}{\partial x} + \frac{\partial \tilde{\sigma}_{12}}{\partial y} = 0, \quad \frac{\partial \tilde{\sigma}_{12}}{\partial x} + \frac{\partial \tilde{\sigma}_{22}}{\partial y} = 0, \tag{15}$$

the following relationships for the coefficients σ_{ij}^{kl} must be true:

$$l\sigma_{11}^{kl} + (k - l + 1)\sigma_{12}^{k, l-1} = 0,$$
$$l\sigma_{12}^{kl} + (k - l + 1)\sigma_{22}^{k, l-1} = 0, \tag{16}$$
$$1 \leq k \leq n_\sigma, \quad 1 \leq l \leq k.$$

Upon the fulfillment of equalities (3) and (16), boundary conditions (4) and (5), and the integration over the region Ω for the corresponding functionals Φ_i, problems (12) are reduced to the minimization of the corresponding quadratic forms

$$\tilde{\Phi}_i = \mathbf{w}^T \mathbf{K}^{(i)} \mathbf{w} + 2\mathbf{b}^{(i)} \mathbf{w} \to \min_{\mathbf{w} \in \mathbb{R}^N}. \tag{17}$$

Here, $\mathbf{w}$ is the N-dimensional vector of independent parameters, which is obtained from the remaining unknown coefficients σ_{ij}^{kl} and u_i^{kl} in (13) and (14); $\mathbf{K}^{(i)} \in \mathbb{R}^{N \times N}$ is the symmetric positive matrix; and $\mathbf{b}^{(i)} \in \mathbb{R}^N$ is the vector defined by the boundary conditions.

The vectors $\mathbf{w}^{(i)}$ that provide the minimum for the corresponding functionals $\tilde{\Phi}_i$ in (17) are defined as the solutions to the following linear sets of equations (hereinafter, the problems 1, 2, 3):

$$\mathbf{K}^{(i)} \mathbf{w} + \mathbf{b}^{(i)} = 0, \quad i = 1, 2, 3. \tag{18}$$

3. We now consider as an example the problem of the transverse bending of a rectangular fixed plate (can-
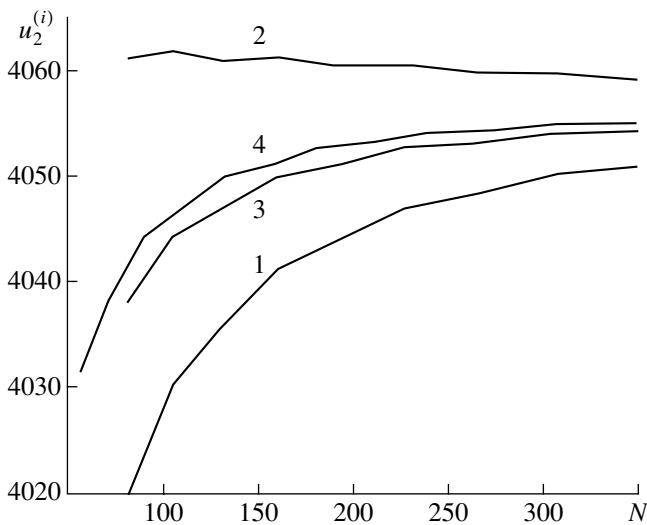
Fig. 1. Displacements $u_2^{(i)}$ vs. the number N of the degrees of freedom.
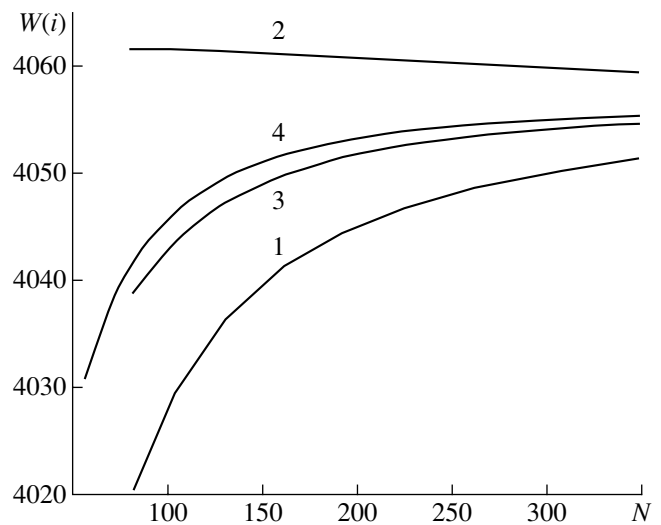
Fig. 2. Elastic energy $W^{(i)}$ vs. the number N of the degrees of freedom.

tilever bending). We assume that an isotropic plate of length l and height b is loaded by the distributed force $p(y)$ applied to the side with the coordinate $x = l$ and fixed at the side $x = 0$. The other sides of the plate are free of loads.

The following dimensionless parameters were chosen in the numerical simulation: $l = 10$, $b = 1$, the Young modulus $E = 1$, and the Poisson's ratio $\nu = 0.3$.

The boundary conditions are given in the form

$$\sigma_{22}|_{y=0} = \sigma_{22}|_{y=1} = \sigma_{12}|_{y=0} = \sigma_{12}|_{y=1} = \sigma_{11}|_{x=10} = 0,$$

$$\sigma_{12}|_{x=10} = 6(y - y^2), \tag{19}$$

$$u_1|_{x=0} = u_2|_{x=0} = 0.$$

The unknown functions σ_{ij} and u_i are approximated by the polynomials defined in formulas (13) and (14). In this case, we assume that $n_u = n_\sigma + 1$. After the boundary conditions (19) and equilibrium equations have been satisfied, in order to seek the approximate values of $\tilde{\sigma}$ and $\tilde{u}$ by means of the MARPLE program package, the problems are solved in the analytical form for the minimization of the functionals $\tilde{\Phi}_i$ ($i = 1, 2, 3$) defined in (17) for different degrees n_σ of the polynomials.

The results obtained are compared with those of the classical variational problem (6), (7) of the elasticity theory (problem 4), in which the displacement functions are approximated by complete polynomials of the degree n_W.

Figure 1 shows the displacements $u_2^{(i)}$, $i = 1, 2, 3, 4$ at the point with the coordinates $\mathbf{r} = (x, y) = (10, 0)$ (the bending at the plate edge) as a function of the number of the degrees of freedom for problems 1, 2, 3, 4. It is

worth noting that for all N, problem 2 yields an upper bound for the bending value $u_2(10, 0)$. In this case, the function $u_2^{(2)}(N)$ begins to monotonically decrease at $N > N_0 = 227$. As a lower bound, we can take, e.g., the function $u_2^{(3)}(N)$.

In Fig. 2, the values of the accumulated elastic energy W_i are presented as a function of the number of the degrees of freedom, where

$$W = \frac{1}{2} \int_\Omega \sigma \varepsilon^0 d\Omega. \tag{20}$$

In the same manner as for the bending $u_2(10, 0)$, problem 2 yields a monotonically decreasing upper
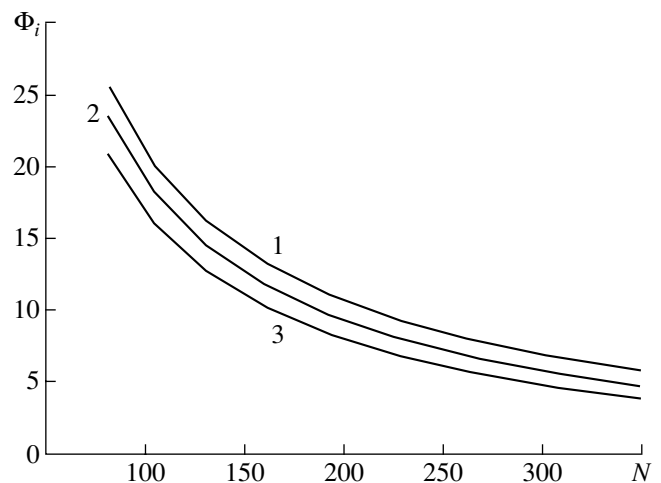
Fig. 3. Functional Φ_i vs. the number N of the degrees of freedom.

bound, whereas problems 1 and 3 yield, respectively, a monotonically increasing lower bound for the value of the accumulated elastic energy W.

The important characteristic for the convergence of the approximate solutions to problems 1, 2, 3 is that of the rate at which the corresponding magnitudes of the functionals Φ_1, Φ_2, Φ_3 tend to zero as functions depending on N. The behavior of these functions is shown in Fig. 3.

ACKNOWLEDGMENTS

REFERENCES

1. K. Washidzu, *Variational Methods in the Theory of Elasticity and Plasticity* (Pergamon, Oxford, 1982; Mir, Moscow, 1987).

2. Ph. G. Ciarlet, *The Finite-Element Method for Elliptic Problems* (North-Holland, Amsterdam, 1978; Mir, Moscow, 1980).

3. K. C. Kwon, S. H. Park, B. N. Jiang, *et al.*, Comput. Mech. **30**, 196 (2003).

4. G. V. Kostin and V. V. Saurin, Z. Angew. Math. Mech. **81**, 871 (2001).

5. G. V. Kostin and V. V. Saurin, Z. Angew. Math. Mech. **81**, 873 (2001).

Translated by G. Merzon

=========== **MECHANICS** ===========

Stability of a Thin Liquid Film Flowing on a Vertical Wall in the Presence of Mass Transfer through the Free Surface

V. A. Buchin and G. A. Shaposhnikova

Presented by Academician S.S. Grigoryan March 14, 2005

Received March 17, 2005

We have studied the problem of the description of a thin liquid film flowing on a vertical wall in the presence of mass transfer through the free surface and have constructed a class of self-similar solutions in the case of a distributed nonstationary mass flux. The stability of the obtained self-similar flows with respect to small nonstationary harmonic perturbations of the liquid parameters has been studied and it is shown that the presence of a negative mass flux through the surface (evaporation) produces a destabilizing action on the flow. Similar to the case of a stationary flowing film of constant thickness, the self-similar flows are unstable with respect to perturbations of any frequency. In the case of evaporation, the development of instability has the character of an "explosion": in the linear approximation, the amplitudes of perturbations exhibit infinite growth within a finite time (the time of evaporation of the liquid film). On the contrary, the presence of a positive mass flux through the surface (condensation, gas absorption, etc.) leads to the stabilization of the flow, whereby the amplitudes of perturbations exhibit limited growth in time over the entire film length and remain on the level of initial values. Moreover, in this case, there is a certain interval of frequencies in which small perturbations exhibit decay. It will be shown below that, using a feedback control, it is possible to stabilize the initially unstable self-similar film flows.

FORMULATION OF THE PROBLEM AND THE SYSTEM OF EQUATIONS

The flow of a thin film of incompressible liquid on the vertical wall is described by the following system of equations:

$$\frac{\partial h}{\partial t} + \frac{\partial q}{\partial x} = \chi(x, t), \tag{1}$$

$$\frac{\partial q}{\partial t} + 1.2\frac{\partial}{\partial x}\frac{q^2}{h} = gh - \frac{3\nu q}{h^2} + \frac{3q}{2h}\chi(x, t), \tag{2}$$

Institute of Mechanics, Moscow State University, Moscow, 117192 Russia

where t is the time, x is the coordinate in the gravity force direction, h is the film thickness, q is the flow rate, $\chi(x, t)$ is the mass flux through the film surface (in the general case, dependent on both coordinate and time), ν is the kinematic viscosity, and g is the acceleration of gravity.

The system of equations (1), (2) is obtained by averaging the equation of continuity and the equation of motion of the incompressible liquid, with allowance for the boundary conditions on the free surface and at the vertical solid wall [1–3]. The presence of mass transfer through the free surface influences the velocity of motion and, hence, changes the kinematic condition on the surface. In this study, we consider the case of a small mass flux through the surface. For this reason, the dependence of the longitudinal component of the liquid velocity on the transverse coordinate is assumed to be quadratic (as in the absence of mass transfer) [1–3]. In addition, consideration will be restricted to the evolution of long-wavelength perturbations, so that the term describing the surface tension in Eq. (2) can be omitted.

Let us introduce the dimensionless variables and parameters defined as

$$t^* = \frac{t}{t_c}, \quad x^* = \frac{x}{L}, \quad q^* = \frac{q}{q_c}, \quad h^* = \frac{h}{h_c},$$

$$q_c = \frac{gh_c^3}{3\nu}, \quad t_c = \frac{h_c L}{q_c}, \tag{3}$$

$$\beta = \frac{9\nu^2 L}{gh_c^4}, \quad \chi^* = \chi\frac{t_c}{h_c},$$

where h_c, q_c, t_c, and L are the characteristic film thickness, flow rate, time, and film length, respectively. In what follows, we set $\beta = 1$ (by selecting an appropriate L value) and omit the asterisk at the dimensionless quantities.

In terms of the dimensionless variables, Eqs. (1) and (2) appear as

$$\frac{\partial h}{\partial t} + \frac{\partial q}{\partial x} = \chi(x, t), \tag{4}$$

$$\frac{\partial q}{\partial t} + 1.2\frac{\partial}{\partial x}\frac{q^2}{h} = h - \frac{q}{h^2} + \frac{3q}{2h}\chi(x, t). \tag{5}$$

As is known, the stationary solution for a vertical film exhibits convective instability. The amplitude of small harmonic perturbations introduced at a certain point of the flow exhibits exponential growth downstream the flow (while remaining finite at each fixed coordinate x) [1–3].

In the presence of mass transfer through the free surface, the unperturbed film flow is substantially nonstationary. There are no analytical methods for investigation of the stability of arbitrary nonstationary flows. However, the available methods for the investigation of the stability of stationary flows can be generalized to apply to the analysis of self-similar flows representing a partial case of nonstationary flows.

SELF-SIMILAR SOLUTIONS

Let us consider the conditions under which the system of equations (4), (5) admits self-similar solutions

$$h = (1 + \kappa t)^{1/2}H_s(\xi), \quad q = (1 + \kappa t)^{3/2}Q_s(\xi),$$
$$\xi = \frac{x}{(1 + \kappa t)^2}, \quad \kappa = \text{const.} \tag{6}$$

Such solutions exist, in particular, if the mass flux through the surface obeys the relation

$$\chi = \chi_0(1 + \kappa t)^{-1/2}\chi_1(\xi).$$

Let us restrict our consideration to the simplest variant, where the expression for the mass flux is

$$\chi(t) = \chi_0(1 + \kappa t)^{-1/2}, \quad \chi_0 = \text{const.} \tag{7}$$

The case of $\chi_0 < 0$, $\kappa < 0$ corresponds to a negative mass flux (evaporation), while $\chi_0 > 0$ and $\kappa > 0$ correspond to a positive mass flux (condensation). The κ value determines the characteristic time of the process. The physical meaning of this quantity is especially clear in the case of evaporation ($\kappa < 0$): the value of abs(κ) is inversely proportional to the dimensionless time (relative to a certain initial moment) required for the complete evaporation of the liquid film.

Substituting expressions (6) and (7) into Eqs. (4) and (5), we obtain the following system of equations

for the functions $H_s(\xi)$ and $Q_s(\xi)$:

$$Q'_{s\xi} - 2\kappa\xi H'_{s\xi} + \frac{1}{2}\kappa H_s = \chi_0, \tag{8}$$

$$1.2\left(\frac{Q_s^2}{H_s}\right)'_{\xi} - 2\kappa\xi Q'_{s\xi} + \frac{3}{2}\kappa Q_s = H_s - \frac{Q_s}{H_s^2} + \frac{3}{2}\chi_0\frac{Q_s}{H_s}. \tag{9}$$

For investigation of the stability of solutions determined by the functions $H_s(\xi)$ and $Q_s(\xi)$, it is convenient to introduce new variables, defined as

$$\tau = \frac{1}{\kappa}\ln(1 + \kappa t), \quad \xi = \frac{x}{(1 + \kappa t)^2}, \tag{10}$$

$$h = (1 + \kappa t)^{1/2}H(\tau, \xi), \quad q = (1 + \kappa t)^{3/2}Q(\tau, \xi). \tag{11}$$

Using these variables, Eqs. (4) and (5) can be rewritten as

$$H'_\tau - 2\kappa\xi H'_\xi + \frac{1}{2}\kappa H + Q'_\xi = \chi_0, \tag{12}$$

$$Q'_\tau - 2\kappa\xi Q'_\xi + \frac{3}{2}\kappa Q + 1.2\left(\frac{Q^2}{H}\right)'_\xi = H - \frac{Q}{H^2} + \frac{3}{2}\chi_0\frac{Q}{H}. \tag{13}$$

The simplest solution of the system of equations (8), (9) is

$$H(\xi) = H_{s0} = 1, \quad Q_s(\xi) = Q_{s0} = \left(1 + \frac{3}{4}\kappa\right)^{-1}, \tag{14}$$
$$\kappa = 2\chi_0.$$

Here, the last equality introduces an additional relation between χ_0 and κ, which will simplify the subsequent analysis. In a more thorough investigation, this relation should be excluded. Now let us proceed to an analysis of the stability of solution (14).

CONVECTIVE INSTABILITY OF SMALL PERTURBATIONS

A solution to the system of equations (12), (13) can be represented in the following form:

$$H = H_{s0} + H_1(\tau, \xi), \quad Q = Q_{s0} + Q_1(\tau, \xi), \tag{15}$$
$$H_1 \ll H_{s0}, \quad Q_1 \ll Q_{s0}.$$

A system of linearized equations for H_1 and Q_1 follows from Eqs. (12) and (13) and appears as

$$H'_{1\tau} - 2\kappa\xi H'_{1\xi} + \frac{1}{2}\kappa H_1 + Q'_{1\xi} = 0, \tag{16}$$

$$Q'_{1\tau} + (-2\kappa\xi + 2.4Q_{s0})Q'_{1\xi} - 1.2Q_{s0}^2 H'_{1\xi}$$
$$= \left(1 + 2Q_{s0} - \frac{3}{4}\kappa Q_{s0}\right)H_1 - \left(1 + \frac{3}{4}\kappa\right)Q_1. \tag{17}$$

It can be shown that both characteristics of the hyperbolic system (1), (2) (and, hence, of the system (16), (17)) are directed downstream. All perturbations introduced into the flow will also be carried downstream with the flow.

Now let us study the following problem. Assume that harmonic perturbations with respect to τ are continuously introduced into the flowing film at $x = 0$ ($\xi = 0$):

$$H_1(\tau, 0) = H_{10}\exp\{i\omega\tau\},$$
$$Q_1(\tau, 0) = Q_{10}\exp\{i\omega\tau\}, \tag{18}$$

where H_{10} and Q_{10} are (in the general case) complex quantities. A solution to the system of equations (16), (17) with the boundary conditions (18) can be found in the following form:

$$H_1 = Y(\xi)\exp\{i\omega\tau\}, \quad Q_1 = Z(\xi)\exp\{i\omega\tau\}, \tag{19}$$

where the functions Y and Z are determined from the system of equations

$$i\omega Y - 2\kappa\xi Y' + \frac{1}{2}\kappa Y + Z' = 0, \tag{20}$$

$$i\omega Z + (-2\kappa\xi + 2.4Q_{s0})Z' - 1.2Q_{s0}^2 Y'$$
$$= \left(1 + 2Q_{s0} - \frac{3}{4}\kappa Q_{s0}\right)Y - \left(1 + \frac{3}{4}\kappa\right)Z. \tag{21}$$

Upon the exclusion of Z, this system reduces to the second-order equation for Y:

$$-\left(i\omega + 1 + \frac{3}{4}\kappa\right)\left(i\omega + \frac{1}{2}\kappa Y - 2\kappa\xi Y'\right) - \left(\left(i\omega + \frac{1}{2}\kappa\right)Y'\right.$$
$$\left. - 2\kappa\xi Y''\right)(-2\kappa\xi + 2.4Q_{s0}) - 1.2Q_{s0}^2 Y'' \tag{22}$$
$$= \left(1 + 2Q_{s0} - \frac{3}{4}\kappa Q_{s0}\right)Y'.$$

Now let us consider two limiting cases.

Case 1: $\kappa\xi \ll Q_{s0}$. In this case, Eq. (22) simplifies to

$$1.2Q_{s0}^2 Y'' + \left(2.4Q_{s0}\left(i\omega - \frac{3}{2}\kappa\right) + 1 + \left(2 - \frac{3}{4}\kappa\right)Q_{s0}\right)Y'$$
$$+ \left(i\omega - \frac{5}{4}\kappa\right)\left(i\omega + \frac{1}{2}\kappa\right) = 0. \tag{23}$$

A solution to this equation is

$$Y = c_1 e^{\mu_1\xi} + c_2 e^{\mu_2\xi}; \tag{24}$$

where μ_1 and μ_2 are the roots of the quadratic equation

$$1.2Q_{s0}^2\mu^2 + \left(2.4Q_{s0}\left(i\omega - \frac{3}{2}\kappa\right) + 1 + \left(2 - \frac{3}{4}\kappa\right)Q_{s0}\right)\mu$$
$$+ \left(i\omega - \frac{5}{4}\kappa\right)\left(i\omega + \frac{1}{2}\kappa\right) = 0. \tag{25}$$

When κ is positive, $\xi = \dfrac{x}{(1 + \kappa t)^2}$ $\xi \longrightarrow 0$ with increasing t at any fixed x. Accordingly, the function Y tends to $Y(0)$ with increasing t at any fixed x irrespective of the magnitude and sign of the real parts of μ_1 and μ_2. An analysis of the dependence of μ_1 and μ_2 on the frequency ω shows that the real parts of both μ_1 and μ_2 for $\kappa \le 1$ and $0 < \omega < 100$ are on the order of unity. Therefore, when t increases, the perturbations in the case under consideration remain uniformly bounded with respect to x (rather than growing exponentially with x as is the case for $\kappa = 0$).

For negative κ, the length of the interval of x in which $\kappa\xi \ll Q_{s0}$ tends to zero with increasing t. However, the results of numerical analysis showed that, for both $\kappa\xi \ll Q_{s0}$ and the intermediate values of $\kappa\xi \sim Q_{s0}$, the perturbations grow but do not pass to a nonlinear growth stage. The further evolution of perturbations is characterized by the asymptotic behavior considered below.

Case 2: $\kappa\xi \gg Q_{s0}$. In this case, Eq. (22) simplifies to

$$4\kappa^2\xi^2 Y'' - 2\kappa\xi\left(2i\omega - \frac{11}{4}\kappa + 1\right)Y'$$
$$+ \left(i\omega - \frac{5}{4}\kappa + 1\right)\left(i\omega + \frac{1}{2}\kappa\right)Y = 0. \tag{26}$$

This is the well-known Euler equation, the general solution to which is

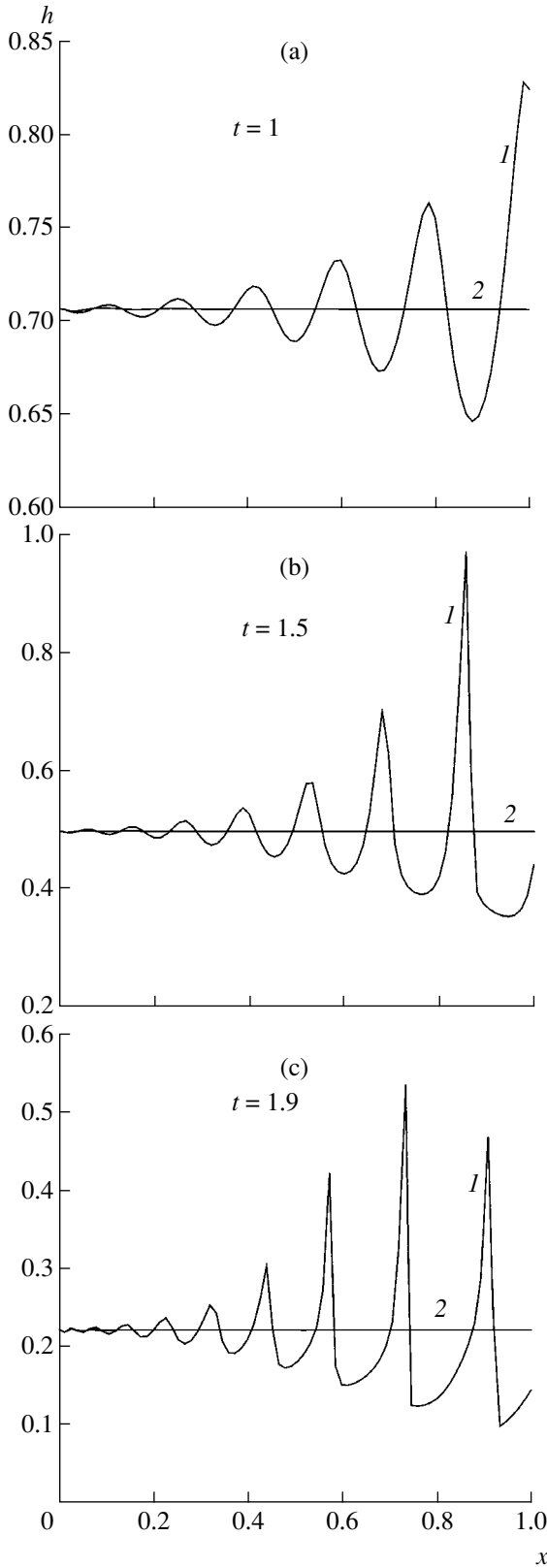$$Y = c_1\xi^{\mu_1} + c_2\xi^{\mu_2}, \quad c_1, c_2 = \text{const}, \tag{27}$$

where μ_1 and μ_2 are constants satisfying the quadratic equation

$$4\kappa^2\mu^2 - 2\kappa\left(2i\omega - \frac{3}{4}\kappa + 1\right)\mu$$
$$+ \left(i\omega - \frac{5}{4}\kappa + 1\right)\left(i\omega + \frac{1}{2}\kappa\right) = 0. \tag{28}$$

Upon solving this equation, we readily obtain

$$\mu_1 = \frac{1}{2} + \frac{i\omega}{2\kappa}, \quad \mu_2 = -\frac{5}{8} + \frac{1}{2\kappa} + \frac{i\omega}{2\kappa}. \tag{29}$$

Substituting these formulas into expression (27) and

Fig. 1. Plots of the liquid film thickness h versus coordinate x in a thin liquid film flowing on a vertical wall (*1*) without and (*2*) with a feedback control for the dimensionless time $t = 1$ (a), 1.5 (b), and 1.9 (c). The flow experienced perturbation at $t = 0$ (see the text for the system parameters).

returning to the initial variables t and x, we obtain

$$h = (1 + \kappa t)^{1/2}(1 + c_1 h_1 + c_2 h_2), \qquad (30)$$

$$h_1 = x^{1/2}(1 + \kappa t)^{-1} x^{i\omega/2\kappa}, \qquad (31)$$

$$h_2 = x^{-5/8 + 1/2\kappa}(1 + \kappa t)^{1/4 - 1/\kappa} x^{i\omega/2\kappa}. \qquad (32)$$

In the formulas for h_1 and h_2, the term

$$x^{i\omega/2\kappa} = \exp\{i\omega \ln x/(2\kappa)\} \qquad (33)$$

has a modulus equal to unity and determines the oscillatory character of perturbations depending on the spatial coordinate. The spatial period of these oscillations decreases (i.e., the frequency grows) with increasing x. It should be noted that the temporal evolution of perturbations does not exhibit an oscillatory character. The character of the spatial and temporal evolution of perturbations strongly depends on the sign of κ.

In the case of evaporation ($\kappa < 0$), formula (31) shows that the amplitude h_1 increase with both x and t. In the linear approximation, the time-dependent term tends to infinity within a finite time $\left(\text{for } t \longrightarrow \dfrac{1}{|\kappa|}\right)$.

Such a growth of perturbations with time can be considered an "explosion." The perturbation growth rate increases with $|\kappa|$ The second perturbation mode amplitude h_2 tends to zero with increasing x and vanishes when $t_1 \longrightarrow \dfrac{1}{|\kappa|}$.

When the mass is supplied to the film ($\kappa > 0$), the analysis of formulas (30)–(32) shows that the amplitude h_1 exhibits unlimited growth with increasing x, but the time-dependent term tends to zero with increasing t. This implies that, at each fixed x, the amplitude h_1 vanishes with time and the rate of this decrease grows with increasing κ. The amplitude h_2 of the second perturbation mode tends to zero with increasing x for $0 < \kappa < \dfrac{4}{5}$, exhibits unlimited growth for $\kappa > \dfrac{4}{5}$, and is independent of x for $\kappa = \dfrac{4}{5}$. With increasing t, the second perturbation mode amplitude h_2 tends to zero with increasing x for $0 < \kappa < 4$, exhibits unlimited growth for $\kappa > 4$, and is independent of t for $\kappa = 4$. Thus, when the parameter κ is in the interval $0 < \kappa < 4$, the total perturbation amplitude $c_1 h_1 + c_2 h_2$ decreases with time at any fixed x.

The stabilizing action of condensation ($\kappa > 0$) on the evolution of perturbations in the film is related to the fact that the main flow velocity linearly increases with time. The perturbations (growing with time) are also carried downstream with increasing velocity and, at each fixed x, their amplitudes, depending on the frequency ω, either vanish with time or remain limited (on

the order of initial values). In the case of evaporation ($\kappa < 0$), the main flow velocity tends to zero. As a result, the perturbations (growing with time) are carried downstream slower and slower, which leads to their infinite growth (within the linear approximation) at each fixed x. In the final stage of evaporation, the film thickness becomes comparable with the amplitude of perturbations and the linear theory is no longer valid.

SUPPRESSION OF INSTABILITY

In order to solve the task of maintaining the flat surface of evaporating liquid film unperturbed, it is possible to use a feedback control as proposed previously [2, 3] for the flows without mass transfer through the surface. The proposed stabilizing system comprises a set of controllers of the following type. The kth controller is located at $kd \leq x \leq (k+1)d$, where $k = 0, 1, \ldots$ and $d > 0$, and includes a sensor that continuously measures the deviation of the film thickness from the current unperturbed value at $x = (k + 1)d$, a feedback circuit with a constant gain α whose output determines the degree of homogeneous heating or cooling of the wall at $kd \leq x \leq (k + 1)d$, and a heating (cooling) device. The heating or cooling of the wall leads to a corresponding change in the liquid viscosity, thus producing a controlled action on the flow [3]. An example of the stabilization of the flow in evaporating liquid film with harmonic perturbations introduced at $x = 0$ is offered by the results of a numerical experiment presented in the figure. In this experiment, the parameters of the main flow, perturbation, and feedback control were as follows: $\kappa = -0.5$ (which corresponds to a dimensionless time of $t = 2$ from $t = 0$ to complete evaporation); initial perturbation amplitude, 0.001; perturbation frequency, $\omega = 50$; $d = 0.02$; and feedback gain, $\omega = 3$. Note that the scale in the x axis is strongly compressed because the results are presented in the dimensionless form. As can be seen from these data, the proposed feedback control solves the task of flow stabilization.

ACKNOWLEDGMENTS

REFERENCES

1. V. Ya. Shkadov, Nauchn. Tr. Inst. Mekh. Mosk. Gos. Univ., No. 25, 192 (1973).
2. V. A. Buchin and G. A. Shaposhnikova, J. Magn. Magn. Mater. **201**, 343 (1999).
3. V. A. Buchin and G. A. Shaposhnikova, Dokl. Akad. Nauk **381** (3), 341 (2001) [Dokl. Phys. **46** (11), 821 (2001)].
4. V. A. Buchin and G. A. Shaposhnikova, Dokl. Akad. Nauk **381** (4), 484 (2001) [Dokl. Phys. **46** (11), 873 (2001)].

Translated by P. Pozdeev

===================== **MECHANICS** =====================

Development of Shear Instability at the Explosion Products–Metal Interface under Conditions of the Sliding Detonation of the Explosive Charge

O. B. Drennov, A. I. Davydov, A. L. Mikhaĭlov, and V. A. Raevskiĭ

Presented by Academician R.I. Il'kaev February 21, 2005

Received March 16, 2005

The Kelvin–Helmholtz instability (also known as shear instability) is a type of hydrodynamic instability that develops at the interface between two contacting flows involving a tangential discontinuity of the velocity field [1]. Mathematical description of the instabilities of interfaces is inevitably approximate, and it is common practice to ignore phenomena such as molecular diffusion (for gases or miscible liquids), evaporation, condensation, and viscosity. For simplicity, a mathematical analysis of the Kelvin–Helmholtz instability was originally also performed for an ideal (nonviscous and incompressible) liquid. In the simplest case, an unstable flow can be described by the following boundary conditions [2]:

$$U(y) = \begin{cases} U & \text{for} \quad y < 0, \\ U' & \text{for} \quad y > 0, \end{cases}$$

$$\rho(y) = \begin{cases} \rho & \text{for} \quad y < 0, \\ \rho' & \text{for} \quad y > 0. \end{cases} \quad (1)$$

The Kelvin–Helmholtz instability also represents a dynamic instability of the interface $y = 0$ in the flow described by relations (1), including the cases of $\rho = \rho'$ (in homogeneous medium) and $g = 0$ (in the absence of gravity). The surface tension at the $y = 0$ interface reduces rather than eliminates this instability.

The problem of the Kelvin–Helmholtz instability in a nonviscous fluid can be mathematically treated as the problem with initial data for an autonomous conservative Lagrange's dynamical system with an infinite number of the degrees of freedom. An equilibrium flow obeying relations (1) represents the equilibrium state of such a system, the stability of which can be studied in terms of the general theory of small oscillations. This theory stipulates the possibility of representing an arbi-

trary small oscillation as a linear superposition of elementary wave solutions. The amplitude $a(t)$ of any elementary wave with the wavenumber k satisfies the ordinary differential equation

$$\frac{d^2 a}{dt^2} = S(k)a \quad (2)$$

and the condition of stability is formulated as

$$S(k) < 0 \quad (3)$$

for all k. Here, $S(k)$ is the so-called perturbation growth factor, which is a function of the wavenumber.

In the particular case of a single flat interface described by relations (1), an elementary wave solution of the differential equation (2) corresponds to sinusoidal perturbations of the interface with an arbitrary wavelength $\lambda = 2\pi/k$. For a horizontal interface in the vertical gravitational field (two fluids with different viscosities and flowing at different velocities), a small sinusoidal perturbation of the interface with a wavelength $\lambda = 2\pi/k$ must exhibit exponential growth according to the law $\exp[S(k)t]$ with the perturbation growth factor [2]

$$S(k) = \frac{\rho\rho'k^2}{(\rho+\rho')^2}(U-U')^2$$
$$- \frac{\rho-\rho'}{\rho+\rho'}(g+\ddot{y})k - \frac{\sigma k^3}{\rho+\rho'}; \quad (4)$$

where ρ and ρ' are the densities of layers, U and U' are their velocities, $\ddot{y}$ is the acceleration of the low-density layer, g is the acceleration of gravity, and σ is the surface tension at the interface. The wavenumber $k = \dfrac{2\pi}{\lambda}$ is introduced for the symmetrization of the plane wave equation with respect to x and t.

Russian Federal Nuclear Center VNIIEF,
Sarov, 607190 Russia
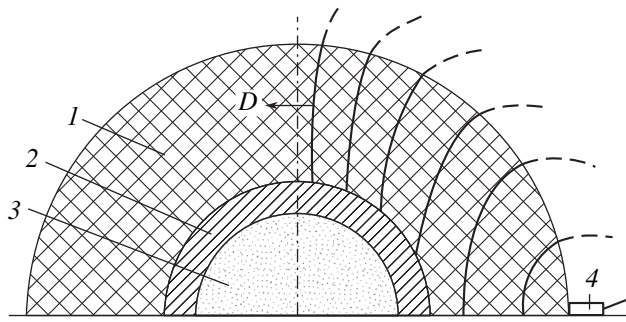
Fig. 1. Schematic diagram of the experimental arrangement (see the text for explanations).

The condition of stability (3) for the interface characterized by relation (4) can be written as [2]

$$4g(\rho - \rho')\sigma > \frac{\rho^2 {\rho'}^2 (U - U')^4}{(\rho + \rho')^2}. \tag{5}$$

The Kelvin–Helmholtz instability phenomenon in liquids and gases has been studied in much detail, including interfaces of the gas–gas, gas–liquid, and liquid–liquid types [1–5]. In recent decades, some experiments have been devoted to monitoring the development of shear instability at the contact between two metals [6–9]. However, investigations of the state of the interface between a medium possessing finite strength (e.g., metal) and a medium without strength (gas, liquid) under the conditions of flow at a large relative velocity have not been reported thus far. Although the process of the interaction of solid surfaces with explosion products (EPs) under conditions of the sliding detonation of explosives is known and has been used for a long time (explosion welding, explosion alloy-free coating, etc.), the related features in the state of the EP–metal interface upon such dynamic loading conditions has never been studied. It has been pointed out [10] that an analog of the cumulative jet is formed at the EP–metal interface upon the sliding detonation of an explosive, which is manifested by the appearance of traces of the jet action (blisters, caverns) on the surface of a metal obstacle oriented perpendicularly to the direction of motion of the detonation wave front.

This paper presents the results of experiments in which we successfully observed the development of perturbations at the EP–metal interface under conditions of the sliding detonation of an explosive. Figure 1 shows a schematic diagram of the experimental arrangement. We used a loading system of spherical geometry, comprising a spherical steel capsule *2* (Steel 10 grade) with an outer radius of $R = 87$ mm and wall thickness of $\Delta = 4$ mm, which was filled with a porous substance b_3 and placed inside a spherical layer *1* of an explosive (TNT, $\rho_0 = 1.6$ g/cm^3, $D = 6.9$ mm/µs) with an outer radius of $R = 127$ mm and a thickness of $\delta = 40$ mm. The explosive was initiated at one point *4*.

After the explosion, the surface of the steel capsule (i.e., the EP–metal interface) exhibited large periodic wavy perturbations. Figure 2 presents a photograph of a fragment of the steel surface upon explosion. Figure 3 shows a micrograph (magnification, ×30) of a transverse section of the EP–metal interface showing the perturbation profile, which is characterized by the following parameters: wavelength, $\lambda \approx 2.5$ mm; amplitude, $a \approx 0.22$ mm.

Evidently, the interface between hot EPs and the metal featured the development of the Kelvin–Helmholtz instability. High-temperature (~3500 K) EPs slide

Fig. 2. Photograph of a fragment of the steel surface upon interaction with the explosion products.
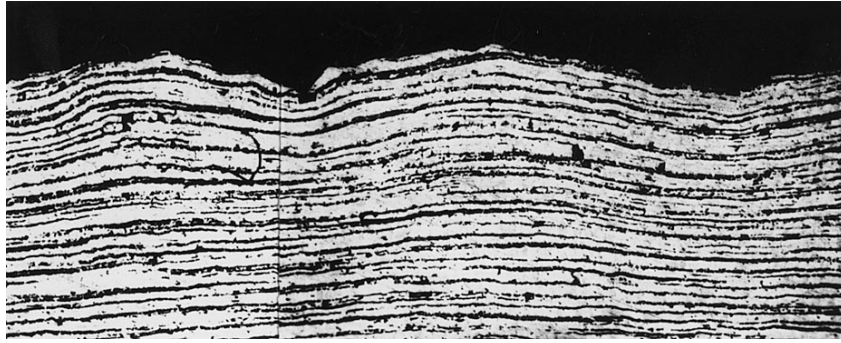
Fig. 3. Micrograph of a transverse section of the EP–metal interface showing the perturbation profile (magnification, ×30).

along the steel surface at a high velocity $\left(U = \dfrac{D}{4} \leq \right.$ 2.2 mm/µs $\left. \right)$. Under these conditions, both the tangential and normal velocity of the metal layer can be ignored. The short-term dynamic action leads to the development of intense plastic straining at the EP–metal interface, which leads to heating and a resulting loss of strength (softening) in the thin surface layer of the metal. Under the action of a large rotor of the tangential velocity U, this layer features the development of the Kelvin–Helmholtz instability.

The initial perturbation amplitude ($a_0 \approx 10^{-2}$ mm) is determined by the steel surface finish. Under dynamical loading conditions, the perturbation increases according to the exponential law until its amplitude becomes comparable with the depth of the softened metal layer. Further growth is impeded by the strength of deeper metal layers.

Previously, we considered the development of small perturbations in the case of an ideal liquid sliding over the surface of a high-strength solid [11]. This formulation of the problem corresponds to a variant whereby one substance is sliding over another solid whose surface layer is deprived of strength as a result of thermal softening. In the approximation of an elastic-plastic medium, the critical condition of stability for this layer can be expressed as

$$\frac{a_0}{\lambda} \leq \left(\frac{a_0}{\lambda}\right)_{cr} \approx \frac{\sigma_T}{G}\left[\left(\frac{M_{cr}}{M}\right)^2 - 1\right]\frac{1}{4\pi\sqrt{3}}; \qquad (6)$$

where a_0 is the initial perturbation amplitude, λ is the perturbation wavelength, σ_T is the yield strength of the layer, ρ is the density of the layer, M is the Mach number, $\mu = U/c$, c is the shear wave velocity in the elastic layer, U is the velocity of the ideal liquid layer, M_{cr} is the critical Mach number for the given perturbation wavelength, and G is the shear modulus in the layer. For perturbation wavelengths much smaller than the liquid

layer thickness, we have $M_{cr} \approx 1.8$, and the critical condition (6) acquires the following form:

$$\begin{aligned}\left(\frac{a_0}{\lambda}\right)_{cr} &\approx \frac{\sigma_T}{G}\left[\left(\frac{1.8}{M}\right)^2 - 1\right]\frac{1}{4\pi\sqrt{3}} \\ &\approx \frac{\sigma_T}{\rho}\left[\left(\frac{1.8}{U}\right)^2 - \left(\frac{1}{c}\right)^2\right]\frac{1}{4\pi\sqrt{3}}.\end{aligned} \qquad (7)$$

For many metals under conditions of shock waves that are not very strong, we have $\rho/\rho_0 < 0.05$ and

$$\frac{\sigma_T}{G}\frac{1}{4\pi\sqrt{3}} \approx 10^{-3}.$$

Then, for the EP velocity $U \approx 2.2$ mm/µs and the shear wave velocity in steel $c = 2.8$ mm/µs, we obtain

$$\left(\frac{a_0}{\lambda}\right)_{cr} \approx 10^{-3}\left[\left(\frac{1.8 \times 2.8}{2.2}\right)^2 - 1\right] \approx 4.25 \times 10^3.$$

For a typical surface roughness of $a_0 \approx 10^{-2}$ mm, the critical perturbation wavelength is $\lambda_{cr} \approx 2.4$ mm. Perturbations with longer wavelengths must not exhibit growth. In the experiments, we observed the growth of perturbations with $\lambda \approx 2.5$ mm, which is close to the calculated critical value.

Thus, the experimentally observed growth of perturbations at the EP–metal interface can be interpreted in terms of the development of the Kelvin–Helmholtz instability in the surface layer of the metal exhibiting a short-term thermal softening. Using the proposed model, the critical perturbation wavelength λ_{cr} such that perturbations with greater wavelengths do not grow is estimated.

ACKNOWLEDGMENTS

REFERENCES

1. G. Birkgoff, *Hydrodynamics. Study in Logic, Fact and Similitude* (Princeton Univ., New Jersey, 1960; Inostrannaya Literatura, Moscow, 1963).

2. *Hydrodynamics Instability, Proceedings of Symposia in Applied Mathematics*, Ed. by G. Birkgoff (American Mathematical Society, New York, 1962; Mir, Moscow, 1964), Vol. 3, p. 372.

3. A. Amsden and F. Harlow, Phys. Fluids **7** (3), 327 (1964).

4. R. Gerwin, Rev. Mod. Phys. **40** (3), 652 (1968).

5. R. Esch, J. Fluid Mech. **3**, 289 (1957).

6. A. L. Mikhaĭlov, Fiz. Goreniya Vzryva **15** (2), 158 (1979).

7. O. B. Drennov, Prikl. Mekh. Tekh. Fiz., No. 3, 41 (1989).

8. O. B. Drennov, Zh. Tekh. Fiz. **69**, 38 (1999).

9. O. B. Drennov, Khim. Fiz. **20** (8), 86 (2001).

10. É. O. Mindeli, V. G. Kabulashvili, T. G. Mardaleishvili, and É. Sh. Chagelishvili, Fiz. Goreniya Vzryva **15** (1), 150 (1979).

11. O. B. Drennov, A. L. Mikhaĭlov, P. N. Nizovtsev, and V. A. Raevskiĭ, Vopr. Atom. Nauki Tekh., Ser.: Teor. Prikl. Fiz., No. 1, 34 (2001).

Translated by P. Pozdeev

=== **MECHANICS** ===

Duration of Transient Processes in the Formation of Internal-Wave Beams

E. V. Ermanyuk and N. V. Gavrilov

Presented by Academician V.M. Titov February 21, 2005

Received March 15, 2005

At the initial stage of the harmonic oscillations of a circular cylinder in a linearly stratified fluid, a fan-shaped pattern of internal waves is formed. With time, this wave system is transformed to the classical St. Andrew's cross pattern: the internal waves emitted by the oscillating body are localized inside four beams directed at angle $\alpha = \arcsin \Omega$ to the horizon. Here, $\Omega = \dfrac{\omega}{N}$, where ω is the body oscillation frequency and $N = \left[\left(-\dfrac{g}{\rho}\right)\dfrac{d\rho}{dy}\right]^{1/2} = \text{const}$ is the buoyancy frequency for the fluid with density ρ in the presence of the gravitational acceleration g directed oppositely to the y axis. The beam width is on the order of the characteristic size of the body. The phase patterns of internal waves for steady-state oscillations and for the impulse displacement of bodies were discussed in [1]. The theoretical solution for internal waves generated by harmonic oscillations of a circular cylinder in a linearly stratified ideal fluid was obtained in [2]. An approximate solution for the case of nonzero fluid viscosity was given in [3]. Various approaches to solving the problem of the emission of internal waves by oscillating bodies in a viscous fluid were also discussed in [4]. A number of problems concerning the viscous mechanism of generating internal waves were considered in [5–7].

The nonstationary problem of the formation of internal-wave beams has been studied less thoroughly. A review of works and the asymptotic solutions of the time-dependent problem concerning internal waves generated by various systems of model singularities were given in [8]. Systematic experimental investigations of transient processes at the initial stage of the formation of internal-wave beams have not yet been carried out. In this work, quantitative experimental estimates for the duration of transient processes are obtained using the correlation analysis of wave-disturbance fields at different times.

Lavrent'ev Institute of Hydrodynamics, Siberian Division,
Russian Academy of Sciences,
pr. Akademika Lavrent'eva 15, Novosibirsk, 630090 Russia
e-mail: ermanyuk@hydro.nsc.ru

The experiments were conducted in a rectangular test tank 100 cm in length, 15 cm in width, and 30 cm in depth. The tank was filled with a linearly stratified fluid. Stratification was created using a sugar–water solution. Internal waves were generated by vertical oscillations of the circular cylinder with diameter D. To acquire quantitative information on wave perturbations in the fluid, we used the version of the "synthetic" schlieren method that was proposed in [9, 10] and used in [9, 11] to analyze the characteristics of steady patterns of internal waves generated by harmonic oscillations of various bodies. The synthetic schlieren method is based on the computer analysis of optical distortions of an image that is obtained by video recording of a contrast pattern (e.g., the system of black and white bands) through a fluid layer disturbed by the passage of internal waves. In this work, a regular system of black points on a white background is used as such a pattern. The passage of internal waves through the stratified fluid is accompanied by local disturbances of the refractive-index gradient. For this reason, the visible positions of background points observed through the disturbed fluid layer differ from those for the undisturbed layer. Various methods for quantitative estimates of the visible displacement of the background elements were discussed in [10]. In this work, the cross-correlation analysis of images, which is one of the basic methods of particle image velocimetry, is used to calculate the displacements of background points. Methods for analyzing images were reviewed in [12]. A formula relating the visible vertical displacements of background points δ_y to the disturbances of the buoyancy frequency squared was obtained in [9]. In these experiments, $\Delta N^2 = -5.23\delta_y$ (where ΔN^2 and δ_y are measured in squared inverse seconds and centimeters, respectively). It is convenient to represent the measurement results for disturbances of the density field in the dimensionless form using the relation $w' = \dfrac{\partial w}{\partial y} = -\dfrac{\Delta N^2}{N^2}$, where $w(x, y)$ is the vertical-displacement field of liquid particles in a wave with respect to the initial undisturbed position. Video recording was performed by means of a personal digital video camera with a 768×576-pixel matrix. The
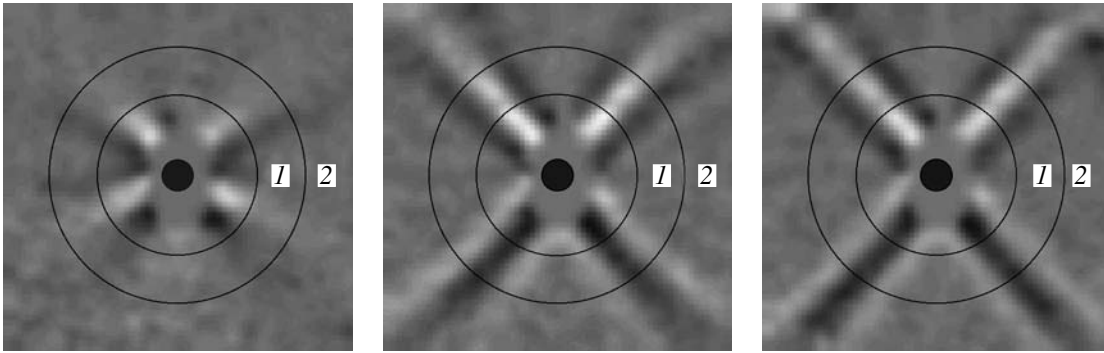
Fig. 1. Internal-wave pattern for various times at the initial stage of oscillations of a circular cylinder in a linearly stratified fluid.
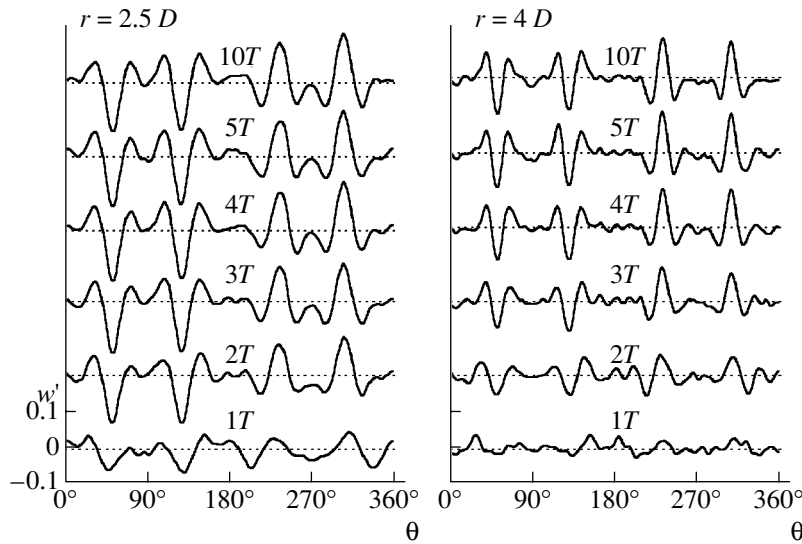

Fig. 2. Profiles $w'(\theta)$ for various times at various distances from the source of disturbances.

data for a region with size D around the oscillating cylinder are filtered in the course of processing, because large optical distortions in this region were beyond the framework of applicability of the method in use.

In the experiments, the center of the circular cylinder underwent vertical oscillations described as $y_c = 0$ for $t < 0$ and $y_c = a\sin(\omega t)$ for $t \geq 0$. Figure 1 shows the patterns of internal waves at the times $t =$ (from left to right) T, $3T$, and $5T$, where $T = \dfrac{2\pi}{\omega}$ is the oscillation period. The grey level is proportional to w' (light and dark regions correspond to $w' < 0$ and $w' > 0$, respectively). The wave patterns in Fig. 1 are obtained for $D = 2$ cm, $a = 0.6$ cm, $\Omega = 0.7$, and $N = 1.05$ s^{-1}. The black circle at the center of each figure is the initial position of the cylinder. Circles 1 and 2 are drawn at distances $r = 2.5D$ and $4D$ from the cylinder axis, respectively. It is seen in Fig. 1 that the St. Andrew's cross pattern of internal waves in the region under consideration is formed in several oscillation periods. Figure 2 shows the distribution of w' over the angular coordinate θ

along circles 1 and 2 (see Fig. 1) at various times. The angle θ is measured anticlockwise from the horizontal line. All curves in Fig. 2 correspond to the fixed phase of cylinder oscillations for which $y_c = 0$ and $\dfrac{dy_c}{dt} > 0$ and differ from each other by the ordinal numbers of oscillation periods. The vertical scale, which is identical for all $w'(\theta)$ distributions, is shown for lower curves. The dotted straight lines correspond to the undisturbed state of the fluid. With time, the characteristic width of the internal-wave beams decreases and the magnitude of w' increases and approaches steady asymptotic values. It is seen that the time interval of the formation of the asymptotic form of the profiles $w'(\theta)$ increases with r. As a quantitative characteristic of the duration of transient processes, it is convenient to use the correlation function for the distributions $w'(\theta)$ that are obtained for a fixed oscillation phase:

$$R(m, M) = \int_0^{2\pi} w'(\theta, mT)w'(\theta, MT)d\theta,$$
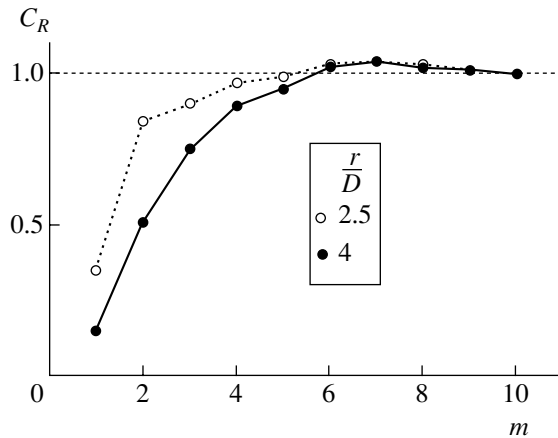
Fig. 3. Distribution $C_R(m)$ for various distances $\dfrac{r}{D}$ from the source of disturbances at a fixed oscillation frequency Ω.
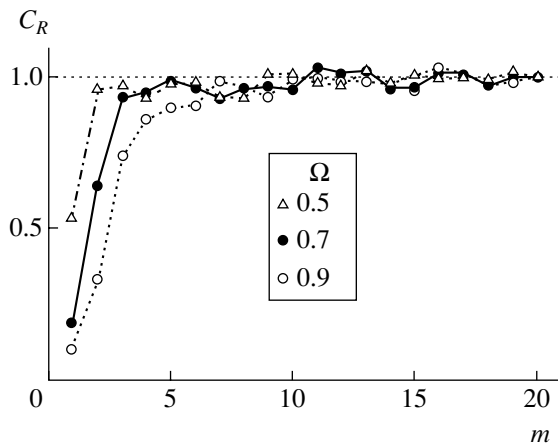
Fig. 4. Distribution $C_R(m)$ for various oscillation frequencies Ω at a fixed distance $\dfrac{r}{D}$ from the source of disturbances.

where m and M are the ordinal numbers of oscillation periods. In particular, we may set $M = m + 1$ or take a sufficiently large M value at which the wave pattern can be considered as stationary. It is convenient to introduce the dimensionless correlation coefficient as $C_R = \dfrac{R(m, M)}{R(M, M)}$. For steady oscillations, $C_R \longrightarrow 1$ for sufficiently large m and M. It is worth noting that the analysis of data in terms of C_R is universal to a certain extent for the class of problems under consideration, because it is independent of the geometry of the internal-wave generator.

Figure 3 shows $C_R(m)$ for the conditions corresponding to Figs. 1 and 2. For the parameters used in the experiments, $M = 10$ may be taken as a sufficiently large value. Since the velocity of the propagation of disturbances is finite, the characteristic relaxation time for

transient processes increases with r. The velocity of the propagation of disturbances depends on Ω. For $\Omega \longrightarrow 1$, the slope angle of the internal-wave beams is $\alpha \longrightarrow 90°$ and the group velocity of internal waves approaches zero. Figure 4 shows the characteristic form of the curves $C_R(n)$ for various Ω values. The data are obtained with the parameters $D = 1$ cm, $a = 0.6$ cm, $N = 1.4$ s^{-1}, $r = 6D$, and $M = 20$ as a sufficiently large value. It is seen that the duration of the transient process increases for $\Omega \longrightarrow 1$.

Thus, for large r values and $\Omega \longrightarrow 1$, the parameters of internal waves approach the asymptotically steady values in a noticeable time interval after the onset of oscillations. This interval can be estimated using the $C_R(m)$ dependence. We emphasize that, for r on the order of tens of D, the characteristic duration of transient processes may reach tens of T, which should be taken into account in experimental investigations of the wave characteristics at large distances from the source of disturbances. In particular, such conditions arise when studying the propagation of internal-wave beams in stratified waveguides.

REFERENCES

1. D. E. Mowbray and B. S. H. Rarity, J. Fluid Mech. **28**, 1 (1967).
2. D. G. Hurley, J. Fluid Mech. **351**, 105 (1997).
3. D. G. Hurley and G. Keady, J. Fluid Mech. **351**, 119 (1997).
4. S. A. Makarov, V. I. Neklyudov, and Yu. D. Chashechkin, Izv. Akad. Nauk SSSR, Fiz. Atmos. Okeana **26** (7), 744 (1990).
5. Yu. V. Kistovich and Yu. D. Chashechkin, Prikl. Mekh. Tekh. Fiz. **40** (6), 31 (1999).
6. Yu. V. Kistovich and Yu. D. Chashechkin, Prikl. Mekh. Tekh. Fiz. **42** (1), 52 (2001).
7. Yu. V. Kistovich and Yu. D. Chashechkin, Dokl. Akad. Nauk **382** (6), 772 (2002) [Dokl. Phys. **47**, 458 (2002)].
8. B. Voisin, J. Fluid Mech. **496**, 243 (2003).
9. B. R. Sutherland, S. B. Dalziel, G. O. Hughes, and P. F. Linden, J. Fluid Mech. **390**, 93 (1999).
10. S. B. Dalziel, G. O. Hughes, and B. R. Sutherland, Exp. Fluids **28**, 322 (2000).
11. B. R. Sutherland and P. F. Linden, Phys. Fluids **14**, 721 (2002).
12. R. J. Adrian, Annu. Rev. Fluid Mech. **23**, 261 (1991).

Translated by R. Tyapaev

===== **MECHANICS** =====

Supersonic Flow around an Elongated Blunt Body near a Screen

V. P. Stulov[a], P. V. Stulov[a], and L. I. Turchak[b]

Presented by Academician G.G. Chernyĭ June 1, 2005

Applied problems present one of the promising areas for applying the rapidly developed field of numerical experiment. In this work, the behavior of an elongated blunt body near a screen in a supersonic flow is analyzed.

The placement of various cargos and devices on the external surface of a main aircraft that separate from it during the flight is characteristic of the current stage of aircraft development. It would be difficult to overstate the importance of understanding the laws of aerodynamic interference for the flying craft's safe start and for the precise execution of tactical–technical tasks. This problem for subsonic flight velocities was studied in [1]. The case of supersonic velocities, where the interaction of shock waves with each other and with streamlined surfaces is the decisive process, has been studied much less thoroughly.

The aim of this work is to demonstrate the capabilities of numerical experiment for solving rather complex problems of aerodynamic interference. Flow fields around elongated blunt bodies near a screen, as well as the coefficients of drag and lift force, have been calculated.

We calculate the flow around a circular cylinder with radius 1 and length L. The cylinder has a hemispherical front surface and a flat back section, is located at distance h from the flat screen, and is streamed by a flow of a perfect gas with the adiabatic index $\gamma = 1.4$. Two series of calculations were performed for (i) the cylinder whose axis is parallel to the screen and $0 \le h \le 3$ and (ii) the cylinder that is streamed at the angle of attack $0° \le \alpha \le 15°$ and whose back section is spaced at a distance of $h = 1$ from the screen. All calculations were performed for the Mach number of free flow M = 3 and the length of the cylindrical part of the body $L = 8$.

For the flow at zero angle of attack around the body located at small distances from the screen ($h \approx 0.05$), the bow shock wave in the flow symmetry plane is orthogonal to the screen. In this case, the flow near the hemispherical blunting is similar to the flow around two spheres with the center line across the flow [2] for small distances between spheres. Therefore, the flow near the front part in the low near-screen region is subsonic. This ensures a relatively high drag of the body for small h values. The drag coefficient $c_x(h)$ is shown in Fig. 1. As h increases, c_x decreases rapidly, because the known pattern of the flow around a single sphere with the separated shock wave is quite rapidly recovered with increasing h. As usual, the closed subsonic zone is recovered in the shock layer.

Small oscillations in $c_x(h)$ are likely associated with the interaction between the bow shock wave reflected from the screen and wake behind the cylinder. This interaction leads to nonmonotonic changes in the bottom pressure. The flow pattern around the body for
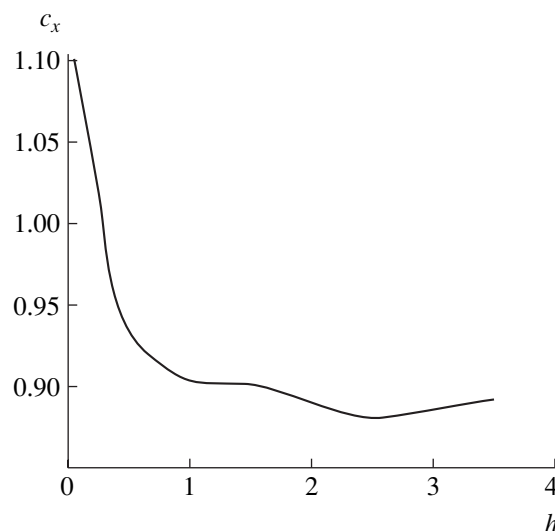
[a] *Institute of Mechanics, Moscow State University,*
  Michurinskiĭ pr. 1, Moscow, 119192 Russia
  e-mail: pstulov@imec.ru

[b] *Dorodnicyn Computing Center,*
  Russian Academy of Sciences,
  ul. Vavilova 40, Moscow, 119991 Russia

Fig. 1. Drag coefficient for $\alpha = 0$.

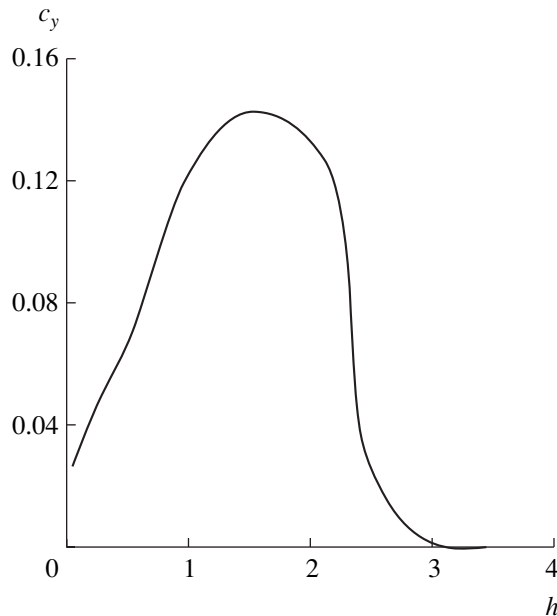**Fig. 2.** Flow pattern for $h = 1$.

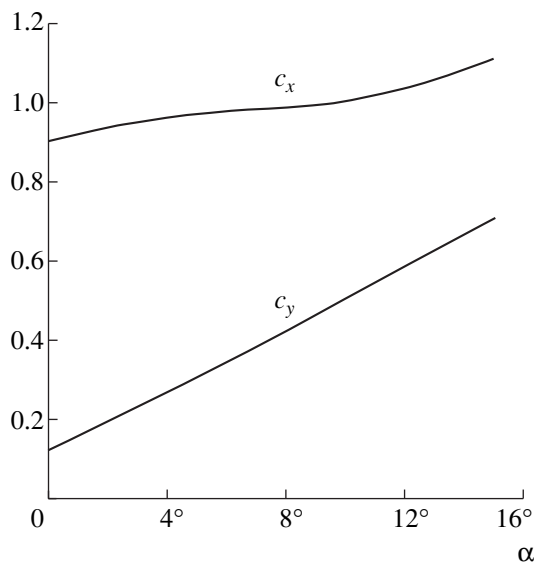**Fig. 3.** Lift-force coefficient for $\alpha = 0$.

Fig. 4. Drag coefficient and lift-force coefficient vs. the angle of attack.

$h = 1$ is shown in Fig. 2. The asymmetry of the wake is a consequence of this interaction.

Figure 3 shows the distribution of the lift-force coefficient $c_y(h)$. Under these conditions, the presence of the lift force is completely determined by interference. A relatively surprising result is a nonmonotonic change in c_y: as h increases, c_y first increases to a certain maximum value at $h \approx 1.5$ and then decreases rapidly to zero. This behavior is attributed to the laws of multiple reflection of the bow shock wave from both the screen and the lateral cylindrical surface of the body. We recall that the bow shock wave initially has the shape of a surface of revolution with variable intensity along the generatrix. It is of interest to develop an approximate analytical model of such multiple reflection of the shock wave from the flat and cylindrical surfaces.

Figure 4 shows the results of the second series of calculations, i.e., for the flow around the body at the angle of attack α. To simplify the calculations, $S = \pi$, i.e., the section of a unit-radius sphere, is taken as the midship section in the formulas for c_x and c_y [2]. As was expected, the drag and lift force increase almost linearly with α. Comparing c_y values in Figs. 3 and 4, we easily conclude that the effect of the screen on the lift force in the variant under consideration is secondary, excluding the region of small angles of attack $\alpha \approx 1°-2°$. This range of the simultaneous effect of the angle of attack and the screen on the lift force can evidently increase for smaller h values.

Thus, the above approach based on numerical experiments provides for the investigation of the aerodynamics of elongated bodies in the presence of interference. Applying known numerical-simulation techniques, one can study a phenomenon in detail, for example, the behavior of the bow shock wave for small distances from the body surface to the screen.

A number of interesting aerodynamic problems including those presented in [1], as well as other problems, can be solved applying the above approaches. This method provides broad possibilities for calculating and designing possible new systems.

REFERENCES

1. N. A. Baranov, A. S. Belotserkovskiĭ, M. I. Kanevskiĭ, and L. I. Turchak, *Numerical Methods of Aircraft Dynamics in the Presence of Aerodynamic Interference* (Nauka, Moscow, 2001) [in Russian].
2. I. A. Zhdan, V. P. Stulov, and P. V. Stulov, Dokl. Akad. Nauk **396** (2), 191 (2004) [Dokl. Phys. **49**, 315 (2004)].

Translated by R. Tyapaev